



**Swansea
University**
**Prifysgol
Abertawe**

Quantitative polarised light microscopy of metals

Hamed Safaie

Supervised by

Prof. Cameron Pleydell-Pearce

Prof. Richard Johnston

Submitted to Swansea university in fulfilment of the requirements
for the degree of


Doctor of Philosophy in Material Science and Engineering

Swansea University

November 2021

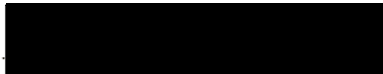
Declarations

This work has not previously been accepted in substance for any degree and is not being concurrently submitted in candidature for any degree.

Signed... 


Date... 9/12/2021

This thesis is the result of my own investigations, except where otherwise stated. Other sources are acknowledged by footnotes giving explicit references. A bibliography is appended.

Signed... 

Date... 9/12/2021

I hereby give my consent for my work, if relevant and accepted, to be available for photocopying and for inter-library loans **after expiry of a bar on access approved by the University.**

Signed... 

Date... 9/12/2021

The University's ethical procedures have been followed and, where appropriate, that ethical approval has been granted.


Signed... 

Date... 9/12/2021

If you DON'T have a bar on access, include the declarations below


Declarations

This work has not previously been accepted in substance for any degree and is not being concurrently submitted in candidature for any degree.

Signed... 


Date... 9/12/2021

This thesis is the result of my own investigations, except where otherwise stated. Other sources are acknowledged by footnotes giving explicit references. A bibliography is appended.

Signed... 


Date... 9/12/2021

I hereby give consent for my thesis, if accepted, to be available for photocopying and for inter-library loan, and for the title and summary to be made available to outside organisations.

Signed... 

Date... 9/12/2021

The University's ethical procedures have been followed and, where appropriate, that ethical approval has been granted.

Signed... 

Date... 9/12/2021

Dedication

I would Like to dedicate this thesis to my loving parents Reza and Akram whose been always supporting and loving me unconditionally. My dear sister Haniyeh never left my side and been there whenever I needed a friend. Also, this work dedicated to the memory of my beloved auntie, who passed away during the final year of my PhD.

Acknowledgments

I would not have been able to complete this PhD without the help and support of the kind people around me including colleagues, friends, and family.

I would like to thank my supervisors, Professor Cameron Pleydell-Pearce and Professor Richard Johnston for their consistent support and guidance during the running of this project to make my Ph.D. experience productive and stimulating. Besides my supervisors, I would like to thank Dr. Mark Coleman and Dr. Amit Das for their insightful comments and ideas during my PhD studies. I acknowledge the financial and equipment support from the Swansea University and Advanced Imaging of Materials Centre, United Kingdom.

I would like to thank my friends who have supported me and had to put up with my stresses and moans.

Also, I would like to thank myself for believing in my abilities, for working hard towards my goals and getting up after each failure.

Lastly, I would like to express my deepest gratitude to my family for their unfailing support, encouragement, sacrifice, and kindness. Indeed, they were my major source of strength and support.

Abstract

For most engineering metals a material's crystal structure can play a significant role in its performance in service. This is particularly relevant for materials that display pronounced differences in their physical properties depending on the arrangement and orientation of these crystals. Examples of such alloys are titanium and aluminium which are employed in a wide range of applications from medical to structural. Conventionally, the crystal structure of these materials is measured using various X-ray and electron diffraction techniques. Unfortunately, these are generally costly, time-consuming and therefore impractical in an industrial quality assurance setting. On-going research at Swansea University has demonstrated that a simpler alternative offers a solution to this problem. The project aimed to build on this research to develop a semi-automated method to conduct this analysis. The work involves extensive characterisation of various materials using optical and electron microscopes; this will focus on the direct correlation of electron diffraction data to polarised light microscopy. The project will concentrate on developing this apparatus to provide high quality, reliable information on material crystal structures. Electron Backscatter Diffraction (EBSD) is the most well-known approach to investigate the crystal orientation of polycrystalline material. However, when compared to optical microscopy EBSD is an expensive approach, very time consuming and complex laboratory technique needed to plot a crystal orientation map. The research offers a novel approach for optically anisotropic (titanium) and isotropic (aluminium) material to plot the crystal orientation map. The aim of the research is to offer a simpler, cheaper, and less time-consuming method which can be affordable by a middle-class company to have access to the crystal orientation map.

Table of contents

Chapter 1 Introduction

1.1 Crystallography	1
1.2 Unit cells	2
1.2.1. Unit cell characterisation.....	4
1.2.1.1. Face Centred Cubic (FCC).....	5
1.2.1.2. Aluminium	5
1.2.2.1. Hexagonal Close Packed (HCP)	7
1.2.2.2. Titanium.....	7
1.3. Isotropic and anisotropic material	8
1.4. Unit cell orientation effect on mechanical properties of polycrystalline material	9
1.5. Crystal Orientation Maps (COM's)	10
1.6. Microscopy.....	12
1.6.1. Light or optical microscope	13
1.6.1.1. Objective lenses	14
1.6.1.2. Eyepiece lenses	14
1.6.1.3. Condenser lenses.....	15
1.6.1.4. Light source	16
1.6.1.4.1. Halogen light.....	16
1.6.1.4.2. White LEDs.....	17
1.6.1.4.3. Monochromatic LEDs.....	18
1.6.1.5. Magnification development	18
1.6.2. Scanning Electron Microscope (SEM).....	19
1.6.2.1 Electron Column	20
1.6.2.2. Electron gun.....	21
1.6.2.2. Condenser lens	21
1.6.2.3. Objective lens.....	22
1.6.2.4. Sample stage	22

1.6.2.5. Electron beam and sample interaction	22
1.7. Electron Backscatter Diffraction (EBSD).....	25
1.7.1. How EBSD works	26
1.7.2. EBSD applications	27
1.8. Problem statement	29
1.8.1. Simplicity	29
1.8.3. Speed limitation	29
1.8.4. Source limitation	30
1.8.5. Cost	30
1.8.7. Sample condition.....	30
1.8.8. Beam damage	30

Chapter 2 Polarised light

2.1. Polarised light.....	32
2.1.1. General physics of polarised light.....	33
2.1.1.1. Stokes parameter	36
2.1.2. Polarised light classification	37
2.1.2.1. Linearly polarised light	38
2.1.2.2. Circular polarisation.....	43
2.1.2.3. Elliptical polarisation	46
2.1.3. Classification of circular and linear polarised light microscopy by intensity profile	49

Chapter 3 (PLM)

3.1. Introduction	52
3.2. Light path design.....	53
3.2.1. Linearly polarised light generation	53
3.2.2. Crossed polarised condition	55
3.3. Optically isotropic & anisotropic material	57
3.3.1. Optical isotropy	57
3.3.2. Optically anisotropic	58
3.4. Tensors	59

3.4.1. Linear elasticity	59
3.4.2. Anisotropic Elasticity	60
3.4.2.1. Hooke's Law	60
3.4.2.2. Effects of crystal symmetry on C and S matrices.....	61
3.5. HCP crystal symmetry	64
3.5.1. Symmetry of operation.....	65
3.5.1.1. Euler 1 (Φ_1) symmetry.....	65
3.5.1.2. Euler 2 (Φ) symmetry	66
3.5.1.3. Euler 3 (Φ_2) symmetry	67
3.6. Qualitative observations of the Interaction of anisotropic crystals with polarised light	68
3.7. Experimental procedure	68
3.7.1. Sample preparation.....	68
3.7.2. EBSD data acquisition and presentation	69
3.7.3. Optical microscopy	70
3.8. Qualitative comparisons.....	71
3.8.1. Quantifying microstructure	74
3.8.2. Quantitative comparison	75
3.9.1. Euler 1 correlation.....	78
3.9.2. Euler 2 correlation.....	83
3.9.3. Euler 3 correlation.....	87
3.10. Forming the crystal orientation map	88
3.11. Shortcomings of the linear cross-polarised acquisition method	90
3.11.1 Stage rotation errors	91
3.11.2 Light source errors	91
3.11.3 Cross polarised light condition errors	91
3.12. Conclusions	91

Chapter 4 (CPLM)

4.1. Introduction	93
4.2. Experimental procedure	95

4.2.1. Material Preparation.....	95
4.2.2. EBSD.....	95
4.2.3. Light path design for CPLM	96
4.2.4 Anodising process	100
4.3 Result and discussion	102
4.3.1 Qualitative analysis	102
4.3.2 Euler corellation	105
4.3.2.1 Euler 1 corellation.....	105
4.3.2.2 Euler 2 corellation.....	108
4.4 Theoretical validation of the observed incident beam rotation after reflection	111
4.5 Final Microstructure map.....	119
4.6. Anodised data.....	120
4.7. Conclusions	122
Future work	124
Appendix	125
Refrences.....	131

Table of figures

Figure 1.1 Representation of atoms positions in crystalline and amorphous material. A) crystalline material B) Amorphous material.....	2
Figure 1.2 Position of atoms in FCC unit cells.	5
Figure 1.3 Position of atoms in HCP unit cells.	7
Figure 1. 4 Crystal orientation map (COM) of isotropic material. A) COMs of completely ordered crystals B) COMs of randomly orientated crystals.	11
Figure 1.5 Crystal Orientation Map of textured polycrystalline material.	12
Figure 1.6. simplified source types of different type of microscope. A) optical microscope B) Scanning Electron Microscope.	12
Figure 1.7 Light path for reflected and transmitted light microscope. A) Transmitted light microscope B) Reflected light microscope.	13
Figure 1.8 Objective lenses diagram for optical microscope.	14
Figure 1.9. ZEISS Primotech microscope diagram.....	15
Figure 1.10 The range of frequencies of electromagnetic radiation and their respective wavelengths and photon energies.....	16
Figure 1.11 Simplified schematic of scanning electron microscope.....	20
Figure 1.12 The interaction volume of an electron beam on a sample.....	24
Figure 1.13 A) Shoji Nishikawa and Seishi Kikuchi Diffraction of Cathode Rays by Calcite. Nature 122 (1928) 726 B) Backscatter Kikuchi patterns obtained from fluorspar (fluorite). H. Boersch 1937.....	25
Figure 1.14 Simplified system for EBSD detector.....	26
Figure 2.1 Propagation of the transverse optical field and formation of the resultant vector in the form of a rotated polarisation ellipse.	34
Figure 2.2 Diagram of creating linearly vertical polarised light.	38
Figure 2.3 Creating linearly polarised light with certain optical axis.	39
Figure 2.4 Propagation of a light beam through a polariser filter.	40
Figure 2.5 Propagation of light beam passing through a polariser filter and a quarter wave plate with an out put of Circularly polarised light.	44

Figure 2.6 Propagation of light beam passing through a polariser filter and a quarter wave plate with an output of elliptically polarised light.	46
Figure 2.7 Electromagnetic wave of a linearly polarised state.	48
Figure 2.8 Electromagnetic wave of a circularly polarised state.	48
Figure 2.9 Electromagnetic wave of an elliptically polarised state.	49
Figure 2.10 Intensity profile for linearly polarised light through a 180° rotation of analyser.	49
Figure 2.11 Intensity profile for circular polarised light through a 180° rotation of analyser.	50
Figure 3.1. Generation of vertically linear polarised light by passing a polariser filter.	54
Figure 3.2. Null intensity experiment by having two polariser filter with perpendicular optical axis to each other.....	55
Figure 3.3 The stage view with analyser filter 90° different to the polariser filter and without. A) Analyser filter in B) Analyser filter out.	56
Figure 3. 4 The view of birefringent material under cross polarised condition.....	56
Figure 3.5 Optical indicatrix sphere of isotropic material.	57
Figure 3.6 Optical indicatrix sphere of optically uniaxial material.	58
Figure 3.7 Optical indicatrix sphere of optically biaxial material.	59
Figure 3.8 Roll-Pitch-Yaw rotation diagram around 3 axes.	63
Figure 3.9 Formation of crystal orientations map by employing roll-pitch-yaw rotation around the reference point.....	64
Figure 3.10 Euler 1 Rotation of HCP crystal with fixed Euler 2 and Euler 3.....	66
Figure 3.11 Euler 2 rotation of HCP crystal system with fixed Euler 1 and Euler 2.....	67
Figure 3.12 Light path designed for the PLM technique, with a rotatable stage.	70
Figure 3.13 The microstructure of variant A viewed by bright field illumination in the etched condition (a) and polarised light (b) and EBSD (c) in the as polished condition.	73
Figure 3.14 The microstructure of variant B viewed by bright field illumination in the etched condition (a) and polarised light (b) and EBSD (c) in the as polished condition.	73
Figure 3.15 The microstructure of variant C viewed by bright field illumination in the etched condition (a) and polarised light (b) and EBSD (c) in the as polished condition.	73
Figure 3.16 The microstructure of variant D viewed by bright field illumination in the etched condition (a) and polarised light (b) and EBSD (c) in the as polished condition.	74
Figure 3.17 Qualitative observations of symmetry in the contrast of images recorded under circular polarised light microscopy.....	76

Figure 3.18 Intensity profile of an identical grain($\varphi_1=38^\circ$, $\Phi =62^\circ$) through 180° stage rotation.	77
Figure 3.19 Intensity profile captured through 360° rotation of analyser for different grains with certain crystal orientations. The value for Euler1 increasing gradually to highlight the correlation between Euler1 and intensity plots.	79
Figure 3.20 The Hexagonal Euler rotation representation for Euler 1 with fixed rotation for Euler2 and Euler3. A) Hexagonal unit cell with Euler angle reference vector. B) Euler angle set to 0° C) Roll Rotation representation with zero.	80
Figure 3.21 Euler 1 correlation between the position of maximum intensity through 180° of stage rotation.	82
Figure 3.22 The impact of second Euler rotation to the intensity profile for each specific grain through 360° rotation of stage under cross polarised conditions.	84
Figure 3.23 The Hexagonal Euler rotation representation for Euler 2 with fixed rotation for Euler1 and Euler3. A) Hexagonal unit cell with Euler angle reference vector. B) Euler angle set to 0° C) Pitch rotation representation with zero.	85
Figure 3.24 Euler 2 correlation between the maximum intensity value captured through 180° rotation of analyser and the rotation of Euler 2.....	86
Figure 3.25 The hexagonal Euler rotation representation for Euler 3 with fixed rotation for Euler1 and Euler2.	87
Figure 3.26 intensity change expected through the rotation around the c-axis.....	87
Figure 3.27 Colour correlation employed by PLM technique. Correlation between the intensity plots (figure 3.20 and 3.23) and crystal orientation map.	89
Figure. 3.28 The crystal orientations maps from the same sample area by using the PLM method and EBSD. A) represents the crystal orientation map by using the PLM method and B) illustrates Crystal Orientation Map by using the EBSD method.....	90
Figure 4.1 Optical path for CPLM where 1 is monochromatic light source, 2 is the linear polariser, 3 is quarter wave plate, 4 is a mirror with angle of 45° , 5 is the sample and 6 is 360° rotatable analyser.	96
Figure 4.2. Intensity plot captured from the mirror reflection of modified circularly polarized light microscopy through 360 degrees of analyzer rotations.....	98
Figure 4.3. Anodised surface transformation from aluminium to hexagonal alumina.	101
Figure. 4.4 The same area of interest under four different conditions A) Bright field with a LED light B) Circular polarized light microscopy with a LED light C) Circular polarized light microscopy with a monochromatic light.....	103
Figure. 4.5 Qualitative observations of symmetry in the contrast of images recorded under circular polarized light microscopy.....	103

Figure. 4.6 An intensity profile and its derivative for an individual crystal orientation recorded over a complete analyzer rotation.	104
Figure 4.7 Intensity profile captured through 360° rotation of analyser for different grains with certain crystal orientations. The value for Euler1 increasing gradually to highlight the correlation between Euler1 and intensity plots.	107
Figure. 4.8 The position of maximum intensity through 180 degrees of analyser rotation.	107
Figure 4.9 The impact of second Euler rotation to the intensity profile for each specific grain through 360° rotation of stage under cross polarised conditions.	109
Figure 4.10 The difference between the maximum and minimum intensity over 45° rotation of Φ	109
Figure 4.11 CPLM intensity data of Close C axis crystals orientations. Left intensity plot is $\phi_1=76$ and $\Phi=43$, Right intensity plot is $\phi_1=75$, $\Phi=43$	110
Figure 4.12 Correlation plots of CPLM data and EBSD data. A) Euler 1 correlation Plot represents the correlation between Euler 1 (ϕ_1) and analyzer rotation. B) Euler 2 correlation illustrates the connection between the difference of maximum and minimum intensity to the Euler 2 (ϕ).	111
Figure. 4.13 The effect of Φ rotation on the ellipse amplitude.	115
Figure 4.14 Correlation between ellipticity parameter and the difference between max and min intensity (ΔI value) for a) theoretically calculated ellipticity parameter and b) experimentally measured ellipticity parameter.	116
Figure 4.15. A) Formation of an elliptical ellipse by electrical field at the coordination of Ψ . B) Elliptical polarized ellipse corresponding to the intensity profile. Ψ is the orientation angle of the ellipse and X the measure of the ellipticity. a is the major axis and b is the minor axis.	117
Figure 4.16. Representation of polarization state of table 4.3 on a Poincare sphere. A) General format of Poincare sphere representing systematic range of polarization state. B) Representation of polarized ellipse in table 4.3 on Poincare sphere.....	117
Figure 4.17. The c-axis crystal orientations maps from the same sample area by using the CPLM method and EBSD. A) represents the crystal orientation map by using the CPLM method and B) illustrates Crystal Orientation Map by using the EBSD method.	120
Figure 4.18. The intensity plots from the same grain. A) First time anodisation data collected on every 5° of analyser rotation. B) Intensity plot of re-anodized grain, data collected on every 10° of analyzer rotation.	121
Figure 4.19 Compared data of maximum intensity position from the first anodisation and re-anodized sample.	122

List of tables

Table 1.1 Auguste Bravais 14 different unit cells of crystalline material.....	3
Table 1.2 Key differences between isotropic and anisotropic material.	9
Table 2.1 Stoke parameters of linear polariser through 180° rotation of optical axis.....	43
Table 3.1 Sample designation and microstructural description of the four different microstructures under investigation.	69
Table 4.1Composition of major elements in 2XXX	95
Table 4.2 The stoke parameter value for S1 and S2 over the rotation of 180° of analyser rotation.	112
Table 4.3. Ellipse structure and stoke parameters for different range of crystal orientation.	118

List of Symbols and Abbreviations

D density

M molecular mass,

Z number of molecules in each unit cell,

N_0 Avogadro's number

V unit cell volume

n refractive index of

v velocity of light

c light speed in the vacuum

$u_x(r, t)$ and $u_y(r, t)$ transverse components

$u_z(r, t)$ is the longitudinal component

u_{0x} , u_{0y} and u_{0z} maximum amplitudes

δ_x , δ_y and δ_z phases

$wt - k \cdot r$ propagator = τ

$E_x(z, t)$ and $E_y(z, t)$ resultant vectors

E_{0x} and E_{0y} maximum amplitudes

$E_x(t)$ and $E_y(t)$ instantaneous amplitudes

ω instantaneous angular frequency

$\delta_x(t)$ and $\delta_y(t)$ instantaneous phase factors

S_0 Total intensity of the light

S_1 The volume of linear horizontal or vertical polarised light

S_2 The volume of linearly polarised light $+45^\circ$ or -45°

S_3 volume of right or left circularly polarised light in the beam

S' Stokes vector of output light

M Mueller matrix

P_x and P_y amplitude transmission coefficients

λ wavelength of light

d is the thickness of the quarter-wave plate

N retardation

n_o ordinary refractive indices

n_e extraordinary refractive indices

σ_{ij} stress components

ε_{ij} strain components,

i direction of normal to the plane

j component direction

C_{ijkl} stiffness constant

S_{ij} compliances of the crystal

φ_1 Rotation about the Z-axis

Φ X-axis rotation

ϕ_2 Z-axis rotation

(SEM) Scanning Electron Microscope

(EBSD) Electron Backscatter Diffraction

(FCC) Face Centre Cubic

(BCC) Body Centre Cubic

(HCP) Hexagonal Close Pack

(CCP) Cubic Closest Pack

(LEDs) light-emitting diodes

(COMs) Crystal Orientation Maps

(PLM) Polarised Light microscopy

(CPLM) Circular Polarised Light Microscopy

(LCP) Left Circular Polarised

(RCP) Right Circular Polarised

(EBSP) Electron Backscatter Diffraction Pattern

Chapter 1: Introduction

The first chapter briefly describes crystallography and highlights the necessity of having access to the crystal orientation map. This chapter introduces anisotropic and isotropic crystallographic systems and their behaviour to when exposed to light and load in different directions. Different types of microscopies are discussed in detail, and later in this chapter, we introduce problems of generating crystal orientations maps by Electron Backscatter Diffraction.

1.1 Crystallography

Crystallography is a fundamental branch of science that deals with the geometric description of crystals and their internal arrangements. All solid materials in which the component atoms or ions are arranged in a highly ordered pattern in three-dimension are called a crystal(1–3).

Metal properties are highly dependent on the metallic bonding of the atoms in the crystalline lattice. This means fundamental metallic properties are due to free and mobile valance electrons in the lattice. Crystalline solids are recognised as materials in which atoms, ions or molecules arranged in the strictly periodic crystal structure at a large atomic distance. These atoms, ions or molecules are distinguished as lattice points and generally represented as round spheres. 90% of all naturally occurring and artificially prepared solids are recognised as crystalline types such as minerals, sand, clay, limestone, metals, carbon (diamond and graphite), salts (NaCl, KCl) Etc.(2). Amorphous or non-crystalline materials are distinguished as a solid which contains randomly oriented atoms, molecules or ions such as metals (non-crystalline material). Amorphous solids keep the order only within a few atomic distances e.g. glass, polymers and liquids. Crystal structure refers to how atoms

packed in a crystalline material can be represented in a few different ways. A perfect crystal maintains a particular crystal structure through the whole surface(1–6).

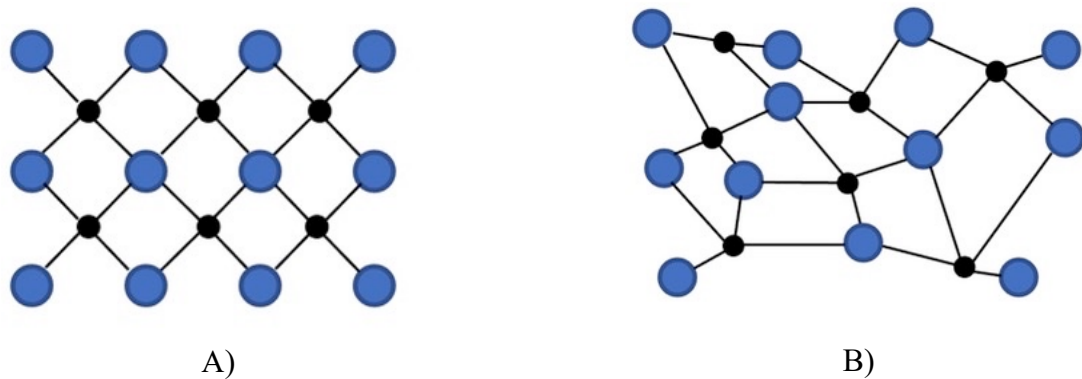


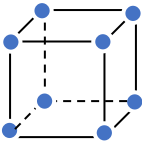
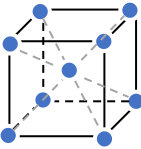
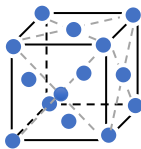
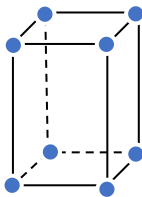
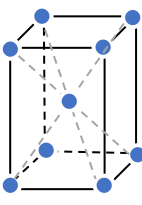
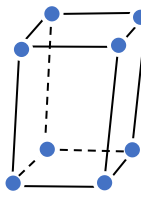
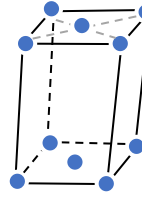
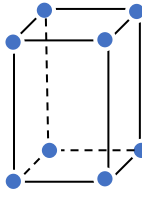
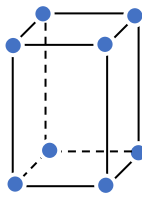
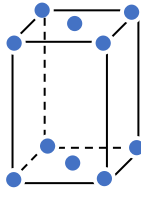
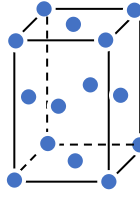
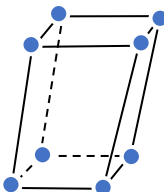
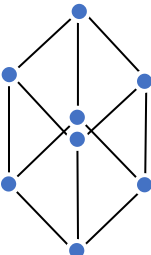
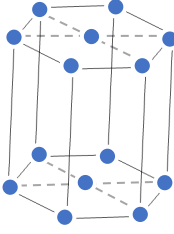
Figure 1.1 Representation of atoms positions in crystalline and amorphous material. A) crystalline material B) Amorphous material

Figure 1.1 represents the arrangement of atoms in a crystalline and amorphous material. A crystalline material is known as a material that consists of a massive number of atoms placed in completely arranged order with precisely repeated order in all directions. This type of symmetry, called translation symmetry, is the most fundamental character of crystalline material, and it can be defined by the lattice of the structure and given numerically in the parameters of a unit cell. A complete crystal structure can be classified by representing the content of a single repeating unit known as a unit cell(1,3,5).

1.2 Unit cells

The simplest and the most common way to describe the crystal structure is by using the unit cell, a periodic space and defines the position of lattice points in each unit. In 1850 Auguste Bravais introduces 14 different unit cells for crystalline material, which becomes the fundamental of modern crystallography. These 14 unit cells are represented in table below(7)(8)(4).

Table 1.1 Auguste Bravais 14 different unit cells of crystalline material.

Cubic			
Simple	Body Centre Cubic (bcc)	Face Centre Cubic (FCC)	
			
Tetragonal		Monoclinic	
Simple	Body centre	Simple	End face centre
			
Orthorhombic			
Simple	Body centre	End Face centre	Face centred
			
Triclinic	Rhombohedral		Hexagonal
			

1.2.1. Unit cell characterisation

Table 1.1 represents the 14 different unit cells that as represented by Auguste Bravais. The diffraction method for crystal structure determination is a fundamental approach to characterise materials between 230 available space groups. By measuring unit cell parameters in the early stages, the probable crystal system can be narrowed down quickly, and the final decision will be taken by measuring the intensity value. Critical sources help identify the information about the space group, such as the unit cell shape and the centring. Also, the Laue class for the complete diffraction pattern, the systematic absence (zero intensities) of specific subgroups of reflections in the data set, the statistical distribution of intensities, other physical properties of the material being studied, and any prior knowledge of certain aspects of the structure. By distinguishing the mentioned parameters, some assessment can be done regarding the number of atoms that can be accommodated in a unit cell. Also, by calculating the value of crystals density, then simply the mass contents of the unit cell can be measured from the cell volume(1,3,5,8,9).

The density of each unit cell can be easily found by using the equation below:

$$D = MZ/N_0V$$

Eq.1. 1

Where D is the density, M the molecular mass, Z the number of molecules in each unit cell, N_0 Avogadro's number, and V the unit cell volume (1,3,6).

Crystal structures for pure elemental metallic structures, which specify as a high packing density, contains 3 different types of unit cell which are FCC (Face Centre Cubic), BCC (Body Centre Cubic) and HCP (Hexagonal Close Pack) with high symmetry. Also, the neighbour distance is small; this is the reason to have significantly low bond energy; plus, metallic bonding is considered as non-directional bonding.

Two types of metallic crystal systems are investigated during this research which are HCP & FCC. These two types of crystal orientation are widespread between metals. For HCP, there are examples like Titanium, Zinc, Magnesium, Zirconium, Cadmium etc. Aluminium, Copper, Nickel, Gamma Iron, Gold, and Silver are familiar examples of the FCC crystal system. This research employed an Aluminium sample to represent the FCC crystal structure and a Titanium sample for the HCP crystal system because of their widespread application in aerospace, automotive and many other engineering applications(1–3,6,10–12).

1.2.1.1. Face Centred Cubic (FCC)

Cubic closest pack (CCP) is created by layering close-packed arrays. The FCC unit cell can accommodate 4 complete atoms.

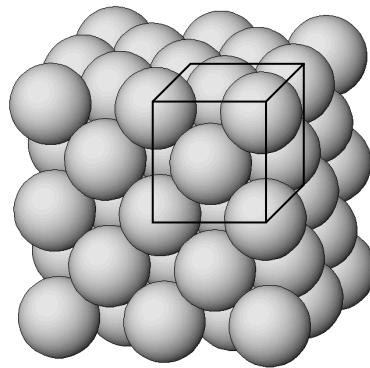


Figure 1.2 Position of atoms in FCC unit cells.

Figure 1.2 illustrate the position of atoms in the FCC unit cell. As can be seen from the figure, the location of the atoms is entirely identical and repetitive. Having access to the rotation of each unit cell can basically show how each atom placed in a polycrystalline material (1-3,5,6).

1.2.1.2. Aluminium

After oxygen and silicon, Aluminium is the third most common element in the earth crust, which occupied 8% of the earth crust. Also, Aluminium considered the most common

metallic element with high chemical stability and recognised as the lightest metal. Another significant character of Aluminium is the low density, one-third the density of steel with even strength. Industrial wise is common to use Aluminium alloy instead of pure Aluminium. This is because Aluminium alloy offers a higher strength to weight ratio compared to pure aluminium. Also, alloys form of Aluminium can improve the stress corrosion cracking and fatigue resistance. Other mechanical properties that would be highly enhanced in alloys format is stiffness and resistance to bending. All these characters identify Aluminium as a material that dominates the industry (13,14).

In 1906, Dr Alfred Wilma (a German metallurgist) discovered that the presence of copper with the correct heat treatment can substantially improve the mechanical properties of Aluminium. This type of aluminium alloy recognised as Duralumin, where Duren is a small city in North Rhine-Westphalia. By 1906 metallurgists already had great successes to improve the mechanical properties of pure metals by creating alloy format. Such as, the addition of Carbon into Iron with correct heat treatment would form steel which has significantly better mechanical properties. Also, the presence of Tin in Copper can substantially improve mechanical behaviour (1,4,8,10,13,15). Aluminium is classified as a face centered cubic unit cell which is a close pack arrangement. (5,18,19)

1.2.2.1. Hexagonal Close Packed (HCP)

7 Lattice points are presented on the top plane of the HCP unit cell 6 of them on each corner of the hexagonal plane and one in the middle. The same lattice point position is happening on the bottom plane, and this is the reason to form a hexagon around a central atom (1,2,6,18,19). The position of atoms in a hexagonal closed pack crystal system illustrated in figure 1.3.

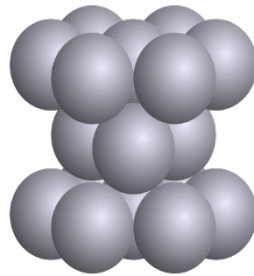


Figure 1.3 Position of atoms in HCP unit cells.

1.2.2.2. Titanium

Titanium was classified as a low-density element recognised in 1791 by William Gregor, the British chemist and mineralogist. Ti placed as the fourth abundant metal in the crust with high melting temperature (1688° C), with a corrosion resistance in many aggressive atmospheres and carrying its exceptional mechanical properties over an extended range of temperature offers significant advantages to turn Ti into one of the favourable elements in engineering applications. Titanium alloys are divided microstructurally into an α type consisting of pure α phase with HCP crystal structure, a β type consisting of just β phase with BCC structure and $\alpha+\beta$ phase.

Titanium alloys became the crucial material of aircraft engines after the second world war, and even now, the aerospace industry is the leading consumer of Titanium-based alloys. However, many other markets are interested in Titanium alloys like architecture, chemical processing, medicine, power generation, marine and offshore, sports and leisure, and transportation are gaining increased acceptance (1,5,6,20–24).

1.3. Isotropic and anisotropic material

Metals are distributed into a single crystal and polycrystalline. In single-crystal metals, the mechanical properties vary with the orientation of the unit cell (25). However, if unit cells are distributed randomly in polycrystalline metal, the material is isotropic because the mechanical properties would be a function of a bulk average response to a materials texture (or predominant average crystallographic orientation) rather than the properties of specific slip systems.

However, the polycrystal metals containing texture regions of the microstructure consisting of many grains are anisotropic. The orientation of each unit cell becomes crucial to understanding the behavior of the material corresponding to the load direction. In this case properties vary along with their crystal structure. The textured or directionally microstructure typically causes during the forming process (1,3,5,26-29). Also grain size has a measurable effect on most mechanical properties. For example, at room temperature, hardness, yield strength, tensile strength, fatigue strength and impact strength all increase with decreasing grain size. The Hall–Petch relationship clearly explains the effect where we could achieve strength in materials that is as high as their own theoretical strength by reducing grain size.

Machinability is also affected, rough machining favors coarse grain size while finish machining favors fine grain size. The effect of grain size is greatest on properties that are related to the early stages of deformation. Thus, for example, yield stress is more dependent on grain size than tensile strength.

Materials are divided to optically isotropic and anisotropic as well. Where we can distinguish them by reflectance behavior to different light directions(33-35).

Table 1.2 Key differences between optically isotropic and optically anisotropic material.

Character	Isotropic material	Anisotropic material
Appearance	Mineral isotropic looks dark	Mineral anisotropic looks light
Chemical Bonding	Consistent and uniform	Inconsistent and different
Light penetration	No	Yes
Refraction	Single refractive index	Have many refractive index
Speed of light	Consistent regardless of the direction	Varies regard of the direction
Directional properties	Identical in all direction	Different properties in different direction
Structure	Equal	Unequal
Polarization properties	Does not split unpolarized light. Used in lenses and windows.	Splits unpolarised light into two when it passes through an anisotropic medium. Used for polarizer, optical waveplates.
Example	Cubic crystal and amorphous materials, like glass	Wood, rocks composite material and all crystals except cubic crystals. Used for polarizer, optical waveplates.

Table 1.2 illustrates the main differences between optically isotropic and anisotropic material. These differences are the crucial points for this research, such as the polarisation properties of anisotropic material response to the light direction (1–3,5,24,30).

1.4. Unit cell orientation effect on mechanical properties of polycrystalline material

The orientation of the unit cells plays a vital role in the mechanical properties of textured polycrystalline material and single crystal materials; this is well documented by many

researchers. Polycrystalline material recognized as the material consists of grains with different sizes, shapes, different crystal orientations and arrangements which can be observed under microscopes. Presence of preferred crystal orientation in a polycrystalline material recognized as texture in the material (5,14,19,24,31).

The mechanical properties of materials distinguished from those physical properties that react with applied load. Most of the mechanical properties can be highly affected by crystal orientations, such as strength, toughness, hardness, ductility, creep, fatigue, etc. Plastic deformation in metallic alloys often occurs via slip on a limited number of crystallographic systems. Each system is defined by a crystallographic plane and a direction of relative motion of the atoms lying on opposing sides of the plane. For example Hexagonal and cubic symmetry leads to considerable anisotropy in the elastic and plastic mechanical properties of HCP metals, as well as other physical properties. Having access to the crystal orientation maps can highly improve the understanding behind the material mechanical properties.

1.5. Crystal Orientation Maps (COM's)

Choosing a suitable material for different application is a critical approach which needs to be done carefully. Having identified the strong interrelation between crystal orientation and mechanical properties it is understandably important to be able to accurately characterise the orientation of the grains within it. This can be determined through bulk texture measurements (predominantly via x-ray diffraction) or through spatially resolved microtexture measurements (predominantly (in recent times) via EBSD). The latter can be used to determine the crystal orientation grain by grain and can be visualised in the form of crystal orientation maps. The particular crystal orientation measurements performed by crystal orientation mapping can illustrate the texture area in a polycrystalline material. The electron beam scanned over the sample and revealed the orientation of each crystal. The

final crystal orientation map employs a qualitative and quantitative approach to interpret the behaviour of a polycrystalline material under different load and atmospheres conditions (3,6,31,32,46).

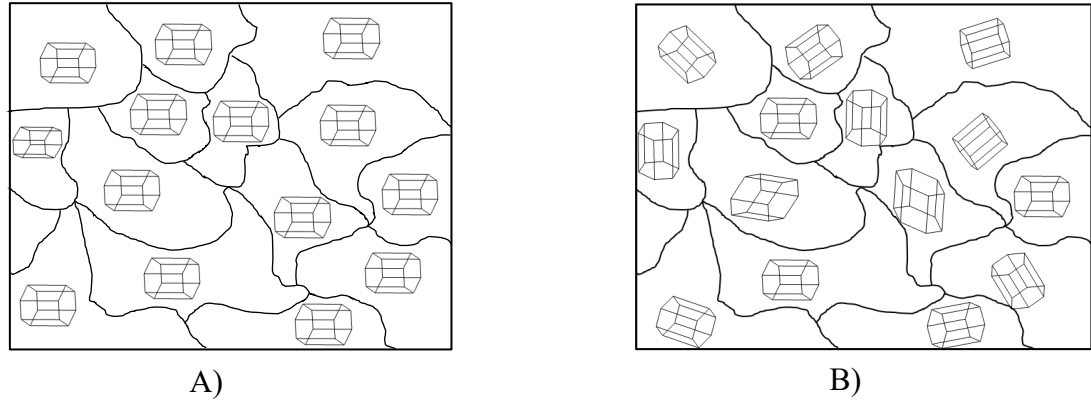


Figure 1. 4 Crystal orientation map (COM) of isotropic material. A) COMs of completely ordered crystals B) COMs of randomly orientated crystals.

The effect of unit cell orientation on mechanical properties was highlighted previously by many researchers (47,48). Many laboratory-based investigations have highlighted qualitative and quantitative links between loading direction and mechanical performance in materials of high bulk texture throughout a broad spectrum of load regimes (49–51). In parallel, studies on the microtexture of titanium using crystal orientation mapping via EBSD have revealed that bulk texture in these materials is dictated by large areas of common orientation often referred to as either microtexture or macro zones (52). These two research themes have precipitated the concept of effective structural units in which microstructure, microtexture and load regime are decisive contributory factors (53).

These two research themes have precipitated the concept of effective structural units in which microstructure, microtexture and load regime are decisive contributory factors (53). Consequently, the determination of microtexture (i.e. macrozone size, morphology and texture intensity) is as much important as conventional microstructural assessment in the characterisation of aluminium and titanium.

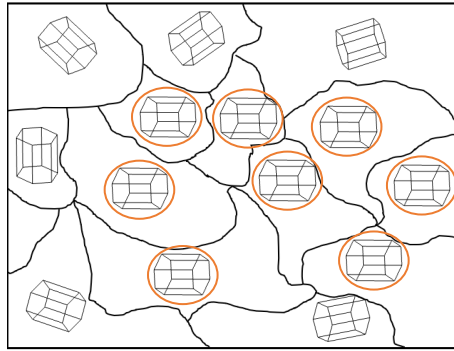


Figure 1.5 Crystal Orientation Map of textured polycrystalline material.

Figure 1.3 represents hexagonal textured polycrystalline material. The highlighted crystals represent the microtexture or macrozones area. In this case, the sample has an anisotropic behaviour as a large micro area have the same crystal orientations.

1.6. Microscopy

The resolution of human eyes is about 0.2mm, and the microscopes helps to improve the resolution up to atomic level. Two main types of microscopy technique were used during this research to produce the results which are, optical microscopy and scanning electron microscopy. Some of the main differences between these two types of microscopies discussed in detail, and those differences are the crucial importance to use a suitable microscope for a particular application (54–57).

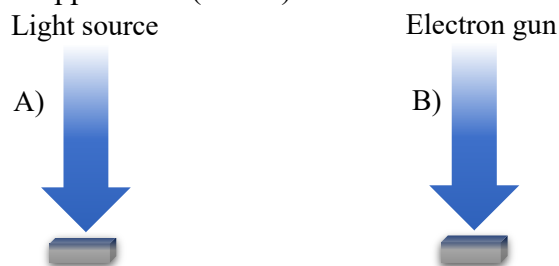


Figure 1.6. simplified source types of different type of microscope. A) optical microscope
B) Scanning Electron Microscope.

1.6.1. Light or optical microscope

It is a laboratory instrument that detects and magnifies microscopic objects using the visible section of the electromagnetic spectrum. This type of microscopy has been available for the past two centuries, from a simple device with limited abilities to a more recent complicated version that offers extensive capabilities. Magnified images created by visible light waves transmitted, absorbed, reflected, or refracted from the sample. Different types of observation are available in light microscopy such as brightfield, darkfield, phase contrast, polarising, DIC, epi-fluorescence and confocal laser scanning. Two primary forms of illumination are available for different applications, which are transmitted and reflected light microscope. Transmitted light illumination (see figure 1.7A) is a recognised type of microscopy for thin samples and polarisation examination as the light passes through the sample, unlike the reflected illumination where the light reflected from the specimen surface. Reflected light illumination (see figure 1.7B) are suitable for surface examination, thick samples, metallic samples, and ceramic samples. (55,56,58,59).



Figure 1.7 Light path for reflected and transmitted light microscope. A) Transmitted light microscope B) Reflected light microscope.

1.6.1.1. Objective lenses

It is responsible for gathering the light reflected or transmitted through the specimen and form an accurate, actual, inverted image of the specimen. Also, objective lenses can accommodate other external devices such as wave plate, polariser filter, darkfield microscopy and correction collar. Typically, 3 to 4 objective lenses attached to an optical microscope with different magnification (Typically with the power of 4x, 10x, 40x and 100x). The shortest lenses have the lowest strength, and the taller lenses have the highest power (54,59,61).

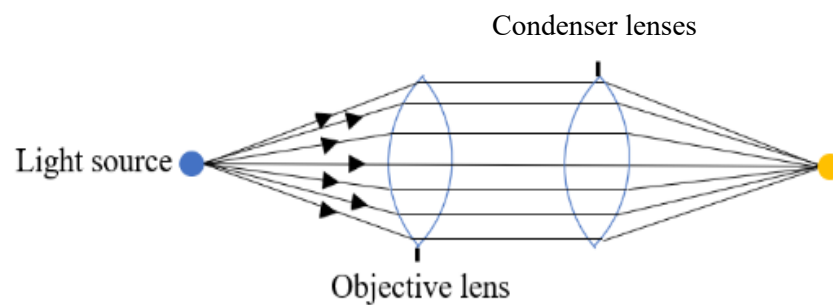


Figure 1.8 Objective lenses diagram for optical microscope.

1.6.1.2. Eyepiece lenses

Eyepiece lenses are the lens at the top of the microscope used to look at the focused area and magnify the real image projected by the objective lens. Generally, the eyepiece lens

can magnify the actual image by 10x. If the objective lens used to project an image has the power of 40x, the final magnification power would be 400 (15,54,56,61).

1.6.1.3. Condenser lenses

The fundamental responsibility of condenser lenses is to collect the light generated by the light source and focus that light from every azimuth onto the sample. The collected light concentrates at the back of the focal plane of the objective lenses (15,54,56,57).

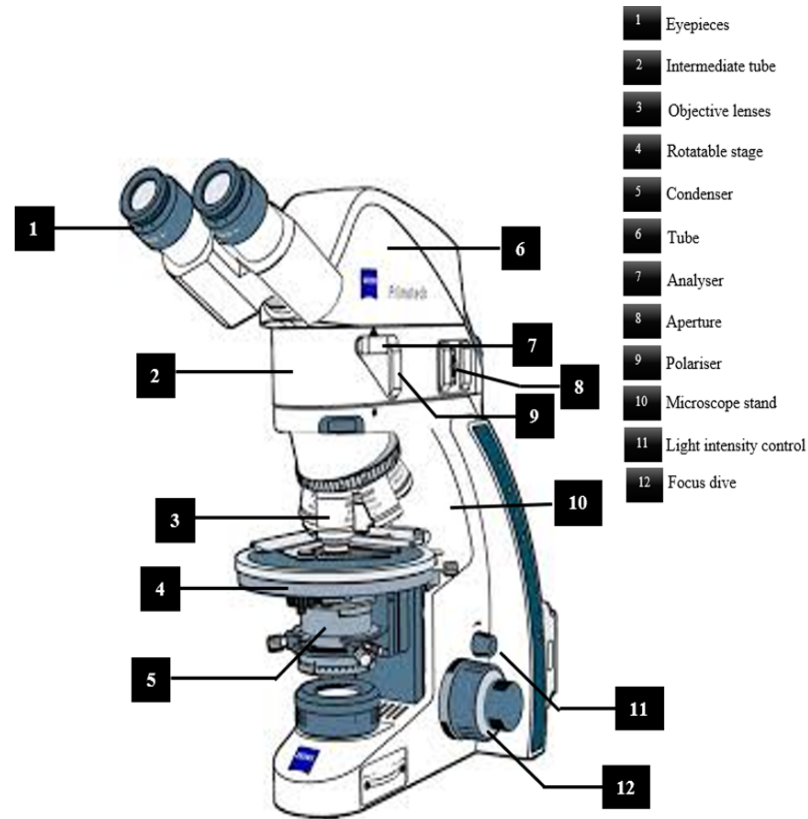


Figure 1.9. ZEISS Primotech microscope diagram.

1.6.1.4. Light source

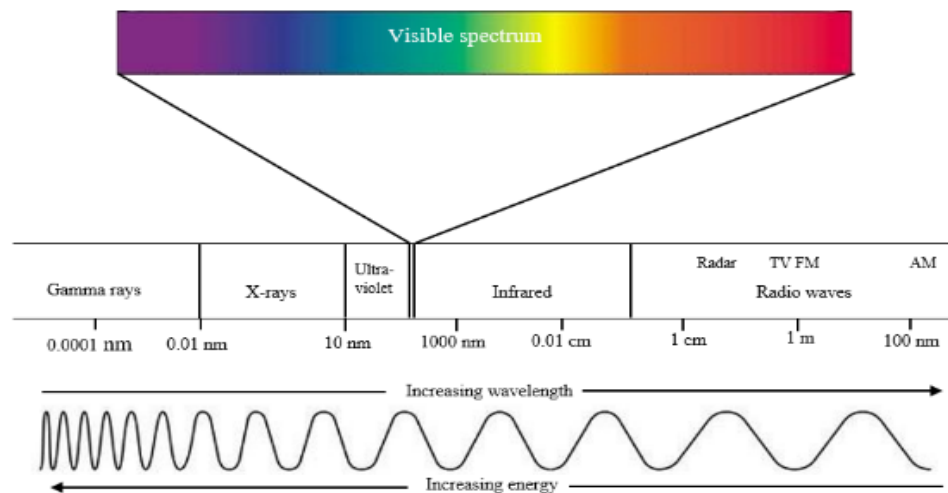


Figure 1.10 The range of frequencies of electromagnetic radiation and their respective wavelengths and photon energies.

Figure 1.10 shows all ranges of frequencies of electromagnetic radiation and highlights the visible spectrum. Optical microscopy uses different types of a light sources to visualise the structure. Such as halogen light, white LED light and monochromatic light (3).

1.6.1.4.1. Halogen light

Tungsten-halogen lamps have been the prominent and reliable light source for optical microscopes for many decades, and the first halogen light with tungsten filament used commercially goes back to 1900. This light source generates a continuous distribution of light through the visible spectrum, which would provide a distinct colour contrast from the specimen surface. However, most of the generated energy will be wasted as heat in the

infrared wavelength (up to 85 per cent), and 15 to 20 per cent of the emitted energy lies in the visible spectrum (400 to 700 nanometers) only 1 per cent or less falls into the ultraviolet (below 400 nanometers). This type of lamp is suitable for brightfield examination, photomicrography, reflected light application, and digital imaging of stained cells and tissue sections. In the polarisation field, the high power of tungsten-halogen used to provide enough light intensity passing through crossed polarisers. This helps for birefringence measurements and particle identification (3,60–62).

1.6.1.4.2. White LEDs

The first white light-emitting diodes (LEDs) was offered to the market in 1996. Unlike early examples, which emit monochromatic light, white LEDs emit polychromatic light. There are several ways to generate white LEDs. The first way is to employ ultraviolet or violet LED chip and phosphor and convert that into a broadband white light. The second approach uses three different LED chips, emitting the main three primary colours (Red, Green, Blue) mixed to create white light. The third and most common way is to employ a single blue LED chip with phosphor combinations where phosphor emits red and green light. Part of the blue light generated by the LED chip absorbed by the phosphor, and the remaining blue light transmitted through the phosphor. The blue light emitted from the LED chip will join the red and green light emitted from the phosphor and generates white light (60,63). This type of light source will provide much more consistent light to the sample surface also the colour shift can be minimised as the light source has narrower spectrum.

1.6.1.4.3. Monochromatic LEDs

During the past decade, the LEDs technique developed extensively and highly improved luminous efficiency. The monochromatic LEDs are available for any wavelength through the visible spectrum, and researchers can now select a suitable wavelength that would be ideal for specific applications (63,64). Monochromatic light must be employed to generate purely circular polarised light and isolate any colour shift by rotation of the polariser filter.

1.6.1.5. Magnification development

The magnification power of a microscope varies highly dependent on the numbers and types of lenses. The first optical microscope was built in 1595 by Hans and Zacharias Janssen, a two-lens microscope. Before the seventeenth century, lenses were made out of rough magnifying glasses and the evolution of modern microscopes, Antoni van Leeuwenhoek (1632–1723). He improved the lenses quality by using 1.5 mm glass sphere magnifiers - protozoa and increasing magnification to 300x in his simple microscope. According to Willebrod Snell (1591-1626), the light beam bends when crossing the surfaces of two media with different optical densities (56,59).

$$n_1 \sin \theta_1 = n_2 \sin \theta_2$$

Eq.1. 2

θ_1 and θ_2 are the angles formed by the ray and the normal to the surface at the point of incidence into mediums 1 and 2, respectively, and n_1 and n_2 are the refractive indexes. The refractive index n of a material is related to the velocity of light v in the same material: $v = c/n$, where c is the light speed in the vacuum (59).

This equation was the fundamental of using thin lenses in optical microscopes, which highly magnified the power of lenses in refraction concepts.

1.6.2. Scanning Electron Microscope (SEM)

The scanning electron microscope (SEM) functions similar to a light microscope except that they employ electrons instead of light to image a specimen and extract information from a specimen. SEM is one of the well-known instruments in material research as it provides crucial information about materials topographical features, morphology, phase distribution, compositional differences, crystal structure, crystal orientation, and the presence and location of electrical defects. The scanning electron microscopes are consisting of two main parts, the electron column and the electronic cabinet. Modern optical microscope magnification can reach 1000x, which enables the eye to separate two resolve objects by 0.0002 mm, and the main concept behind upgrading the technique into an SEM is to go to higher magnification up to 1,000,000x and improve the resolution up to 1 nm. SEM also provides a higher depth of field (49,50,60,61).

1.6.2.1. Electron Column

In scanning electron microscopy, the electron beam scans the sample in a raster pattern. First, electrons are generated at the top of the column by the electron source. These are emitted when their thermal energy overcomes the work function of the source material. They are then accelerated and attracted by the positively-charged anode. The entire electron column needs to be under vacuum. Like all components of an electron microscope, the electron source is sealed inside a special chamber to preserve vacuum and protect it against contamination, vibrations, and noise. Besides protecting the

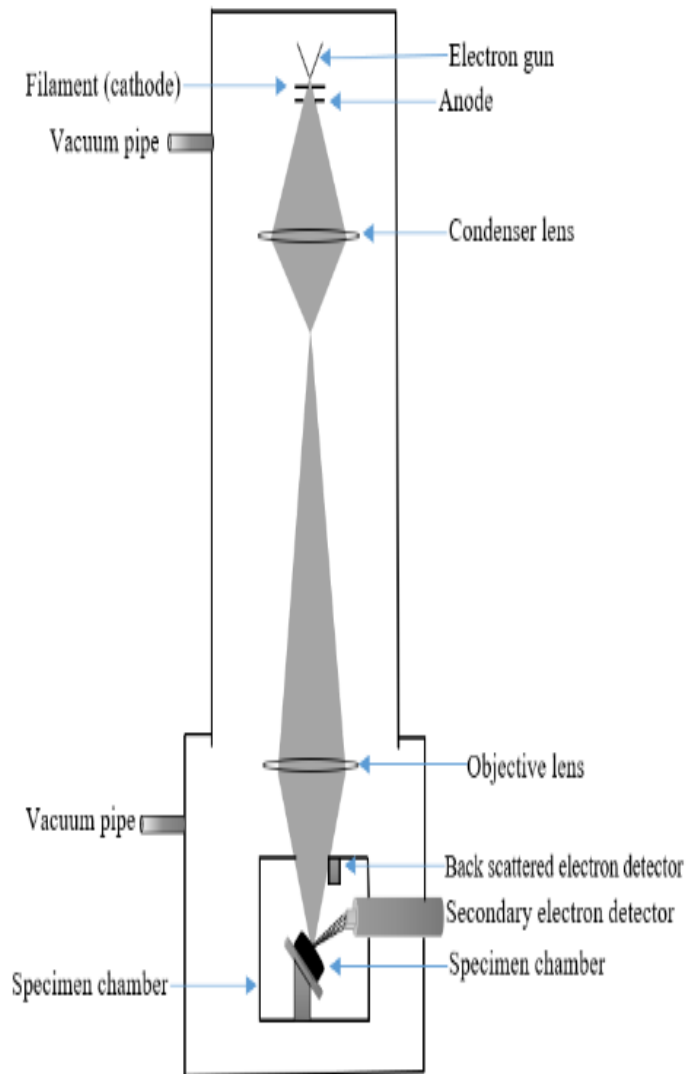


Figure 1.11 Figure: Simplified schematic of scanning electron microscope

electron source from being contaminated, vacuum also allows the user to acquire a high-resolution image. In the absence of vacuum, other atoms and molecules can be present in the column. Their interaction with electrons causes the electron beam to deflect and reduces the image quality. High vacuum also increases the collection efficiency of electrons by the detectors that are in the column. (55,65–68).

1.6.2.2. Electron gun

The electron gun provides a stable source of electrons, which is used to form the electron beam. electron guns use thermal energy to emit electrons from the cathode. If the filament (made of tungsten or LaB6(which requires a higher vacuum level)) is heated with joule heat (about 2800K), the free electrons inside the filament acquire thermal energy to exceed the work function, which is the energy difference between an electron at the Fermi level and that in vacuum. The electrons are emitted from the filament surface to vacuum, and then travel towards the anode under the acceleration voltage (V_{acc}) between the cathode and the anode(37,38).

1.6.2.3. Condenser lens

In a similar way to optical microscopes, lenses are used to control the path of the electrons. Because electrons cannot pass through glass, the lenses that are used are electromagnetic. They simply consist of coils of wires inside metal pole pieces. When current passes through the coils, a magnetic field is generated. As electrons are very sensitive to magnetic fields, their path inside the microscope column can be controlled by these electromagnetic lenses simply by adjusting the current that is applied to them.

The beam passes the anode affected by condenser lenses which enables us to adjust the diameter of the electron beam by that we mean to converge and pass the beam through a focal point. This provides the capability to focus the electron beam down to almost 1000 times its former diameter. The aperture is located between the condenser and objective lens, made of a thin metal plate with a small hole. The condenser lens defines the size of the electron beam (which defines the resolution), which is the fundamentals of controlling the electron probe diameter and the probe current (61,65,66,68).

1.6.2.3. Objective lens

The objective lens in SEM is responsible to determine the final diameter of the electron probe by focusing the electron beam on the sample surface. This is the final touch, and despite all the careful actions taken previously, this step needs to be taken very accurately to form the final image in high quality (44,54-56).

1.6.2.4. Sample stage

The sample stage is placed stably in the sample chamber, located on the lower side of the column. The stage can move in a different direction as it follows: The X and Y (horizontal movement) to select field of view, Z (vertical movement) used to improve the image resolution, specimen tilt up to 90° and rotation (44,50,54,56).

1.6.2.5. Electron beam and sample interaction

The interaction of a high energy electron beam with the specimen will produce various effects resulting in a range of signals being emitted. The incident electrons interact with specimen atoms and are significantly scattered by them. SEM utilizes an electron beam to image a sample and generate X-rays for compositional analysis. The region where this occurs is the interaction volume which provides information on specimen composition, topography, crystallography local magnetic field and electrical potential. The interaction volume depth and size are dependent on the type of signal that is detected and the accelerating voltage of the beam. Before SEM was invented, some of the essential physics of electrons scattering was investigated. Two types of electrons are used μ electrons result from the emission of the valence electrons of the constituent atoms in the specimen. The secondary electrons are extremely sensitive to the surface (top 100 nm), where only those created on top of the sample's surface are emitted outside of the specimen. The inelastic

interaction is responsible for the production of secondary electrons and it takes place between the incident electrons and the outer (not strongly bound) electrons of the atoms. These outer electrons can be ejected from the atom with energies lower than 50eV. The Everhart-Thornley detector is the most frequently used device for the detection of Secondary electrons. It consists of a scintillator inside a Faraday cage, which is positively charged and attracts the secondary electrons. The scintillator is then used to accelerate the electrons and convert them into light before reaching a photomultiplier for amplification. The secondary electron detector is placed at the side of the electron chamber, at an angle, to increase the efficiency of detecting secondary electrons. Backscattered electrons result from an elastic collision (around 1 μ m) and scattering reaction between incident electrons and specimen nuclei or electrons. In elastic scattering the electron trajectory changes, but its kinetic energy and velocity remain essentially constant (due to large differences between the mass of the electron and nucleus). Backscattered electrons help to resolve topographical contrast and atomic number contrast with a resolution higher than 1 micron(41.42). The backscattered electrons detectors are placed above the sample, concentrically to the electron beam in a doughnut arrangement to maximize the collection of the backscattered electrons. When all parts are enabled, the contrast of the image depicts the atomic number of the element. When only specific quadrants of the detector are enabled, topographical information from the image can be retrieved. Two major factors control which effects can be detected from the interaction volume. Firstly a beam of electrons lose energy as they traverse the sample due to interactions with it and if too much energy is required to produce an effect, it will not be possible to produce it from deeper portions of the volume. Secondly the degree to which an effect, once produced, can be observed is controlled by how strongly it is diminished by absorption and scattering in the sample. For example, although secondary and Auger electrons are produced throughout the interaction volume, they have very low energies and can only escape from a thin layer near the sample's surface. While several types of signals are generated from a specimen under an electron beam, the x-ray signal is typically the only other signal used for scanning electron

microscopy. The x-ray signal is a result of recombination interactions between free electrons and positive electron holes that are generated within the material (43,55,66–69).

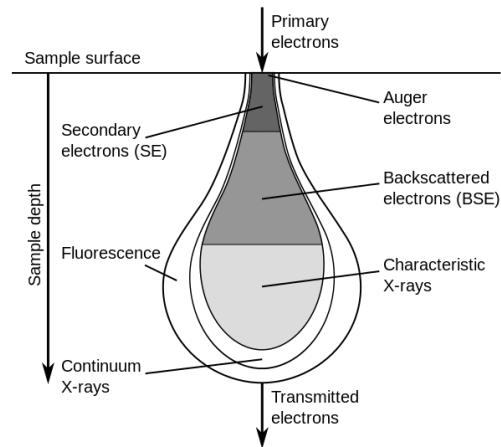


Figure 1.12 The interaction volume of an electron beam on a sample.

1.7. Electron Backscatter Diffraction (EBSD)

EBSD is a widespread laboratory-based technique employed to identify crystals' orientation from crystalline samples(70). EBSD also considered an accessory tool attached to an SEM and identifies quantitative microstructure information of crystallographic material. Such as grain size, grain boundary character, grain orientation, texture, and phase identity of the sample under the beam. The sample size depends on the SEM stage ability, and the stage orient a sample at 70° tilt within an applicable working distance, generally between 4 to 20 mm. The fundamental discovery of EBSD goes back to 1928 when Shoji Nishikawa and Seishi Kikuchi directed a beam of 50 keV electrons from a gas discharge on a cleavage face of calcite at a grazing incidence of 6° . Diffraction patterns were recorded on photographic plates placed 6.4 cm behind the crystal, normal to the primary beam. The poor quality of the pattern is due to the sample contamination causing by poor vacuum instruments (71–73). Nine years after Boersch managed to create some clear patterns recorded on a film by improving the vacuum condition with a condition of (at 20 kV, $\sim 5^\circ$ of incidence and up to 162° of acceptance angle), the data collected from polished and etched samples (NaCl, KCl, PbS, CaCO_3 , CaF_2 , quartz, mica, diamond, Cu, and Fe) surfaces (67–69,71,73).

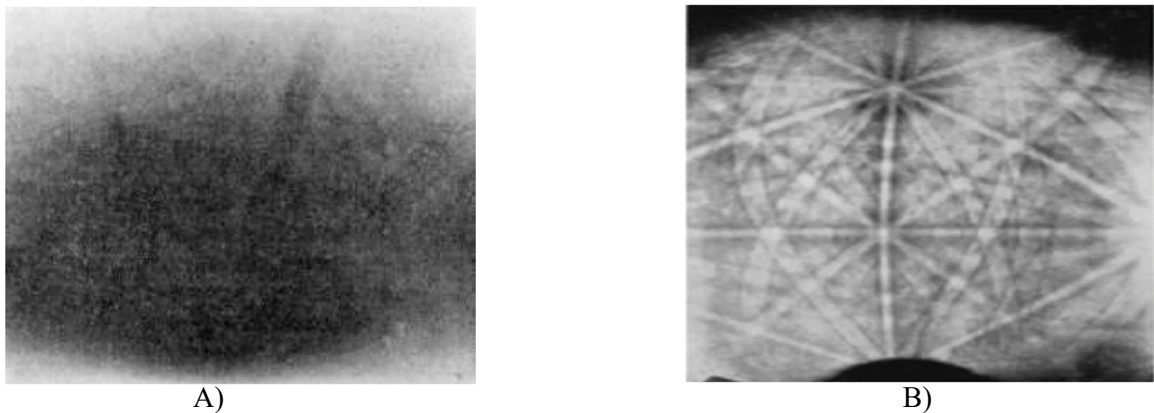


Figure 1.13 A) Shoji Nishikawa and Seishi Kikuchi Diffraction of Cathode Rays by Calcite. Nature 122 (1928) 726 B) Backscatter Kikuchi patterns obtained from fluorspar (fluorite). H. Boersch 1937.

1.7.1. How EBSD works

All EBSD works done in Carl Zeiss Crossbeam 550 with Oxford Instruments EBSD on Aztec. In the most common method for a microstructural EBSD, the high energy electrons interact with a tilted (70° toward the EBSD camera) crystalline sample, which means that the surface topography/relief must be kept an absolute minimum to avoid shadowing problems.

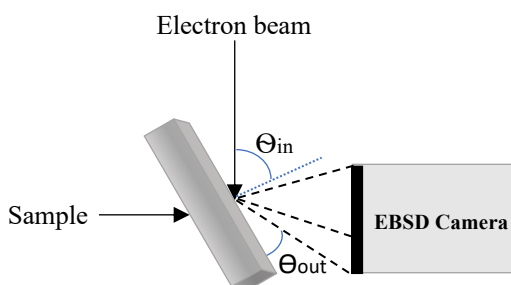


Figure 1.14 Simplified system for EBSD detector.

As can be seen from figure 1.10, EBSD is a surface-sensitive technique and analyses the signal coming from the top few nanometres of the crystal lattice. This is why having very distinguished sample preparation for EBSD to collect accurate EBSD data as the surface should be free of any damage, contamination, and oxidation. When the electron beam strikes the sample surface with a range of acceleration voltage between 15 to 25 Kv and incident current beam from 1 to 15 nA, it causes electron diffraction by the crystal lattice at the incident point on the specimen surface. The sample forms Electron Backscatter Diffraction Pattern (EBSP) in all directions and collected by EBSP detector. The EBSP detector is a digital camera, and the CCD chip of the camera is illuminated by a phosphor screen that intersects with a spherical pattern. The diffracted electron converts into light by phosphor screen, which is appropriate for the CCD camera to record. The lattice parameter of each specific crystal under the electron beam is determined by comparing the recorded EBSP after translation to Hough space to that of simulated patterns. The best fitted

simulated EBSP can be identified by matching the crystal orientation and the possible identities. This process repeats in stepwise fashion over the surface until the whole selected area examined and the Crystal Orientation Map (COM) generated for each specific crystal under the electron beam (69,70,73–75). The technique is capable of providing an unambiguous quantification of crystal orientation with sub degree resolution, though the practical accuracy and precision of the technique are closely related to calibration quality, SEM stage control and sample preparation.

1.7.2. EBSD applications

Materials commonly used in industrial applications like aluminium and titanium are polycrystalline, which is essential to analyse their microtexture in detail. In this case, electron backscatter diffraction is the only available technique to provide the information necessary to characterise the behaviour of a polycrystalline material in different conditions. Electron Backscatter diffraction (EBSD) provides information about the specimen's microstructure, such as the illustration of microstructure for grain size and grain/subgrain and phase distribution. Regions of distinct local texture, crystallographic texture determination, local strain determinations, and accurate identification of minor phases. The texture illustrates the crystal preferred orientation and the microstructure of the crystalline sample and some of the crucial applications of using EBSD in material research represented below. Most of these applications are directly related to the texture or the influence texture can have on it (10,19,24,48).

- Texture computation in sheet materials of Aluminium and steel for quality application.
- Used for improving the formability and surface finish of aluminium sheets.
- Study of texture concerning electrical and magnetic properties.

- Grain boundary effect on corrosion, fracture, and fatigue in metal manufacturing.
- Second phase particles analysis and orientation measurement of material.
- Texture microscopic studies that relate of macrotexture to microstructure.
- Analyse recrystallisation in metals and alloys.
- Studying the capability of crystal orientation maps to reveal the presence, location, and grain size of grains unambiguously.
- Grain boundary misorientations and influence of grain boundary types to segregation, corrosion, precipitation, fatigue and fracture resistance.
- Impact of grain boundary properties on fracture.
- High-temperature superconductors, including the influence of texture and grain boundary type on superconducting properties.
- Orientation of secondary phases and precipitates.
- Phase identification, discrimination and fraction determination, including analysis of intermetallic materials, carbides, and hydrides.

Some of the applications for EBSD been discussed. However, there are significantly more applications that can be considered here and this can highlight the necessity of having access to the crystal orientation map in metallurgy and material science (6,10,19,24,36,39,40,47,48,74,76–79).

1.8. Problem statement

Although EBSD is a recognised technique to generate a crystal orientation map, it doesn't mean it is free of disadvantages. There are critical limitations that prevent researchers and companies from having access to the COM of material. The limitations can be mentioned as:

1.8.1. Simplicity

EBSD is now a common microanalytical technique which is employed as an accessory tool attached to the SEM. This would occupy ample space, and the room needs to be under precise control such as humidity, pressure, and temperature control. EBSD is a complex laboratory technique that requires days of training to be qualified on EBSD for a high technical skilled researcher. Also, to start training on EBSD, you need to be an expert on SEM. The complexity of the EBSD is not limited to data acquisition. Researchers face complications when they carry out data processing. During the past 20 years, different software introduced to the materials world such as Tango, TSL, Mambo, Salsa to solve this difficulty, however, each of these applications required expertise to get the correct results (70,73,75). The post-processing software's are not free of limitations in data processing and errors which will be discussed later.

1.8.3. Speed limitation

Speed is determined by the time to spend from the first stage, sample preparation, to the final stage, a data representation, in all phases for EBSD method such as sample preparation, laboratory work data processing and data post-processing takes such a long time to generate a set of reliable data. In the PLM technique, we significantly decrease the acquisition time where the tilting is complex and a large area requires stitching the EBSD technique.

1.8.4. Source limitation

Uses electrons with a wavelength of 1 nm to have a high resolution. The source limitation unable the access of measuring the crystallography of thin films with EBSD. The X-Y resolution of SEM is better than the Polarised Light Microscope, but the Z (depth) resolution is worse as the interaction volume is higher.

1.8.5. Cost

EBSD detector must be attached to an SEM, which is very expensive to purchase with a high maintenance cost. This would prevent most low-budget companies or middle-class companies from having access to the crystal orientation map (11,72,80). Two types of optical microscopes was employed in this research which are Primotech Upright Microscopes (£13000) and ZEISS AXIO Observer Z1 Inverted Microscope (£90000). Whereas the SEM employed during this research FEGSEM (£450000) and Crossbeam FIB-SEM (£900000) are significantly more expensive compare to the optical microscopes.

1.8.7. Sample condition

The sample must be fixed, conductive only and no oxide layer on the surface. Also, a a very thin specimen can be used because the tilting condition and limited area can be examined as this process is such a time-consuming process. The non-conductive sample must be coated with carbons to conduct (55,66,70).

1.8.8. Beam damage

This might not be that crucial for metallic samples; however, this could become critical in soft and geological materials (10,68,70).

The considerations highlighted above were part of the motivation for this research to introduce a novel approach by polarised light microscopy (PLM) to investigate the crystal orientation of polycrystalline material. The PLM method applied on the HCP and FCC crystal system and the crystal orientation map generated by the PLM approach compared directly to EBSD data to prove the data set's reliability and consistency. This PhD thesis introduce an alternative approach to investigate the crystal orientation of Titanium alloy and Aluminium alloy. The alternative approach will be compared directly to EBSD and the advantage and disadvantage of each technique will be discussed in details. The PLM approach tries to introduce a more accessible and cost effective approach to have access to the Crystal Orientation Maps.

CHAPTER 2 Polarised Light Microscopy Method

This chapter details the fundamental of polarised light microscopy and represents the approach to create linearly, elliptically, and circularly polarised light. Also, the theoretical approach of creating polarised light and analysing the polarised light parameters are discussed in detail.

2.1. Polarised light

The process which transforms un-polarised light to polarised light is known as polarisation. Polarisation is one of the fundamental properties of light next to intensity, coherence, and wavelength. In 1690 Huygens discovered the phenomenon of refraction for calcite crystal (also HCP) which can be extinguished by passing it through a second calcite crystal, and this becomes the starting point of learning the fundamentals of polarisation. This result was the reference point for Isaac Newton to introduce his wave theory. However, at that time, scientists believed if light waves existed, they would be only longitudinal waves which are similar to sound waves. In 1801 Thomas Young advanced the wave theory by an incredibly straightforward experiment to illustrate the light interference called the two-point interference test. This method was missing the quantitative aspects, and that's why it did not get enough attention until 1808 when Etienne-Louis Malus, a French army officer, observed the sun's reflection from a windowpane by a Valspar crystal. Malus discovered two individual images formed by double refraction were extinguished alternatively by rotating the calcite crystal. In 1818 Augustin Jean Fresnel, was awarded the prize for experimentally proving the solution for the diffraction problem by showing a presence of a small bright point in a shadow of a circular disk and the result predicted by Fresnel theory. Later the Fresnel theory was employed to describe the propagation, diffraction, interference and polarisation of light (82–84).

2.1.1. General physics of polarised light

As discussed earlier, Huygens discovered light was not a scalar quantity, and Newton suggests light has “sides”. This vectorial behaviour of light is called Polarisation. Optical disturbances occur in 3 different oscillations which are $u_x(r,t)$, $u_y(r,t)$ and $u_z(r,t)$. This represents the necessity of having three individual wave equations to describe the propagation of the optical disturbance.

$$u_x(r, t) = u_{0x} \cos(\omega t - k \cdot r + \delta_x)$$

Eq.2. 1a

$$u_y(r, t) = u_{0y} \cos(\omega t - k \cdot r + \delta_y)$$

Eq.2. 1b

$$u_z(r, t) = u_{0z} \cos(\omega t - k \cdot r + \delta_z)$$

Eq.2. 1c

Where $u_x(r, t)$ and $u_y(r, t)$ known as transverse components and $u_z(r, t)$ is the longitudinal component. u_{0x} , u_{0y} and u_{0z} are the maximum amplitudes, and δ_x , δ_y and δ_z are arbitrary phases. and $\omega t - k \cdot r$ is the propagator = τ

As the longitudinal component doesn't exist and the light consists of two transverse components, then the optical field can be described as Fresnel's theory:

$$u_x(r, t) = u_{0x} \cos(\omega t - kz + \delta_x)$$

Eq.2. 2a

$$u_y(r, t) = u_{0y} \cos(\omega t - kz + \delta_y)$$

Eq.2. 2b

The Fresnel theory can be upgraded and explains the wave theory passes through one complete cycle at optical frequencies, which known as an “instantaneous” wave and only

take 10^{-15} sec. In this case the instantaneous optical field and the polarisation ellipse can be described as:

$$E_x(z, t) = E_{0x} \cos(\tau + \delta_x)$$

Eq.2. 3a

$$E_y(z, t) = E_{0y} \cos(\tau + \delta_y)$$

Eq.2. 3b

$E_x(z, t)$ and $E_y(z, t)$ are the resultant vectors, and the vector is described as a locus points in space. E_{0x} and E_{0y} are the maximum amplitudes, and δ_x and δ_y are the phases.

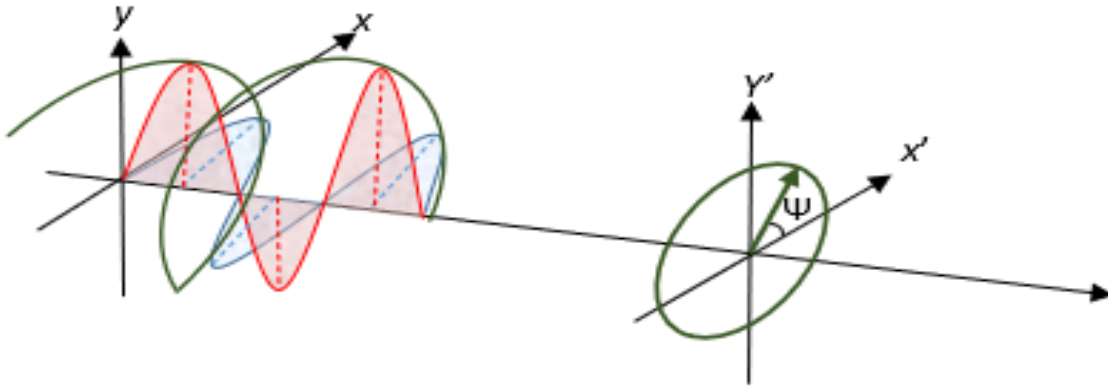


Figure 2.1 Propagation of the transverse optical field and formation of the resultant vector in the form of a rotated polarisation ellipse.

Figure 2.1 represents the formation of an ellipse when the light is polarised. A pair of plane waves which are orthogonal to each other at a point in space, where $z = 0$ can be illustrated by the equations:

$$E_x(t) = E_{0x}(t) \cos[\omega t + \delta_x(t)]$$

Eq.2. 4a

$$E_y(t) = E_{0y}(t) \cos[\omega t + \delta_y(t)]$$

Eq.2. 4b

Where $E_x(t)$ and $E_y(t)$ are the instantaneous amplitudes, w is the instantaneous angular frequency, and $\delta_x(t)$ and $\delta_y(t)$ are the instantaneous phase factors. The general format of a polarisation ellipse can only be valid at an instant time:

$$\frac{E_x^2(t)}{E_{0x}^2(t)} + \frac{E_y^2(t)}{E_{0y}^2(t)} - \frac{2E_x(t)E_y(t)}{E_{0x}(t)E_{0y}(t)} \cos\delta(t) = \sin^2\delta(t)$$

Eq.2. 5

In the case of monochromatic light source, the amplitudes and the phase are constant for all time, so the equation reduces to

$$\frac{E_x^2(t)}{E_{0x}^2} + \frac{E_y^2(t)}{E_{0y}^2} - \frac{2E_x(t)E_y(t)}{E_{0x}E_{0y}} \cos\delta = \sin^2\delta$$

Eq.2. 6

According to (2.1a) and (2.1b), as E_{0x} , E_{0y} and δ are constants, the E_x and E_y remain implicitly dependent on time. To observe equation (2.6) in terms of optical field it is necessary to have the average over the time of observation. This observation continues for a long time compared to a single oscillation, so this can be considered infinite. Although if (2.6) is considered as a single period of oscillation, the $E_x(t)$ and $E_y(t)$ can be viewed as periodicity, and the time average can be chosen so:

$$\frac{\langle E_x^2(t) \rangle}{E_{0x}^2} + \frac{\langle E_y^2(t) \rangle}{E_{0y}^2} - \frac{2\langle E_x(t)E_y(t) \rangle}{E_{0x}E_{0y}} \cos\delta = \sin^2\delta$$

Eq.2. 7a

In this case:

$$\langle E_i(t)E_j(t) \rangle = \lim_{T \rightarrow \infty} \frac{1}{T} \int_0^T E_i(t)E_j(t)dt \quad i, j = x, y$$

Eq.2. 7b

Multiplying (2.7b) by $4E_{0x}^2E_{0y}^2$,

$$4E_{0y}^2\langle 4E_x^2(t) \rangle + 4E_{0x}^2\langle E_y^2(t) \rangle - 8E_{0x}E_{0y}\langle E_x(t)E_y(t) \rangle \cos\delta = (2E_{0x}E_{0y}\sin\delta)^2$$

Eq.2.8

From 2.4a and 2.4b we can find the average values of (2.8) using for (2.7b)

$$\langle E_x^2(t) \rangle = \frac{1}{2} E_{0x}^2$$

Eq.2. 9a

$$\langle E_y^2(t) \rangle = \frac{1}{2} E_{0y}^2$$

Eq.2. 9b

$$\langle E_x(t)E_y(t) \rangle = \frac{1}{2} E_{0x}E_{0y}\cos\delta$$

Eq.2. 9c

Now can substitute (2.9) into (2.8).

$$2E_{0x}^2E_{0y}^2 + 2E_{0x}^2E_{0y}^2 - (2E_{0x}E_{0y}\sin\delta)^2 = (2E_{0x}E_{0y}\sin\delta)^2$$

Eq.2. 10

Now the quantities of each parameter can be written as:

Eq.2. 11a

$$S_0 = E_{0x}^2 + E_{0y}^2$$

Eq.2.11b

$$S_1 = E_{0x}^2 - E_{0y}^2$$

Eq.2. 11c

$$S_2 = 2E_{0x}E_{0y}\cos\delta$$

Eq.2.11d

$$S_3 = 2E_{0x}E_{0y}\sin\delta$$

The equations given by 2.11 known as stokes parameters for a plane wave and they can be expressed as

$$S_0^2 = S_1^2 + S_2^2 + S_3^2$$

Eq.2. 12

2.1.1.1 Stokes parameters

In 1852 stokes parameters were determined by Sir George Gabriel Stokes. The stokes parameters are actual quantities, and they can be observed and characterised in the form of the polarisation ellipse (85–88):

S_0 = Total intensity of the light

S_1 = The volume of linear horizontal or vertical polarised light.

S_2 = The volume of linearly polarised light $+45^\circ$ or -45° .

S_3 = Describes the volume of right or left circularly polarised light in the beam.

The light can be fully or partially polarised and in this case the state of polarisation can be described as:

$$S_0^2 \geq S_1^2 + S_2^2 + S_3^2$$

Eq.2. 13

All four stokes parameters can be described in terms of intensities, and the polarised light can be entirely characterised by having the value for all 4 parameters. The stokes parameters can be represented as a 4×1 matrix. For example, the state of linearly horizontal polarised light where $E_{0y} = 0$ can be illustrated as:

$$S_{LHP} = \begin{pmatrix} S_0 \\ S_1 \\ S_2 \\ S_3 \end{pmatrix} = \begin{pmatrix} E_{0x}^2 + E_{0y}^2 \\ E_{0x}^2 - E_{0y}^2 \\ 2E_{0x}E_{0y}\cos\delta \\ 2E_{0x}E_{0y}\sin\delta \end{pmatrix} = \begin{pmatrix} E_{0x}^2 \\ E_{0x}^2 \\ 0 \\ 0 \end{pmatrix} = \begin{pmatrix} 1 \\ 1 \\ 0 \\ 0 \end{pmatrix}$$

Eq.2. 14

2.1.2. Polarised light classification

There are several ways to produce polarised light such as, polarised by scattering, polarised by transmission, polarised by reflection, and polarised by polarisation filter, which is the most common approach to practically polarising the light. This research used polarised light microscopy to investigate the crystal orientation of the material by analysing the light before hitting the sample and reanalysing the polarised light reflected from the sample. Any changes in the polarisation state of the light would correspond to the changes in the

crystal orientation. Otherwise, the metallic material must behave like a mirror where it reflects the light with precisely the same state of polarisation.

The polarisation of light is distinguished into three different classifications, which are linear, circular, and elliptical. Linear polarisation is known as a single electromagnetic field in the direction of propagation. Circular can be considered as two perpendicular electromagnetic waves with the same amplitude travelling in the direction of propagation. In circularly polarised light conditions, the difference between the phases is 90° . However, circularly polarised light can be created with linearly polarised light by passing through a quarter-wave plate with an angle of 45° to the optic direction of the plane. Elliptically polarised light consists of two perpendicular electromagnetic fields with different amplitudes, where the waves phases differ by 90° .

2.1.2.1. Linearly polarised light

Unpolarised light is known as a type of light where the electric field fluctuates in random directions. Most available light sources in the industry, such as Halogen lighting, LED spotlights, and lasers, produce unpolarised light. Linearly polarised light is recognised as a type of light where the electric field is well defined and is confined to a single plane through propagation. The most well-known technique to create polarised light is by using a polariser filter where only lets the light pass through the filter in a single direction.

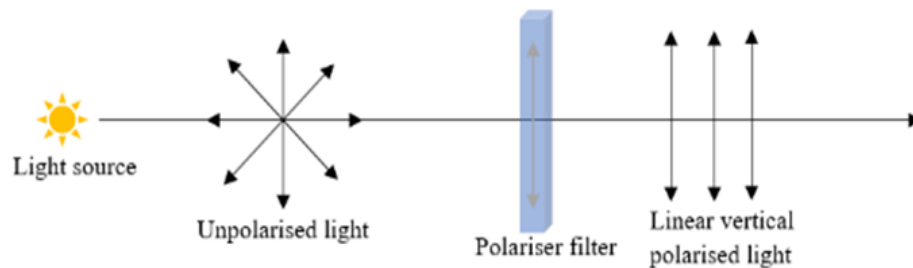


Figure 2.2 Diagram of creating linearly vertical polarised light.

As can be seen from figure 2.2, the polariser filter only lets electric field oriented in vertical direction pass through it. This is the simplest way to change an unpolarised light into a linearly polarised light. By rotating the polariser filter can control the direction of light like the example below.

Figure 2.3 shows that by turning the polariser filter 45°, the electric field also rotates 45°, the resultant light will be a +45° linearly polarised light.

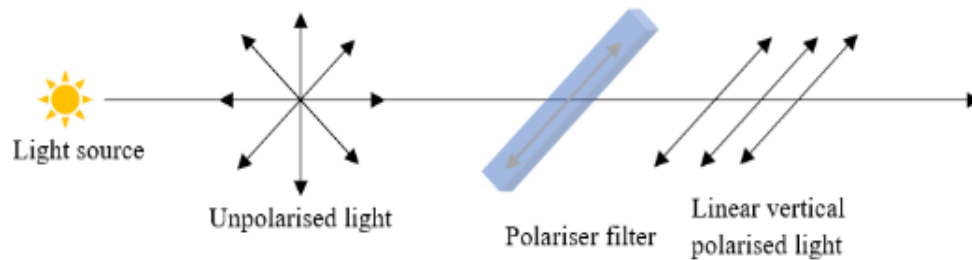


Figure 2.3 Creating linearly polarised light with certain optical axis.

As discussed earlier, the output light can be characterised in the form of stokes parameters recognised as the state of polarisation. The stokes parameter for unpolarised light known as:

$$S = \begin{pmatrix} 1 \\ 0 \\ 0 \\ 0 \end{pmatrix}$$

The interaction of light with optical elements, which can change polarisation by transmission, reflection or scattering, is illustrated with the matrix transformation known as the Mueller matrix.

$$S' = M.S$$

Eq.2. 15

Where S' is the Stokes vector of output light and M is 4×4 matrix identified as Mueller matrix, which was introduced by Mueller in the early 1940s. The Mueller matrix illustrates the polarisation altering properties of the element and defined as $m_{ij} = M_{ij}/M_{11} (i, j = 1, 2, 3, 4)$, which means:

$$M = \begin{pmatrix} m_{00} & m_{01} & m_{02} & m_{03} \\ m_{10} & m_{11} & m_{12} & m_{13} \\ m_{20} & m_{21} & m_{22} & m_{23} \\ m_{30} & m_{31} & m_{32} & m_{33} \end{pmatrix}$$

Eq.2. 16

The Stokes vector of the light interacted with several optical systems can be calculated simply by:

$$S' = M_n \dots M_2 M_1 S$$

Eq.2. 17

Each individual optical system creates their own Mueller matrix, and the combined effect of all optical systems can be calculated as $M = M_n \dots M_2 M_1$.

A polariser is an anisotropic attenuator that limits the amplitude of the electric field in two orthogonal directions of an electromagnetic wave with two transmission axes p_x and p_y .

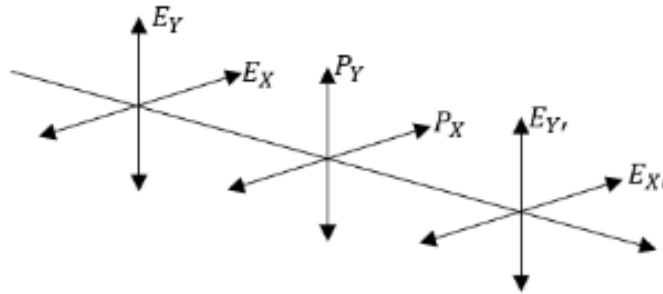


Figure 2.4 Propagation of a light beam through a polariser filter.

In this case the fields are related in a format of:

$$\text{Eq.2.18a} \quad E'_X = P_X E_X \quad 0 \leq P_X \leq 1$$

$$\text{Eq.2.18b} \quad E'_Y = P_Y E_Y \quad 0 \leq P_Y \leq 1$$

The Stokes polarisation parameters of the incident and emerging beams can be represented by

$$\text{Eq.2.19a} \quad S'_0 = E'_X E'^*_X + E'_Y E'^*_Y$$

$$\text{Eq.2.19b} \quad S'_1 = E'_X E'^*_X - E'_Y E'^*_Y$$

$$\text{Eq.2.19c} \quad S'_2 = E'_X E'^*_Y + E'_Y E'^*_X$$

$$\text{Eq.2.19d} \quad S'_3 = i(E'_X E'^*_Y - E'_Y E'^*_X)$$

Substituting (18) into (19) can form the general Mueller matrix for the polariser:

$$M_P = \frac{1}{2} \begin{pmatrix} P_x^2 + P_y^2 & P_x^2 - P_y^2 & 0 & 0 \\ P_x^2 - P_y^2 & P_x^2 + P_y^2 & 0 & 0 \\ 0 & 0 & 2P_x P_y & 0 \\ 0 & 0 & 0 & 2P_x P_y \end{pmatrix}$$

Eq.2. 20

P_x and P_y are amplitude transmission coefficients along the orthogonal transmission axis.

This means for an ideal linear vertical polariser that only transmitting light in y-direction

$P_x = 0$ so the Mueller matrix for linear vertical polariser can be calculated as:

$$M_{lvp} = \begin{pmatrix} 1 & -1 & 0 & 0 \\ -1 & 1 & 0 & 0 \\ 0 & 0 & 0 & 0 \\ 0 & 0 & 0 & 0 \end{pmatrix}$$

The Stokes vector of an output light that passes through a polariser with vertically transmitting light direction is represented below:

$$\begin{pmatrix} 1 \\ 0 \\ 1 \\ 0 \end{pmatrix} = \begin{pmatrix} 1 & -1 & 0 & 0 \\ -1 & 1 & 0 & 0 \\ 0 & 0 & 0 & 0 \\ 0 & 0 & 0 & 0 \end{pmatrix} \begin{pmatrix} 1 \\ 0 \\ 0 \\ 0 \end{pmatrix}$$

The situation will be different when we deal with a rotated ideal linear polariser, in this case the state of output light can be calculated by

$$S' = M_R(2\theta).S$$

Eq.2. 21

Where S' the stokes vector of the beam and $M_R(2\theta)$ is the Mueller matrix for rotated ideal linear polariser.

$$M_R(2\theta) = \begin{pmatrix} 1 & \cos 2\theta & \sin 2\theta & 0 \\ \cos 2\theta & \cos^2 \theta & \sin 2\theta \cos 2\theta & 0 \\ \sin 2\theta & \sin 2\theta \cos 2\theta & \sin^2 2\theta & 0 \\ 0 & 0 & 0 & 0 \end{pmatrix}$$

Eq.2. 22

This muller matrix can simply be used for any polariser filter with rotational angle of θ .

So, S polariser which is rotated 45° can be calculated as:

$$M_{45^\circ} = \begin{pmatrix} 1 & 0 & 1 & 0 \\ 0 & 0 & 0 & 0 \\ 1 & 0 & 1 & 0 \\ 0 & 0 & 0 & 0 \end{pmatrix}$$

So, by way of example, the Stokes vector of an output light which passes through a rotated polarised with a rotational angle of 45° can be calculated like the below:

$$\begin{pmatrix} 1 \\ 0 \\ 1 \\ 0 \end{pmatrix} = \begin{pmatrix} 1 & 0 & 1 & 0 \\ 0 & 0 & 0 & 0 \\ 1 & 0 & 1 & 0 \\ 0 & 0 & 0 & 0 \end{pmatrix} \begin{pmatrix} 1 \\ 0 \\ 0 \\ 0 \end{pmatrix}$$

Table 2.1 Stokes parameters of linear polariser through 180° rotation of optical














0°	15°	30°	45°	60°	75°	90°	105°	120°	135°	150°	165°	180°
												
S'_{0°	S'_{15°	S'_{30°	S'_{45°	S'_{60°	S'_{75°	S'_{90°	S'_{105°	S'_{120°	S'_{135°	S'_{150°	S'_{165°	S'_{180°
$\begin{pmatrix} 1 \\ 1 \\ 0 \\ 0 \end{pmatrix}$	$\begin{pmatrix} 1 \\ 0.86 \\ 0.5 \\ 0 \end{pmatrix}$	$\begin{pmatrix} 1 \\ 0.5 \\ 0.86 \\ 0 \end{pmatrix}$	$\begin{pmatrix} 1 \\ 0 \\ 1 \\ 0 \end{pmatrix}$	$\begin{pmatrix} 1 \\ -0.5 \\ 0.86 \\ 0 \end{pmatrix}$	$\begin{pmatrix} 1 \\ -0.86 \\ -0.5 \\ 0 \end{pmatrix}$	$\begin{pmatrix} 1 \\ -1 \\ 0 \\ 0 \end{pmatrix}$	$\begin{pmatrix} 1 \\ -0.86 \\ -0.5 \\ 0 \end{pmatrix}$	$\begin{pmatrix} 1 \\ -0.5 \\ -0.86 \\ 0 \end{pmatrix}$	$\begin{pmatrix} 1 \\ 0 \\ -1 \\ 0 \end{pmatrix}$	$\begin{pmatrix} 1 \\ 0.5 \\ -0.86 \\ 0 \end{pmatrix}$	$\begin{pmatrix} 1 \\ 0.86 \\ 0.5 \\ 0 \end{pmatrix}$	$\begin{pmatrix} 1 \\ 1 \\ 0 \\ 0 \end{pmatrix}$

Table 2.1 illustrates the Stokes vector of a light passing through the polariser from 0° to 180°. The symmetry of polarisation state through 180° rotation of polariser can be identified and the same value will be repeated from 180° to 360°(58,83–85,89,90).

2.1.2.2. Circular polarisation

Circularly polarised light includes two perpendicular electromagnetic waves with equal amplitudes with a phase difference of $\pi/2$. Two types of circular polarisation can be recognised, which are right circular and left circular polarisation. Circularly polarised microscopy is a popular technique in tissue engineering, biology, geology, and metallurgy. The phase difference can be achieved by using a quarter-wave plate made out of birefringent materials with different refractive indices for different light transmission orientations. The light beam first needs to change into a linearly polarised light and pass through a suitable wave plate (that introduces the $\pi/2$ phase shift between two waves) for the specific wavelengths to achieve a circular polariser with a high degree of accuracy(82,84,91).

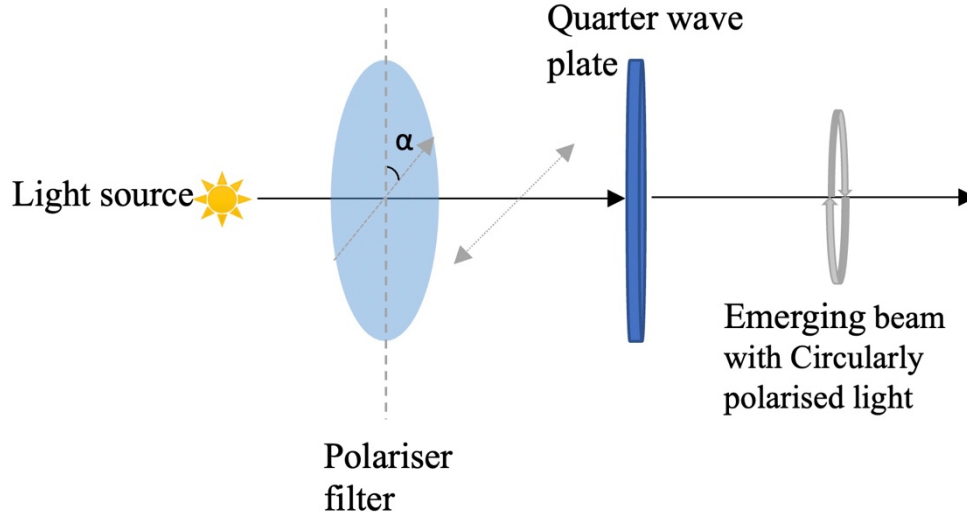


Figure 2.5 Propagation of light beam passing through a polariser filter and a quarter wave plate with an output of Circularly polarised light.

Specifically, the waveplate rotates the orthogonal field components $E_x(z, t)$ and $E_y(z, t)$ through an angle of θ . The thickness of the plate and its refractive index determine the phase shift generated. There are two main types of wave plates employed in optical microscopy, quarter-wave plates $2m\pi \pm (\pi/2)$ and half-wave plates $2m\pi + (\pi)$. Where $m = 0, 1, 2, \dots$ corresponding to the order of the wave plate. For example, the $\pi/2$ and π phase shift is recognised zero-order ($m=0$). The suitable plate thickness for a specific wavelength can be calculated by using equation 2.23 (58,92).

$$N\lambda = \pm(n_e - n_o)d \rightarrow d = \left| \frac{\lambda}{4(n_e - n_o)} \right|$$

Eq.2. 23

Where λ is the wavelength of the source light and d is the thickness of the quarter-wave plate. N is the retardation that can be expressed as a fraction of wavelength e.g. the quarter-wave plate retardation is $N=1/4$ (93). A wave plate made out of birefringent material would

have different refractive indices concerning the orientation of light. n_o represents the ordinary and n_e illustrates the extraordinary refractive indices (92).

The transmitted polarisation state of a circulatory polarised light can be calculated by:

$$S' = (S) (Mp) (Mr)$$

Eq.2. 24

Where Mp is the Mueller matrix for the polariser and Mr is the Mueller matrix for the retarders.

The Mueller matrix of the quarter plate with the fast axis of 0° , and the \emptyset is the phase delay which is 90° and can be calculated by the matrix below.

$$Mr = \begin{pmatrix} 1 & 0 & 0 & 0 \\ 0 & 1 & 0 & 0 \\ 0 & 0 & \cos\emptyset & -\sin\emptyset \\ 0 & 0 & \sin\emptyset & \cos\emptyset \end{pmatrix} = \begin{pmatrix} 1 & 0 & 0 & 0 \\ 0 & 1 & 0 & 0 \\ 0 & 0 & 0 & -1 \\ 0 & 0 & 1 & 0 \end{pmatrix}$$

Eq.2. 25

The Mueller matrix for a perfect linear polariser with transmitted axis at an angle $\Theta = 45^\circ$ is:

$$Mp = \begin{pmatrix} 1 & \cos 2\theta & \sin 2\theta & 0 \\ \cos 2\theta & \cos^2 \theta & \sin 2\theta \cos 2\theta & 0 \\ \sin 2\theta & \sin 2\theta \cos 2\theta & \sin^2 \theta & 0 \\ 0 & 0 & 0 & 0 \end{pmatrix} = \begin{pmatrix} 1 & 0 & 1 & 0 \\ 0 & 0 & 0 & 0 \\ 1 & 0 & 1 & 0 \\ 0 & 0 & 0 & 0 \end{pmatrix}$$

Eq.2. 26

For this case, the Stokes vectors of emerging beam shows the light has the state of left circular polarisation.

$$\begin{pmatrix} 1 \\ 0 \\ 0 \\ -1 \end{pmatrix} = \begin{pmatrix} 1 & 0 & 1 & 0 \\ 0 & 0 & 0 & 0 \\ 1 & 0 & 1 & 0 \\ 0 & 0 & 0 & 0 \end{pmatrix} \begin{pmatrix} 1 & 0 & 0 & 0 \\ 0 & 1 & 0 & 0 \\ 0 & 0 & 0 & -1 \\ 0 & 0 & 1 & 0 \end{pmatrix} \begin{pmatrix} 1 \\ 0 \\ 0 \\ 0 \end{pmatrix}$$

2.1.2.3. Elliptical polarisation

Any state of polarisation which lies between linear polarised and circular polarised is recognised as elliptical polarisation. Elliptically polarised light consists of two perpendicular waves with different amplitudes and a phase difference of π . Unlike circularly polarised light, elliptically polarised light can appear in many states. Experimental production of elliptically polarised light is achieved using a plane polariser followed by a quarter-wave plate. The output light consists of quanta electromagnetic field rotating with an angular velocity equal to the optical angular frequency of ω and different magnitude.

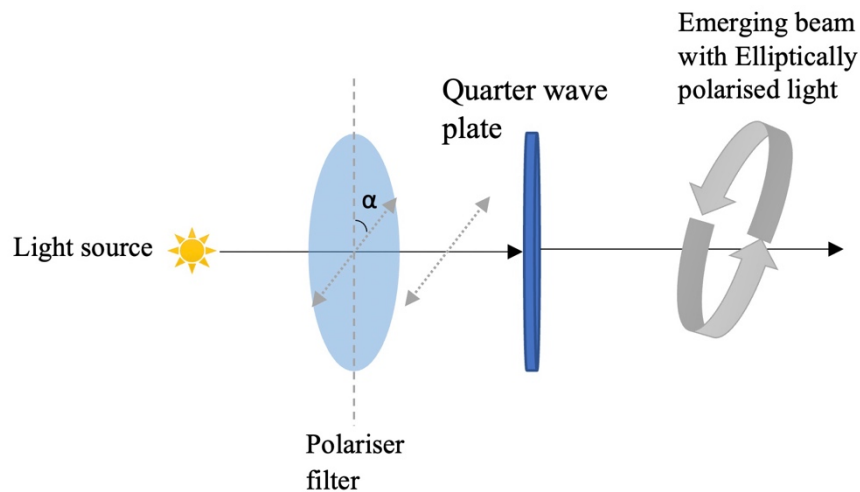


Figure 2.6 Propagation of light beam passing through a polariser filter and a quarter wave plate with an output of elliptically polarised light.

Figure 2.6 illustrates the design to produce elliptically polarised light where optical principle employed for this are precisely similar to circularly polarised light. A linear polariser changes the light to a singular direction, and a quarter-wave plate rotates the linear polariser. Although, the main difference would be in the orientation of the linear polariser or the thickness of the quarter-wave plate corresponding to the bending of an ellipse.

$$(S) = (Mp) (Mr)$$

Eq.2. 27

Let's consider if the axis of polariser is at 60° and passes through a quarter wave-plate resulting in an outcome of elliptically polarised light.

$$S' = \begin{pmatrix} 1 & \cos 2\theta & \sin 2\theta & 0 \\ \cos 2\theta & \cos^2 \theta & \sin 2\theta \cos 2\theta & 0 \\ \sin 2\theta & \sin 2\theta \cos 2\theta & \sin^2 \theta & 0 \\ 0 & 0 & 0 & 0 \end{pmatrix} \begin{pmatrix} 1 & 0 & 0 & 0 \\ 0 & 1 & 0 & 0 \\ 0 & 0 & \cos \emptyset & -\sin \emptyset \\ 0 & 0 & \sin \emptyset & \cos \emptyset \end{pmatrix}$$

Eq.2. 28

$$S' = \begin{pmatrix} 1 \\ 0 \\ 0 \\ 1 \end{pmatrix}$$

As can be seen, we have values for all Stokes parameters and most of the polarised light around us will be in the same condition. Having a correct understanding of polarised light would be necessary to find the light's Stokes vector and any changes that happened to the light on the light path.

The output ellipse can be characterised practically by using a second rotatable polariser which works as the analyser. By collecting the intensity value over 180° rotation of the analyser, we can determine if the light is linearly, circularly, or elliptically polarised.

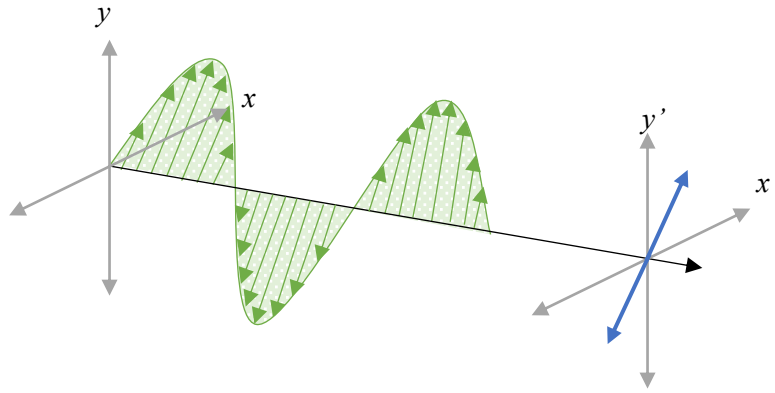


Figure 2.7 Electromagnetic wave of a linearly polarised state.

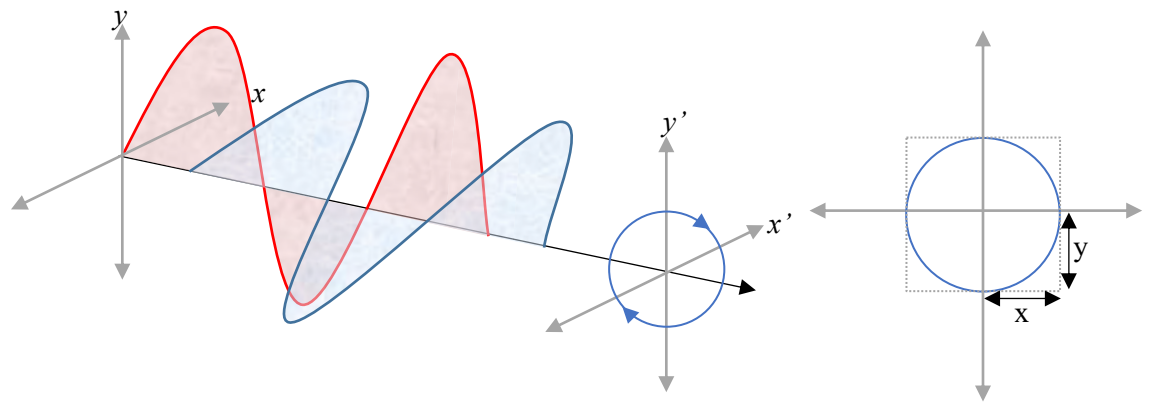


Figure 2.8 Electromagnetic wave of a circularly polarised state.

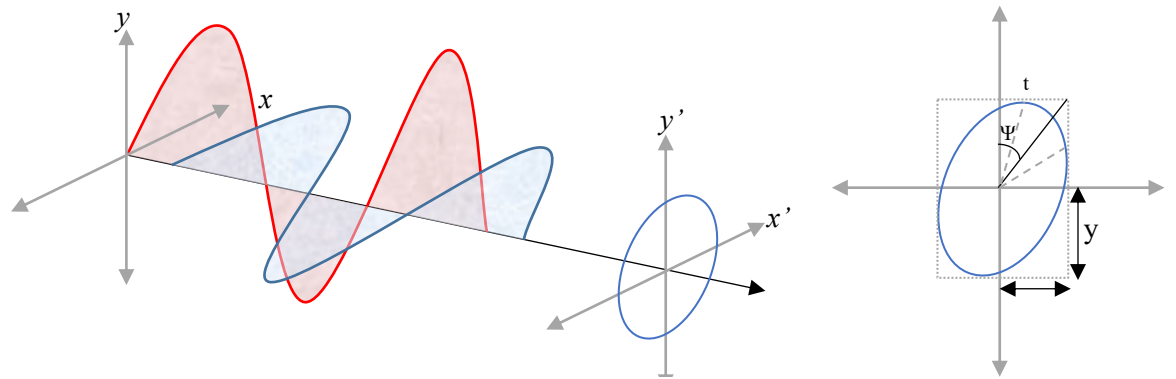


Figure 2.9 Electromagnetic wave of an elliptically polarised state.

2.1.3. Classification of circular and linear polarised light microscopy by intensity profile

Three types of polarised light conditions are demonstrated in figures (2.7, 2.8 and 2.9) and the relation of the ellipse to the intensity captured over 180° rotation of the analyser is critical to the description of the ellipse. Where in linearly polarised light, if the orientation of analyser goes to cross polarised condition (90° with respect to the polariser axis), Zero intensity will be received, and significant changes in intensity value will be captured (see figure 2.9).

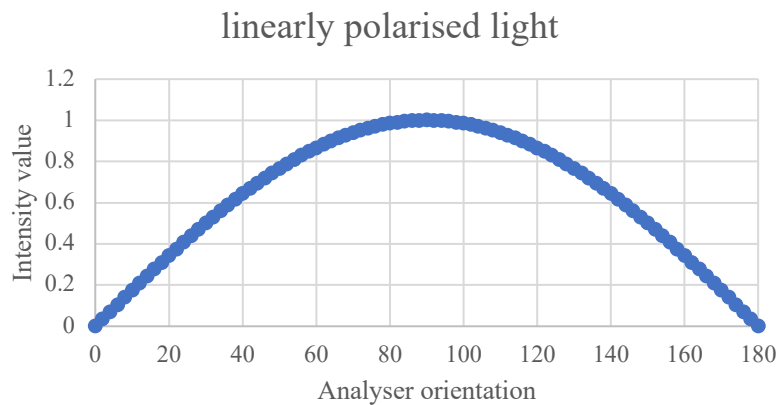


Figure 2.10 Intensity profile for linearly polarised light through a 180° rotation of analyser.

Figure 2.10 shows if the output light is a perfect circularly polarised light, the intensity value captured over 180° will be consistent and zero changes in intensity value over 180° expected.

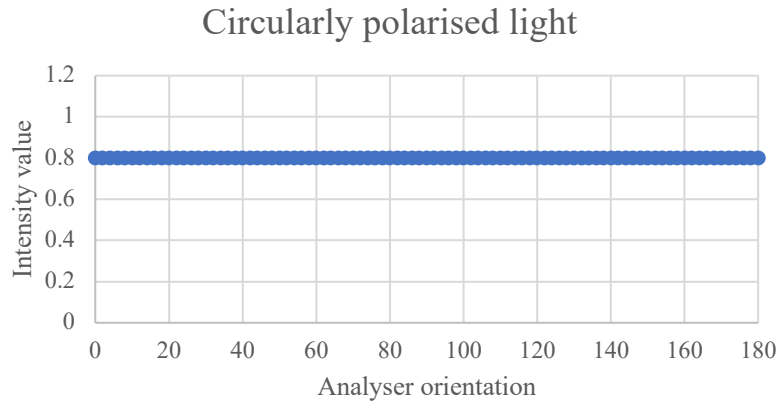


Figure 2.11 Intensity profile for circular polarised light through a 180° rotation of analyser.

For elliptical polarisation, if the ellipse is closer to the linear forms, then intensity values changes become more dominant, although practically one cannot capture a 0 intensity value as one cannot establish a cross-polarised condition. However, if the light is closer to circularly polarised, more minor changes in intensity value are anticipated.

As shown in Figures 2.10 and 2.11 the character of the light can therefore be determined through careful measurement of recorded intensity value as a function of the analyser orientation. However, one must remember the plots depict a perfect condition for each state.

In case of Polarised Light Microscopy (PLM) technique the polarisation state before reaching the specimen can be carefully measured. Similarly, the light reflected from the sample surface can be analysed. Thus, any changes in the light state (aside from those arising from perfect (e.g. mirror) reflection itself) can reasonably be expected to be due to the optical properties of reflecting surface. The widespread previous use of PLM to qualitatively observe crystals in many birefringent systems show these changes have been at least loosely correlated to the crystalline orientation of the surface. Through careful

optical measurement and correlative EBSD this study sought to quantify this relationship and unite it with the fundamental theoretical physical descriptions of the PLM technique presented above. Two crystal systems were investigated in this research, HCP (inherently anisotropic and birefringent and FCC (inherently isotropic and non-birefringent). Due to the progression of the technique during the study and the choice to address the lesser challenge of the HCP system first, the linear polarised light technique was employed to determine the crystal orientation / optical property relationship for the HCP system and circular polarised light technique was used to investigate the same in the FCC system. However, practical considerations aside, both approaches could be used for both crystal systems.

CHAPTER 3 Linearly polarised light method on HCP crystal system

The influence of texture on the mechanical performance titanium-based alloys is well documented (94–96). Many laboratory-based investigations have highlighted qualitative links between loading direction and mechanical performance in materials of high bulk texture throughout a wide spectrum of load regimes (49–51). In parallel, studies on the microtexture of titanium using crystal orientation mapping (COM) via electron backscatter diffraction (EBSD) have revealed that bulk texture in these materials is dictated by large areas of common orientation often referred to as either microtexture or macrozones (49,52,95). These two research themes have precipitated the concept of effective structural units in which microstructure, microtexture and load regime are key contributory factors(53). Consequently, the determination of microtexture (i.e. macrozone size, morphology and texture intensity) is gaining as much importance as conventional microstructural assessment in characterisation of titanium. Unfortunately, macrozone characterisation via EBSD is far more complex, costly and time consuming than its conventional counterpart (polarised light microscopy). This limits the viability of assessing macrozone characteristics as design / quality control criteria in an industrial scenario.

3.1 Introduction

Polarised light microscopy (PLM) is a long-established technique, traditionally associated with phase identification (phase contrast) in a variety of metals and minerals (97). It is ideally suited to the vast majority of commercially available titanium alloys on account of the optically anisotropic properties of the dominant low temperature HCP α phase (24,49,98). The technique exploits this property to produce definition between units of different crystal orientation whether these are twins, grains or macrozones (1,95). The resulting images can be captured through standard digital imaging equipment providing a

qualitative alternative method of producing crystal orientation maps to EBSD at vastly increased speed and reduced cost.

Previous investigations in other fields (specifically biosciences) demonstrated success in resolving differences in optical birefringence behavior in transmitted light microscopy(27,99–101). In addition, other studies have refined the principle through the implementation of laser optics (102) to produced more detailed orientation maps. Finally, some qualitative and quantitative correlations between PLM and EBSD images of superconductor material (103) have been attempted.

This research attempted to apply PLM method to resolve the crystal orientation map and overcome some critical limitation of employing EM/EBSD to produce the crystal orientation maps of polycrystalline material. The main limitations of SEM are discussed in problem initiation section. Applying PLM to this challenge can introduce an alternative option to generate practically useful crystal orientation maps. This research was conducted on Ti-6Al-4V a flexible ‘staple’ alloy for gas turbine applications.

3.2. Light path design

3.2.1. Linearly polarised light generation

In 1828 William Nicol discovered an approach to remove one of the two light beams from the optical axis, introduced initially as a polariser in the 1600s(104).

Crystals are optically divided into 4 types: perfectly symmetric crystals that would cause the light to propagate in all directions with the same speed, crystals with no symmetry in any direction, which causes the output light in all 3 directions to have different speeds. Biaxial crystal is recognised as the material where the speed of light is different in three mutually perpendicular directions, and uniaxial crystal has the same speed of light in two directions and different in the third direction. Uniaxial crystals (e.g. calcite) change the

unpolarised light into a linearly polarised light as the light in random directions directed to the crystal along the unique axis which known as the optic axis. The refraction index of the light travelling along the optic axis known as n_o and the light travelling through the plane perpendicular to the optic axis will have the index of refraction n_e . In this case the extraordinary refractive index is a function of a direction or angle which is an intermediate between n_o and n_e .

The first commercially polarised filter made by Edwin land in 1933 who later founded the Polaroid company(105). Modern filters consists of a tape of long polymer molecules stretched along its length. The stretched film is dipped in a solution of iodine to attach the iodine molecules to the polymer. The highly ordered polaroid's structure will absorb the light parallel to the polymer chains and transmit the light perpendicular to the chain. In this case, when the light travels through the tape at different speeds and the light components are moving fast (parallel to the direction of the long polymer chain), will recombine with the ones moving slowly (perpendicular to the direction of the long polymer chain) to produce waves with new properties.

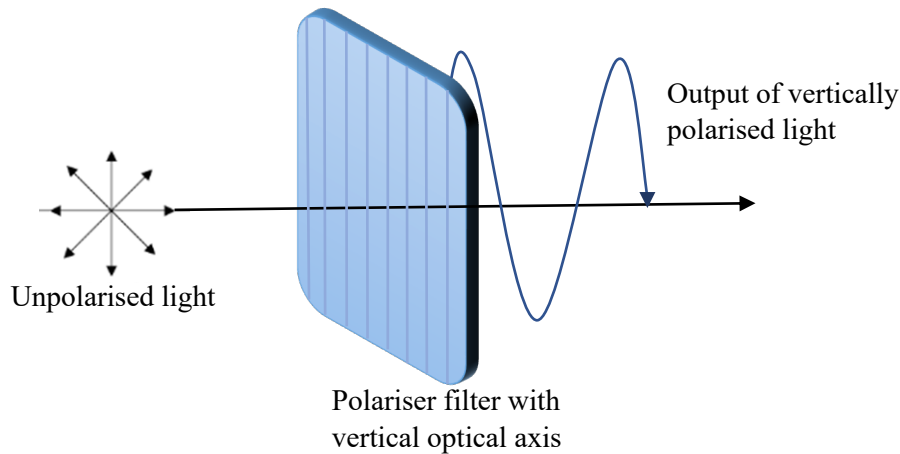


Figure 3.1. Generation of vertically linear polarised light by passing a polariser filter.

By using a polariser filter, we can instantly generate the light with a desirable optical axis which can be simply controlled by rotating the polariser orientation to a preferable optical axis angle (see figure 3.1).

3.2.2. Crossed polarised condition

Cross polarisation is a condition where the polariser and the analyser (the second polariser with the same optical parameters) have a perpendicular optical axis. In this condition, no light is expected to pass through the analyser.

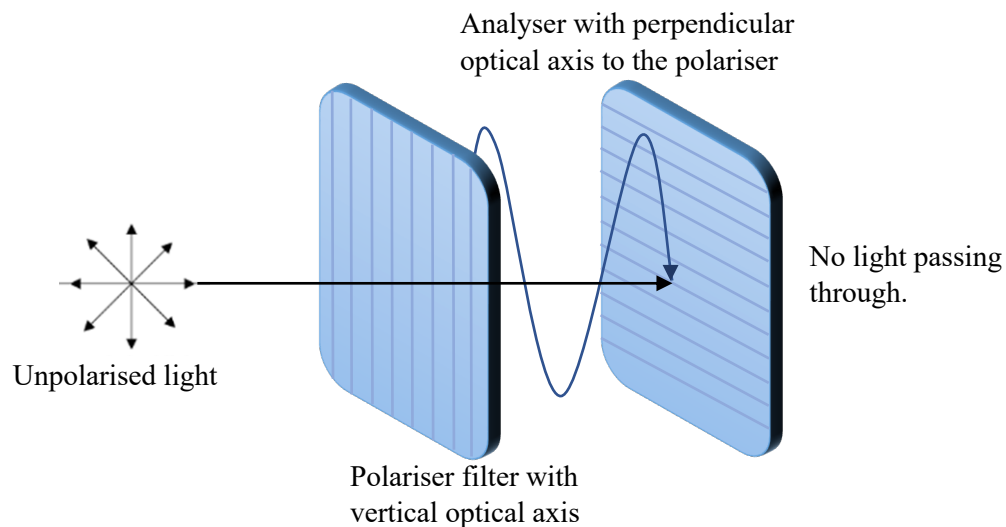


Figure 3.2. Null intensity experiment by having two polariser filter with perpendicular optical axis to each other.

Figure 3.2 illustrates the formation of cross polarised conditions where the polariser and analyser optical axis has a 90° difference in the optical axis. The first polariser rejects the p-polarised and transmits the s-polarised light, and the second polariser, which works as an analyser, will only let the p-polarised pass through the filter. In this condition, if there is no optically anisotropic material sitting between these two polariser filters, no lights expected to receive from the detector.

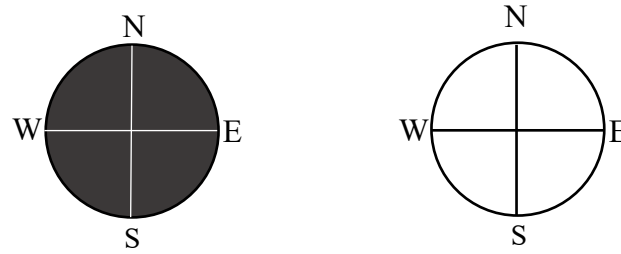


Figure 3.3 The stage view with analyser filter 90° different to the polariser filter and without. A) Analyser filter in B) Analyser filter out.

Figure 3.3 symbolises the view from the stage with the analyser in perpendicular optical axis to the polariser (cross polarised condition) and without an analyser. The intensity test of an optically isotropic sample can simply define the optical state of the polariser and the analyser. However, the situation will be different if we substitute the specimen with a polycrystalline anisotropic material. In this condition, the sample surface will reflect the light same as the diagram below where the sample reflects the light depending on the direction of the crystal (figure 3.4). This process will be discussed in details in this research.



Figure 3.4 The view of birefringent material under cross polarised condition.

3.3. Optically isotropic & anisotropic material

3.3.1. Optical isotropy

Material with isometric crystal (cubic) has a single and constant index of refraction (n) for every wavelength, which does not change with the light direction. i.e. the isotropic material speed of light remains constant although the course of irradiation changes (45).

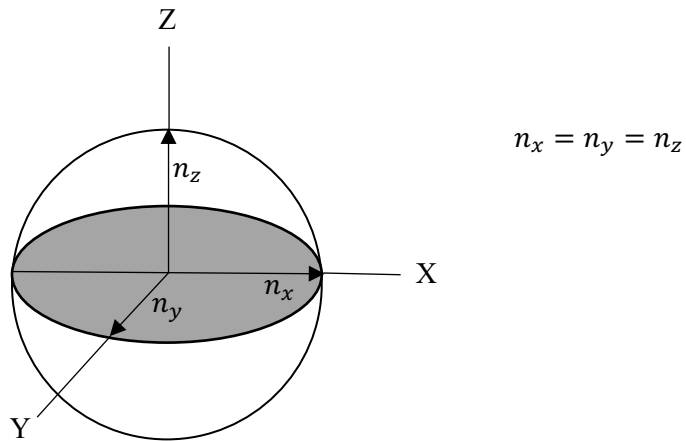


Figure 3.5 Optical indicatrix sphere of isotropic material.

In this case, the optical indicatrix (Figure 3.5 represents the index of refraction and vibration direction of light) can be expressed in a sphere and the birefringence considered to be zero.

3.3.2. Optically anisotropic

Anisotropic materials are divided into two main types, which are uniaxial and biaxial. Uniaxial recognised as a type of material with two extreme refractive indices for each wavelength (see figure 3.6). Crystalline materials with tetra and hexagonal crystal systems identified as uniaxial material. This system has two different unit cell dimensions (a and c) with a having a high degree symmetry about the c axis. In this system, the material has a single optical axis and characterised as optically uniaxial.

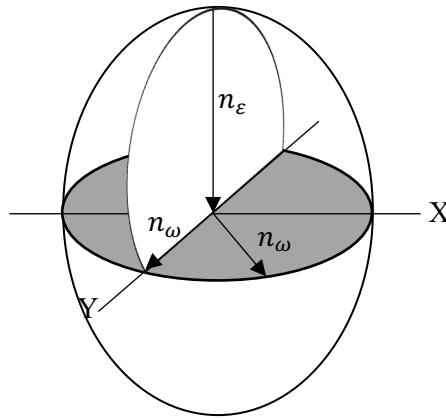


Figure 3.6 Optical indicatrix sphere of optically uniaxial material.

Figure 3.7 represents the indicatrix sphere of optically biaxial materials such as mono, ortho and triclinic crystal systems usually require three dimensions to describe the unit cell and three refractive indices with two opposite optical and one being neutral between two to define the shape of their indicatrix. The refractive index represented as n_α , n_β and n_γ where $n_\alpha < n_\beta < n_\gamma$.

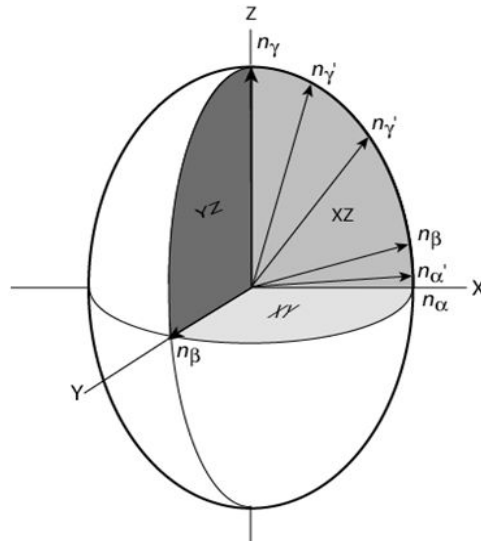


Figure 3.7 Optical indicatrix sphere of optically biaxial material.

3.4. Tensors

It is necessary to have comprehensive understanding on the EBSD technique to determine the correlation between the EBSD and PLM.

3.4.1. Linear elasticity

Linear elasticity links the strain experienced in any volume element to the forces acting on the microscopic body. The most essential constructive equations of the stress sensitivity for arbitrary anisotropic material under arbitrary load can be discussed by linear elasticity(106).

3.4.2. Anisotropic Elasticity

Many materials employ the linear elastic model to characterise them, although they are not isotropic. The mechanical properties of these materials differ in different directions; these materials considered to be anisotropic.

3.4.2.1. Hooke's Law

Based on Linear Elasticity, the most generalized linear relationship of stress and strain of a material is related by the stiffness matrix, and the relationship can be defined as:

$$\sigma_{ij} = C_{ijkl}\epsilon_{kl}$$

Eq.3. 1a

$$\epsilon_{ij} = S_{ij}\sigma_{ij}$$

Eq.3. 1b

Where σ_{ij} and ϵ_{ij} show the stress and strain components, i represents the direction of normal to the plane, and j illustrates component direction. The stiffness constant of the crystal symbolized by C_{ijkl} and S_{ij} is the compliances of the crystal. C_{ijkl} are the components of the fourth-order stiffness tensor of material properties originally consisting of 81 and 16 components for three-dimensional and two-dimensional problems. This leads to an asymmetrical 9 x 9 array of coefficients which represented as below.

$$\begin{pmatrix} \sigma_{11} \\ \sigma_{22} \\ \sigma_{33} \\ \sigma_{23} \\ \sigma_{31} \\ \sigma_{12} \\ \sigma_{32} \\ \sigma_{13} \\ \sigma_{21} \end{pmatrix} = \begin{pmatrix} C_{1111} & C_{1122} & C_{1133} & C_{1123} & C_{1131} & C_{1112} & C_{1132} & C_{1113} & C_{1121} \\ C_{2211} & C_{2222} & C_{2233} & C_{2223} & C_{2231} & C_{2212} & C_{2232} & C_{2213} & C_{2221} \\ C_{3311} & C_{3322} & C_{3333} & C_{3323} & C_{3331} & C_{3312} & C_{3332} & C_{3313} & C_{3321} \\ C_{2311} & C_{2322} & C_{2333} & C_{2323} & C_{2331} & C_{2312} & C_{2332} & C_{2313} & C_{2321} \\ C_{3111} & C_{3122} & C_{3133} & C_{3123} & C_{3131} & C_{3112} & C_{3132} & C_{3113} & C_{3121} \\ C_{1211} & C_{1222} & C_{1233} & C_{1223} & C_{1231} & C_{1212} & C_{1232} & C_{1213} & C_{1221} \\ C_{3211} & C_{3222} & C_{3233} & C_{3223} & C_{3231} & C_{3212} & C_{3232} & C_{3213} & C_{3221} \\ C_{1311} & C_{1322} & C_{1333} & C_{1323} & C_{1331} & C_{1312} & C_{1332} & C_{1313} & C_{1321} \\ C_{2111} & C_{2122} & C_{2133} & C_{2123} & C_{2131} & C_{2112} & C_{2132} & C_{2113} & C_{2121} \end{pmatrix} \begin{pmatrix} \epsilon_{11} \\ \epsilon_{22} \\ \epsilon_{33} \\ \epsilon_{23} \\ \epsilon_{31} \\ \epsilon_{12} \\ \epsilon_{32} \\ \epsilon_{13} \\ \epsilon_{21} \end{pmatrix}$$

Eq.3. 2a

$$\begin{pmatrix} \varepsilon_{11} \\ \varepsilon_{22} \\ \varepsilon_{33} \\ \varepsilon_{23} \\ \varepsilon_{31} \\ \varepsilon_{12} \\ \varepsilon_{32} \\ \varepsilon_{13} \\ \varepsilon_{21} \end{pmatrix} = \begin{pmatrix} S_{1111} & S_{1122} & S_{1133} & S_{1123} & S_{1131} & S_{1112} & S_{1132} & S_{1113} & S_{1121} \\ S_{2211} & S_{2222} & S_{2233} & S_{2223} & S_{2231} & S_{2212} & S_{2232} & S_{2213} & S_{2221} \\ S_{3311} & S_{3322} & S_{3333} & S_{3323} & S_{3331} & S_{3312} & S_{3332} & S_{3313} & S_{3321} \\ S_{2311} & S_{2322} & S_{2333} & S_{2323} & S_{2331} & S_{2312} & S_{2332} & S_{2313} & S_{2321} \\ S_{3111} & S_{3122} & S_{3133} & S_{3123} & S_{3131} & S_{3112} & S_{3132} & S_{3113} & S_{3121} \\ S_{1211} & S_{1222} & S_{1233} & S_{1223} & S_{1231} & S_{1212} & S_{1232} & S_{1213} & S_{1221} \\ S_{3211} & S_{3222} & S_{3233} & S_{3223} & S_{3231} & S_{3212} & S_{3232} & S_{3213} & S_{3221} \\ S_{1311} & S_{1322} & S_{1333} & S_{1323} & S_{1331} & S_{1312} & S_{1332} & S_{1313} & S_{1321} \\ S_{2111} & S_{2122} & S_{2133} & S_{2123} & S_{2131} & S_{2112} & S_{2132} & S_{2113} & S_{2121} \end{pmatrix} \begin{pmatrix} \sigma_{11} \\ \sigma_{22} \\ \sigma_{33} \\ \sigma_{23} \\ \sigma_{31} \\ \sigma_{12} \\ \sigma_{32} \\ \sigma_{13} \\ \sigma_{21} \end{pmatrix}$$

Eq.3. 2b

Each C_{ijkl} is achieved by considering a set of applied stress components where all components of strain vanish except for either one normal component or a pair of shear components. For example, $\sigma_{11} = C_{1111}\varepsilon_{11}$ in this case $\sigma_{ii} = C_{ii}\varepsilon_{kk}$ where $i = k$.

3.4.2.2. Effects of crystal symmetry on C and S matrices

Due to the centre symmetries of the stiffness tensor and the compliances tensor such as ($C_{12} = C_{21}$ or $S_{12} = S_{21}$) the material constants reduce to 21. Also, the material constant can be represented in a simpler format after Voigt managed to change the format of contracted matrix notation from pairs into single suffixes in 1928 e.g. 11 = 1, 22 = 2, 33 = 3, 23 or 32 = 4, 31 or 13 = 5 and 12 or 21 = 6. This further decreases due to other symmetry elements such as axes of rotation mirror planes and inversion. The most general format for an anisotropic linear elastic material. According to (107) Voigt, 1928; Nye, 1985; Hearmon, 1979 the symmetrical 6 x 6 matrix for hexagonal crystal structure can be represented as:

$$\begin{pmatrix} \sigma_1 \\ \sigma_2 \\ \sigma_3 \\ \sigma_4 \\ \sigma_5 \\ \sigma_6 \end{pmatrix} = \begin{pmatrix} C_{11} & C_{12} & C_{13} & \blacksquare & \blacksquare & \blacksquare \\ C_{12} & C_{11} & C_{13} & \blacksquare & \blacksquare & \blacksquare \\ C_{13} & C_{13} & C_{33} & \blacksquare & \blacksquare & \blacksquare \\ \blacksquare & \blacksquare & \blacksquare & C_{44} & \blacksquare & \blacksquare \\ \blacksquare & \blacksquare & \blacksquare & \blacksquare & C_{44} & \blacksquare \\ \blacksquare & \blacksquare & \blacksquare & \blacksquare & \blacksquare & C_{66} \end{pmatrix} \begin{pmatrix} \varepsilon_1 \\ \varepsilon_2 \\ \varepsilon_3 \\ \gamma_4 \\ \gamma_5 \\ \gamma_6 \end{pmatrix} = \begin{pmatrix} S_{11} & S_{12} & S_{13} & \blacksquare & \blacksquare & \blacksquare \\ S_{12} & S_{11} & S_{13} & \blacksquare & \blacksquare & \blacksquare \\ S_{13} & S_{13} & S_{33} & \blacksquare & \blacksquare & \blacksquare \\ \blacksquare & \blacksquare & \blacksquare & S_{44} & \blacksquare & \blacksquare \\ \blacksquare & \blacksquare & \blacksquare & \blacksquare & S_{44} & \blacksquare \\ \blacksquare & \blacksquare & \blacksquare & \blacksquare & \blacksquare & S_{66} \end{pmatrix} \begin{pmatrix} \sigma_1 \\ \sigma_2 \\ \sigma_3 \\ \sigma_4 \\ \sigma_5 \\ \sigma_6 \end{pmatrix}$$

Eq.3. 3

The stress and strain of an anisotropic material are affected by the rotation of the material matrix compared to the global coordinate system of the object. The effects depend on the particular materials' crystallographic characteristics; this micro-level structure dictates the material's behaviour. The rotation of the material matrix is done by implementing Euler angles that describe the orientation of a single crystal measured by electron backscatter diffraction (EBSD) or X-ray diffraction (XRD). Three orientations around orthogonal reference directions need to be calculated to represent a single crystal's orientation: the rotation about the Z-axis φ_1 , the x-axis Φ and the z-axis again φ_2 . These rotations are performed around the fixed vectors, which called Roll-Pitch-Yaw angle.

$$\text{Eq.3. 4a} \quad R_x = \begin{pmatrix} 1 & 0 & 0 \\ 0 & \cos\delta & -\sin\delta \\ 0 & \sin\delta & \cos\delta \end{pmatrix}$$

$$\text{Eq.3.4b} \quad R_y = \begin{pmatrix} \cos\delta & 0 & \sin\delta \\ 0 & 1 & 0 \\ -\sin\delta & 0 & \cos\delta \end{pmatrix}$$

$$\text{Eq.3.4c} \quad R_z = \begin{pmatrix} \cos\delta & -\sin\delta & 0 \\ \sin\delta & \cos\delta & 0 \\ 0 & 0 & 1 \end{pmatrix}$$

$$R = \begin{pmatrix} c_1c_2 - s_1s_2C & s_1c_2 + c_1s_2C & s_2S \\ -c_1s_2 - s_1c_2C & -s_1s_2 + c_1c_2C & c_2S \\ s_1S & -c_1S & C \end{pmatrix}$$

Eq.3. 5

Eq.3. 6a

$$c_1 = \cos (\varphi 1) \quad s_1 = \sin (\varphi 1)$$

Eq.3.6b

$$c_2 = \cos (\Phi) \quad s_2 = \sin (\Phi)$$

Eq.3.6c

$$C = \cos (\varphi 2) \quad S = \sin (\varphi 2)$$

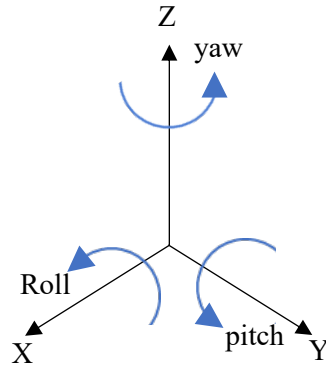


Figure 3.8 Roll-Pitch-Yaw rotation diagram around 3 axes.

	R_x	R_y	R_z
R_1	ω_{11}	ω_{12}	ω_{13}
R_2	ω_{21}	ω_{22}	ω_{23}
R_3	ω_{31}	ω_{32}	ω_{33}
	RD	TD	ND

The matrix represents the general format of the coordinate system employed by EBSD to draw the crystal orientation map. R_x , R_y and R_z known as reference vectors about to the orientation matrix (R_1 , R_2 and R_3).

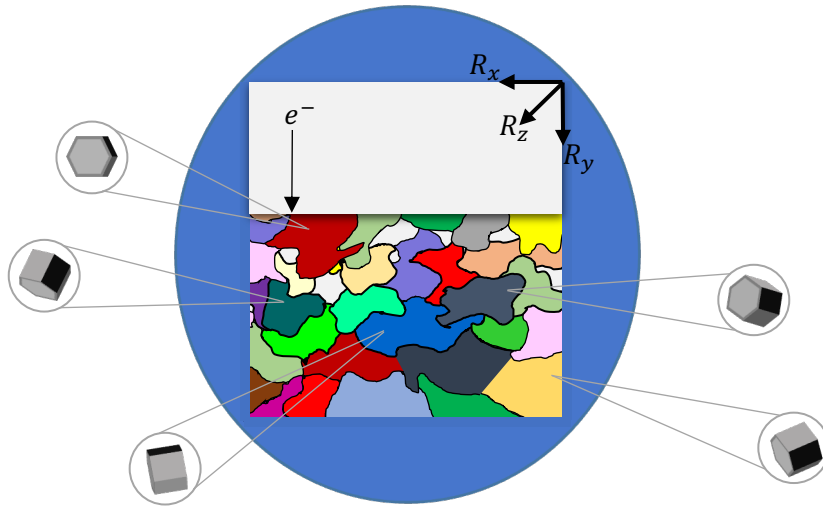


Figure 3.9 Formation of crystal orientations map by employing roll-pitch-yaw rotation around the reference point.

Figure 3.9 illustrates how the crystal orientation of each grain is corresponding to the final crystal orientation map. Later, how the value of each Euler angle would affect the intensity of three primary colours (RGB) to colour each individual grain will be explained and its limitations highlighted (43).

3.5. HCP crystal symmetry

Crystalline solid material consists of an enormous number of identical molecules arranged in a highly regular structure repeated in all directions, which offers a high order. This type of symmetry is the most fundamental character of a crystalline solid-state, called translation symmetry. This type of symmetry is observed in three dimensions in all perfect crystals.

3.5.1. Symmetry of operation

A symmetry operation is the movement of a body (molecule) such that after the movement the unit cell or the molecules appears the same as before. Two types of symmetry of operation are available, proper rotations which are a fraction of 360° about a rotation axis and improper rotations which combine a rotation and a simultaneous reflection in a plane perpendicular to the axis passing through the centre of the molecule.

Rigid body rotations can be interpreted around the fixed reference vectors. By calculating the rotation in three dimensional orientation space (R_x , R_y and R_z) (described as matrices in equation (3.4)) can eliminate the orientation of a single crystal. The simplest way to determine the orientation of a single crystal is by Euler angle. Three Euler angle are presented as below:

3.5.1.1. Euler 1 (φ_1) symmetry

- Rotation by angle φ_1 (anti clockwise) about the Z axis (Normal direction). To determine φ_1 value two parameters are critical which are ω_{32} and ω_{31} .

$$\text{If } \omega_{32} < 0 : \quad \varphi_1 = 180^\circ - \varphi' \quad \text{Where } \varphi' = \arcsin\left(\frac{\omega_{31}}{\sin\theta}\right).$$

Eq.3. 7a

$$\text{If } \omega_{32} \geq 0 \quad \varphi_1 = -(sgn(\omega_{31}) - sgn(\omega_{32})).180^\circ + \varphi'$$

Eq.3. 7b

The operation symmetry around Euler 1, which is the symmetry of Euler 1 (φ_1), will be equal to 180° in this case $0 \leq \varphi_1 \leq 180^\circ$.



Figure 3.10 Euler 1 Rotation of HCP crystal with fixed Euler 2 and Euler 3.

Figure 3.10 represents the symmetry of the HCP crystal system around Euler 1. In this case, the material will repeat the optical and mechanical behaviour after passing 180° . So, there is no need for the crystallographer to determine the orientation of Euler 1 (ϕ_1) after passing 180° , and there is no available instrument that can define the rotation value around Euler 1 after passing 180° .

3.5.1.2. Euler 2 (Φ) symmetry

- Rotation by angle Φ (anti clockwise) about the new x axis. This the simplest Euler angle to calculate from $R=\omega_{ij}$ is θ because of exceptional value range of the cosine of $0 \dots 180^\circ$.

$$\Phi = \arccos(\omega_{33})$$

Eq.3. 8

Unlike ϕ_1 and ϕ_2 no need to calculate the angle larger than 180° ; it will be excluded for any crystal system.

Figure 3.11 illustrates the operation symmetry of the HCP crystal system rotating around Euler 2 Φ is 90° too. The mechanical and optical behaviour of the HCP crystal system around Euler 2 will be identical after passing 90° .

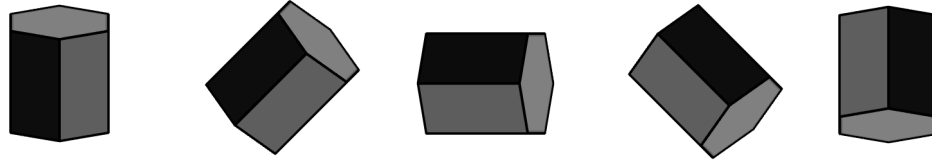


Figure 3.11 Euler 2 rotation of HCP crystal system with fixed Euler 1 and Euler 2.

3.5.1.3. Euler 3 (φ_2) symmetry

- Rotation by angle φ_2 (anti clockwise) about x axis (Transverse direction). To determine φ_1 full range of rotation from 0° to 360° needs to be considered. The Euler angle of φ depends on two other parameters which are ω_{23} and ω_{13} .

$$\text{If } \omega_{23} < 0 : \varphi_2 = -(\text{sgn}(\omega_{13}) - \text{sgn}(\omega_{32})). 180^\circ + \varphi' \quad \text{Where } \varphi' = \arcsin\left(\frac{\omega_{13}}{\sin\theta}\right)$$

Eq.3. 9a

$$2.34b) \text{ If } \omega_{23} \geq 0 \quad \varphi_2 = 180^\circ - \varphi'$$

Eq.3. 9b

The sum of φ and φ_1 will be constant if $\sin\theta = 0$

The whole Euler rotation can be explained by the matrices below.

$$R_x R_y R_z = \begin{pmatrix} 1 & 0 & 0 \\ 0 & \cos\delta & -\sin\delta \\ 0 & \sin\delta & \cos\delta \end{pmatrix} \begin{pmatrix} \cos\delta & 0 & \sin\delta \\ 0 & 1 & 0 \\ -\sin\delta & 0 & \cos\delta \end{pmatrix} \begin{pmatrix} \cos\delta & -\sin\delta & 0 \\ \sin\delta & \cos\delta & 0 \\ 0 & 0 & 1 \end{pmatrix}$$

Eq.3. 10

$$R = \begin{pmatrix} \cos\varphi_2 \cos\varphi_1 - \sin\varphi_2 \cos\Phi \sin\varphi_1 & -\cos\varphi_2 \sin\varphi_1 - \sin\varphi_2 \cos\Phi \cos\varphi_1 & \sin\varphi_2 \sin\Phi \\ \sin\varphi_2 \cos\varphi_1 + \cos\varphi_2 \cos\Phi \sin\varphi_1 & -\sin\varphi_2 \sin\varphi_1 + \cos\varphi_2 \cos\Phi \cos\varphi_1 & -\cos\varphi_2 \sin\Phi \\ \sin\Phi \sin\varphi_1 & \sin\Phi \cos\varphi_1 & \cos\Phi \end{pmatrix}$$

Eq.3. 11

3.6. Qualitative observations of the Interaction of anisotropic crystals with polarised light

The hexagonal crystal system consists of four axes where three axes have equal length and are separated with a consistent angle that lies in the same plane. The fourth axis is perpendicular to the plane of the other three axes. This type of crystal is known as optically uniaxial crystals, which demonstrate double refraction and yield two refractive indices for each colour's light. HCP crystals are well-known to transmit and reflect light depending upon the orientation of the crystalline lattice with respect to the incident polarised light angle. When light interacts with the optical axis of an anisotropic crystal it behaves in a mode similar to the interaction with isotropic crystal, which passes through with a consistent velocity. Although the light entering the non-equivalent axis will be refracted in two rays, each polarised light oscillates in the direction mutually perpendicular or at the right angle to one another and travels at different velocities. This behaviour of anisotropic crystals recognised as double refraction or birefringence.

3.7. Experimental procedure

3.7.1. Sample preparation

Ti-6Al-4V alloy of composition almost 90% titanium, 6% aluminum, 4% vanadium, 0.25% (max) iron and 0.2% (max) oxygen (take from Timet website). The alloy was beta forged at 1050°C and slow cooled to room temperature resulting in a fully transformed Widmanstätten alpha microstructure with very fine interlath beta of total volume fraction ~8%. This processing condition delivered a large colony size of approximately 60µm. This microstructure was deliberately introduced to produce large areas of common orientation

when compared to a conventional bimodal microstructure that is created when the material is deformed and annealed in the $\alpha + \beta$ phase field. Four common titanium Ti-6Al-4V microstructural forms have been assessed so as to provide a broad spectrum of both unit size and microstructural condition. These are outlined below in table 3.1.

Table 3.1 Sample designation and microstructural description of the four different microstructures under investigation.

Sample Designation	Microstructural condition
A	70 / 30 Bimodal $\alpha +$ transformed (lath) β
B	30 / 70 Bimodal $\alpha +$ transformed (lath) β
C	Equiaxed α structure
D	Fully transformed lath structure

3.7.2. EBSD data acquisition and presentation

Analytical correlative microscopy was employed on four different microstructural variants of the α / β titanium alloy Ti-6Al-4V. Light microscopy was performed on a Carl Zeiss Axio Observer in bright field and polarised condition. EBSD data was recorded on a Carl Zeiss Crossbeam 540 with Oxford Instruments EBSD and CLEM was facilitated via the Carl Zeiss Shuttle and Find system. The samples were tilted to a known, calibrated angle of 70° and a Nordilus Camera inserted to 164.1mm. Working distances of 16-18mm were employed. The EBSD system was calibrated using a cleaved silicon specimen of known crystallographic orientation (within 0.5°). Individual specimen tilts were measured prior to conducting each acquisition. The final angular accuracy of the system was within 3° . Orientation data were collected using HKL Technology Channel 5 software. The step size was varied for each map as a function of the microstructural / microtextural features of interest, these are indicated for each map in the results. In the majority of cases EBSD data is presented in the form of crystal orientation maps (COMs).

3.7.3. Optical microscopy

All optical microscopy was carried out on a Primotech Zeiss rotatable stage microscope. Unfiltered reflected light microscopy employed a white LED light source and was performed on etched metal surfaces. Polarised light microscopy was performed on as-polished un-etched surfaces using a LED light source under fixed crossed polarisation condition (Figure 3.12). Where appropriate, sample rotations were performed using a eucentric rotating stage. The sample was rotated over 360° with images captured from the sample at 1° intervals to provide an angular accuracy within that determined for the EBSD acquisition.

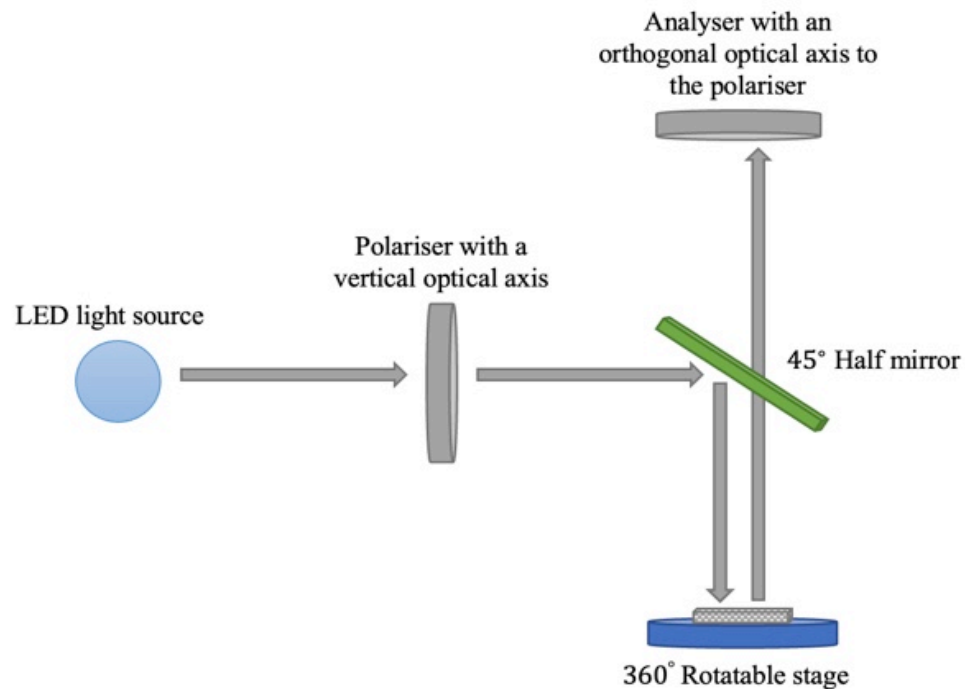


Figure 3.12 Light path designed for the PLM technique, with a rotatable stage.

All images were captured under cross polarised condition and subsequently digitally rotated back to its original position in order to provide an image stack that permitted equivalent pixels to be compared between the different images. Where intensity profiles

are presented as a function of stage rotation, these are on a grain-by-grain basis and so represent the average intensity of the pixels recorded within that grain.

3.8. Qualitative comparisons

Before describing the differences in the data presented in figures 3.13, 3.14, 3.15 and 3.16 it is important to consider the way in which these images are created. Etched microstructures are formed when a reagent chemically reacts with and dissolves material on a polished flat surface. As a result, the differences in the chemistry of individual phases within a microstructure result in different levels of attack, highlighting phase proportions. Areas of imperfectly bonded material within a single phase material, such as grain boundaries with their associated boundary free volume, are preferentially attacked with low energy stacking faults, areas of high dislocation density and finally well packed crystal structures less prone to attack in that order. Consequently, the microstructures produced depend strongly on etch concentration and time of exposure (explaining the consistent etch times employed in the investigation).

EBSD information is retrieved from the specimen surface by quantifying Kikuchi electron diffraction patterns meaning crystal orientation is calculated as a function of inter-planar spacing within the crystal lattice. This provides an unambiguous record of crystal structure. While the technique cannot acquire boundary data directly, it can define crystal boundaries through the subsequent inspection of misorientation profiles in the data set.

Finally, information recorded under polarised light results as a function of the amount of twist/rotation of the plane of polarisation. The degree to which this plane is rotated corresponds to the specific optically anisotropic properties of the crystal structure under observation. The intensity of light passing the analyser under cross poles is then determined

by the product of the birefringent beams and Malus' law of polarisation. The resultant image contrast is then defined by the orientation of a crystal's optical axis (the c-axis of the hcp unit cell for α titanium). Individual images recorded in this way provide a qualitative description of c-axis orientations but unlike EBSD cannot define the degree of rotation about that axis and hence gives an ambiguous indication of the crystallographic orientation.

The microstructural analysis of the microstructures in variants A and B (figures 3.13 and 3.14 respectively) shows why crystal orientation measurements are so important in the characterisation of titanium alloys. Variant A clearly shows some microstructural discontinuities around the area of common orientation exposed in the EBSD map. However, this may be construed at first glance as a microstructural refinement which is clearly not the case. Variant B shows no evidence of microstructural anomalies in the etched microstructure, but EBSD again confirms the presence of a larger area of common orientation composed of both primary and secondary microstructural forms. Importantly, the polarised light images in both cases very accurately describe the crystallographic unit sizes. Etched microstructures in variants C and D (figure 3.15 and 3.16 respectively) reveal very similar unit sizes in all three analyses. This shows that conventional etched microstructures can approximate unit size in the absence of microtextured regions. However, it is worth noting that changes in lath orientation in variant D often do not correspond to differences in crystallographic orientation as evidenced by the corresponding EBSD data.

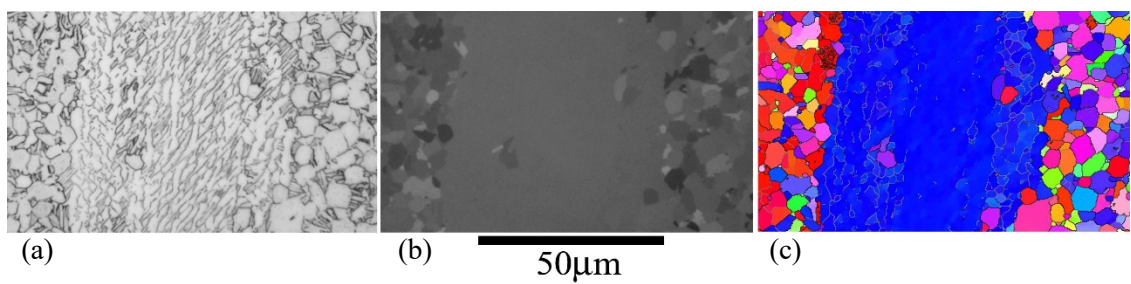


Figure 3.13 The microstructure of variant A viewed by bright field illumination in the etched condition (a) and polarised light (b) and EBSD (c) in the as polished condition.

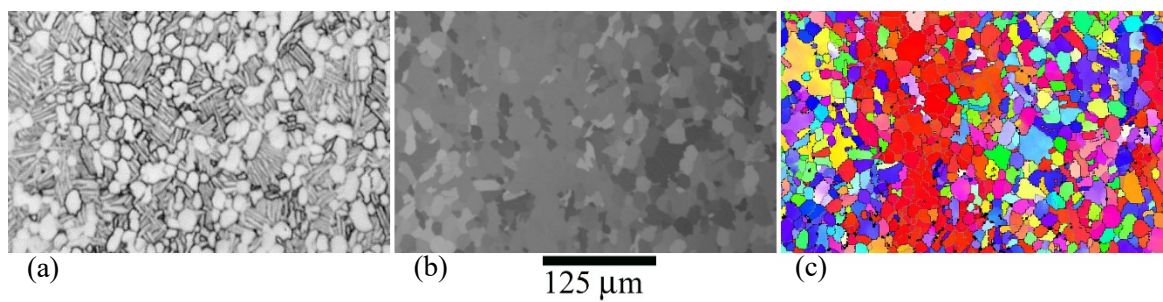


Figure 3.14 The microstructure of variant B viewed by bright field illumination in the etched condition (a) and polarised light (b) and EBSD (c) in the as polished condition.

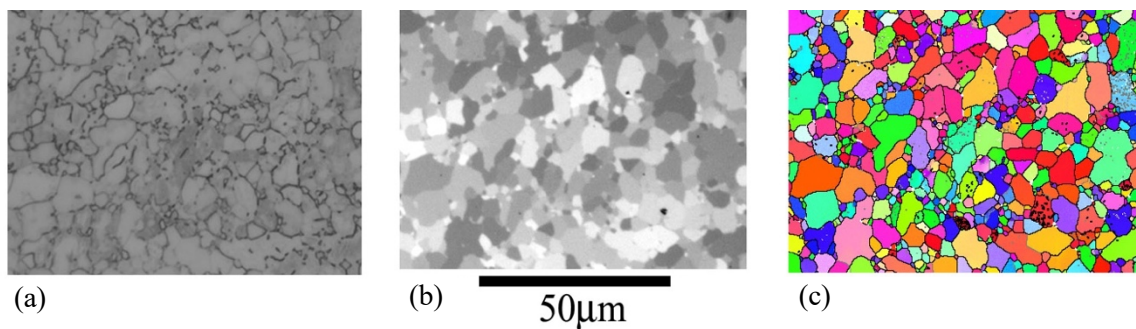


Figure 3.15 The microstructure of variant C viewed by bright field illumination in the etched condition (a) and polarised light (b) and EBSD (c) in the as polished condition.

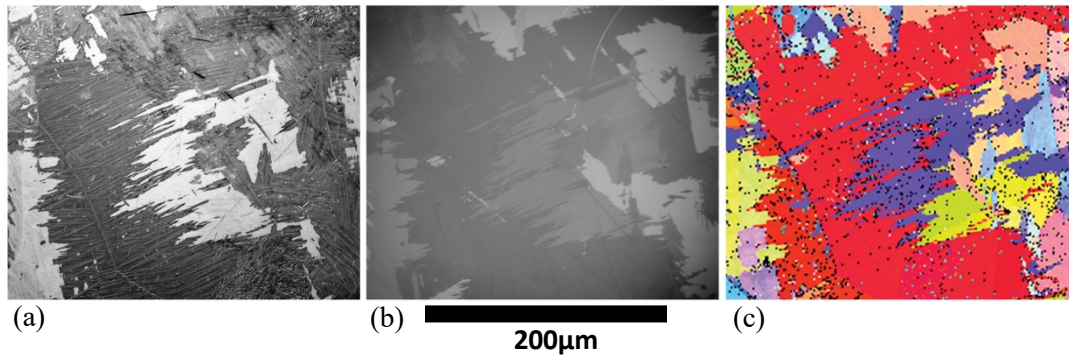


Figure 3.16 The microstructure of variant D viewed by bright field illumination in the etched condition (a) and polarised light (b) and EBSD (c) in the as polished condition.

3.8.1. Quantifying microstructure

Quantification of etched microstructures must be supported by secondary analysis as no quantitative material information can be directly gleaned by the technique. In the case of the majority of titanium engineering alloy microstructures (bi-modal) conventional grain size measurement techniques like the linear intercept method are not applicable. Post image processing can accurately distinguish between primary and secondary microstructural forms giving accurate indications of primary α grain size, an important microstructural parameter. However, when considering crystallographic units of a size in excess of this parameter etched microstructures fall short.

As EBSD is a truly quantitative acquisition technique, very accurate information can be gained on grain size distributions based on their fundamental defining character – crystallography. This in turn provides data on which quantitative assessments of unit size can be performed. Though not considered in detail in this chapter, it also permits a wide range of quantitative crystallographic analyses such as statistical analysis of boundary character (108). Nevertheless, EBSD does have limitations. These include technical issues such as the dependency of grain or unit size calculations on step size(109), image distortion / calibration (110) and absence of standard crystal symmetry in data processing(111). This

is evidenced by the comparisons between etched microstructures and EBSD images presented in figures 3.15 and 3.16. However, combined backscattered imaging and EBSD has previously been shown to be adequate for separating microtextures of primary and secondary microstructural forms(52).

Analysis of single images acquired under polarised light may be analysed through digital image processing in a manner similar to that of etched micrographs, but like EBSD it struggles to resolve the differences between units of low misorientation. As such they appear to provide an accurate approximation of unit size alone, without describing the crystallographic orientation of these areas. Clearly, proportions of commonly orientated material are well described by polarised light microscopy for all variants. As can be seen from figure 3.13, figure 3.14 and figure 3.15 variants A and B where microtextured areas are well defined crystallographically, but hidden in the microstructure. These results clearly demonstrate the advantages of polarised light microscopy as a tool for the quantification of microtextured regions in titanium alloy microstructures irrespective of microstructural form.

3.8.2. Quantitative comparison

Given the potential for unit size quantification via polarised light, and the previous documented success in quantifying optical birefringence, it seems reasonable to conclude that similar operations would be possible under reflected light. Polarised light images were recorded at various sample rotations applied using a eucentric rotating stage, using the microstructure presented in figure 3.16 as an arbitrary example. Figure 3.17 shows the symmetry observed in the appearance of images recorded at 0,90,180 and 270 degrees of rotation. Microstructural features appear similar at $0^\circ / 180^\circ$ and $90^\circ / 270^\circ$, i.e. there is a 180° symmetry in the retardation behaviour. This observation correlates well with the

crystallographic symmetry of the c-axis in the HCP α phase. Moreover, as the stage was rotated the intensity associated with individual units was found to vary sinusoidally with rotation with a phase of approximately 180° as demonstrated by the example in figure 3.17.

3.9. Euler angle correlation to intensity plot

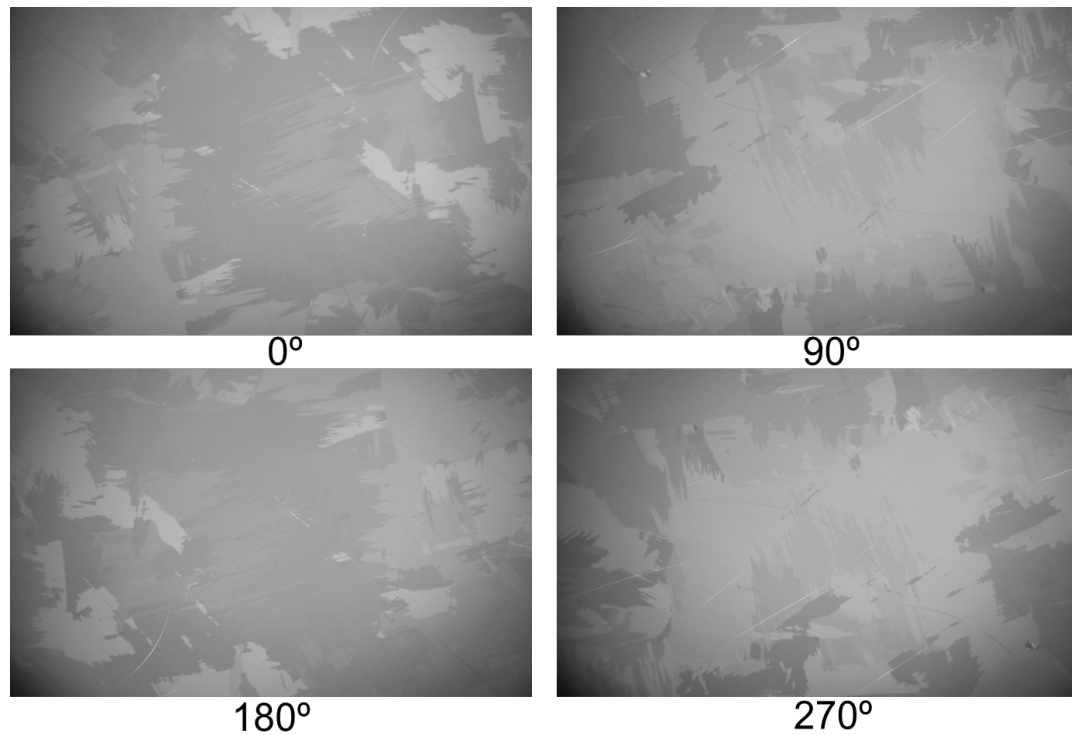


Figure 3.17 Qualitative observations of symmetry in the contrast of images recorded under circular polarised light microscopy.

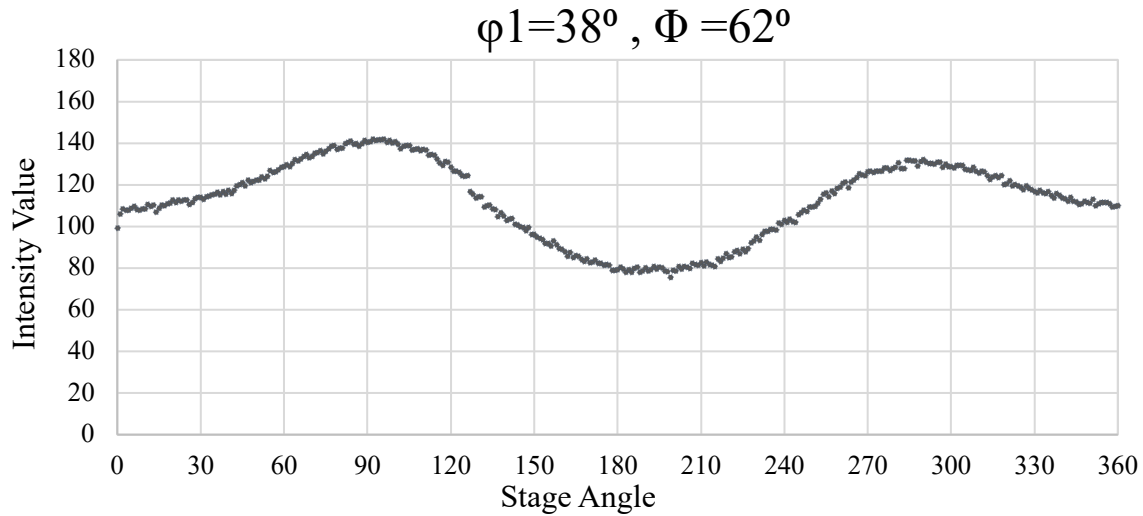


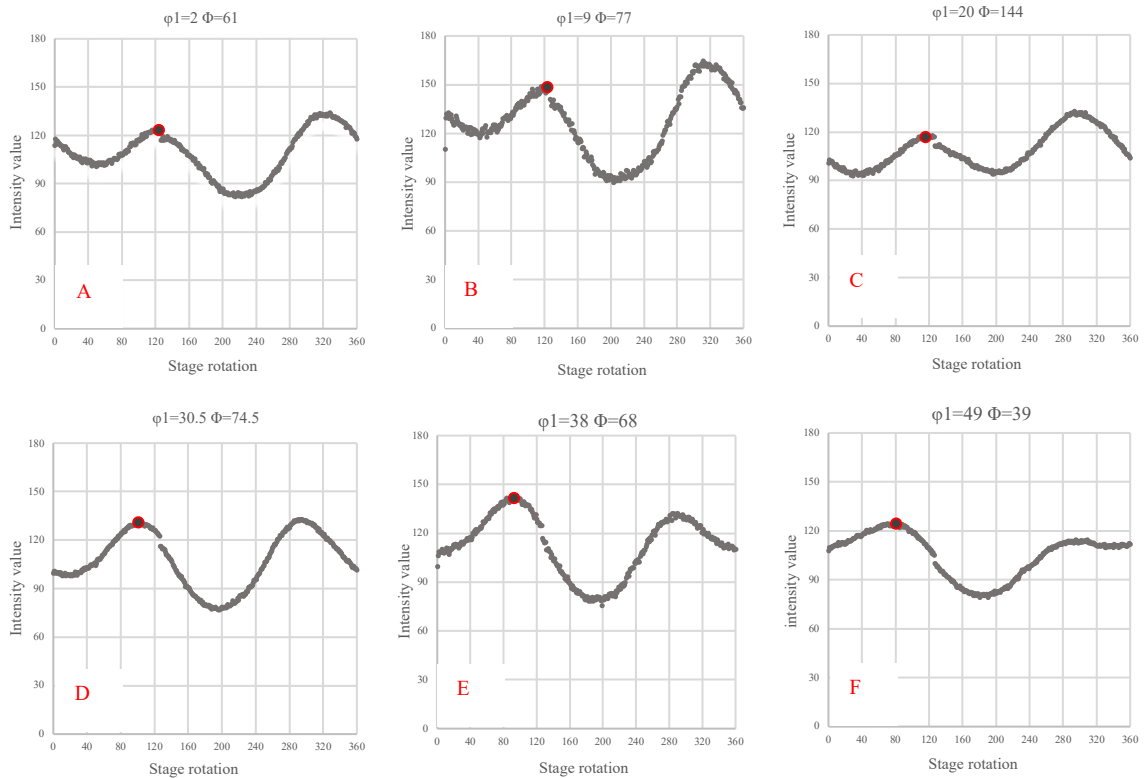
Figure 3.18 Intensity profile of an identical grain($\phi_1=38^\circ$, $\Phi =62^\circ$) through 180° stage rotation.

Figure 3.18 represents the intensity profile with stage rotation of a single grain within the dataset of orientation $\phi_1=38^\circ$, $\Phi=62^\circ$ (determined by correlative EBSD). Two critical features of the profile need to be considered ,one is the stage rotation of maximum intensity and the other one is the value of the maximum intensity which is highlighted in each plot. The value of Euler 3 (ϕ_2) is irrelevant to the intensity change for the reasons described above. This means cross polarised light microscopy technique is not capable of distinguishing the value of ϕ_2 . However the rotation of ϕ_2 not previously been shown to as as dramatic an effect on mechanical properties of material as the other two angles given the many $\langle a \rangle$ type prismatic slip planes that are available when rotating about the c axis of the HCP unit cell.

Having established similar symetries between the intensity profile and the unit cell, the development of well evidenced quantitative correlations of ϕ_1 and Φ with the intensity profileis explored in the following sections.

3.9.1. Euler 1 correlation

Obtaining the correlation between Euler angle and intensity profile is fundamental to proving the Polarised Light Microscopy (PLM) method quantitatively. Firstly this research attempt to find the correlation between Euler one orientation and the intensity plot. Around 100 individual grains have been analysed to prove the consistency of the correlation. It was identified in the preliminary studies that the position of the maximum intensity appeared to be related to ϕ_1 . The intensity profile was captured for each of the 100 individual grains through 360° rotation of stage rotation under cross polarised condition with examples presented in figure 3.17.



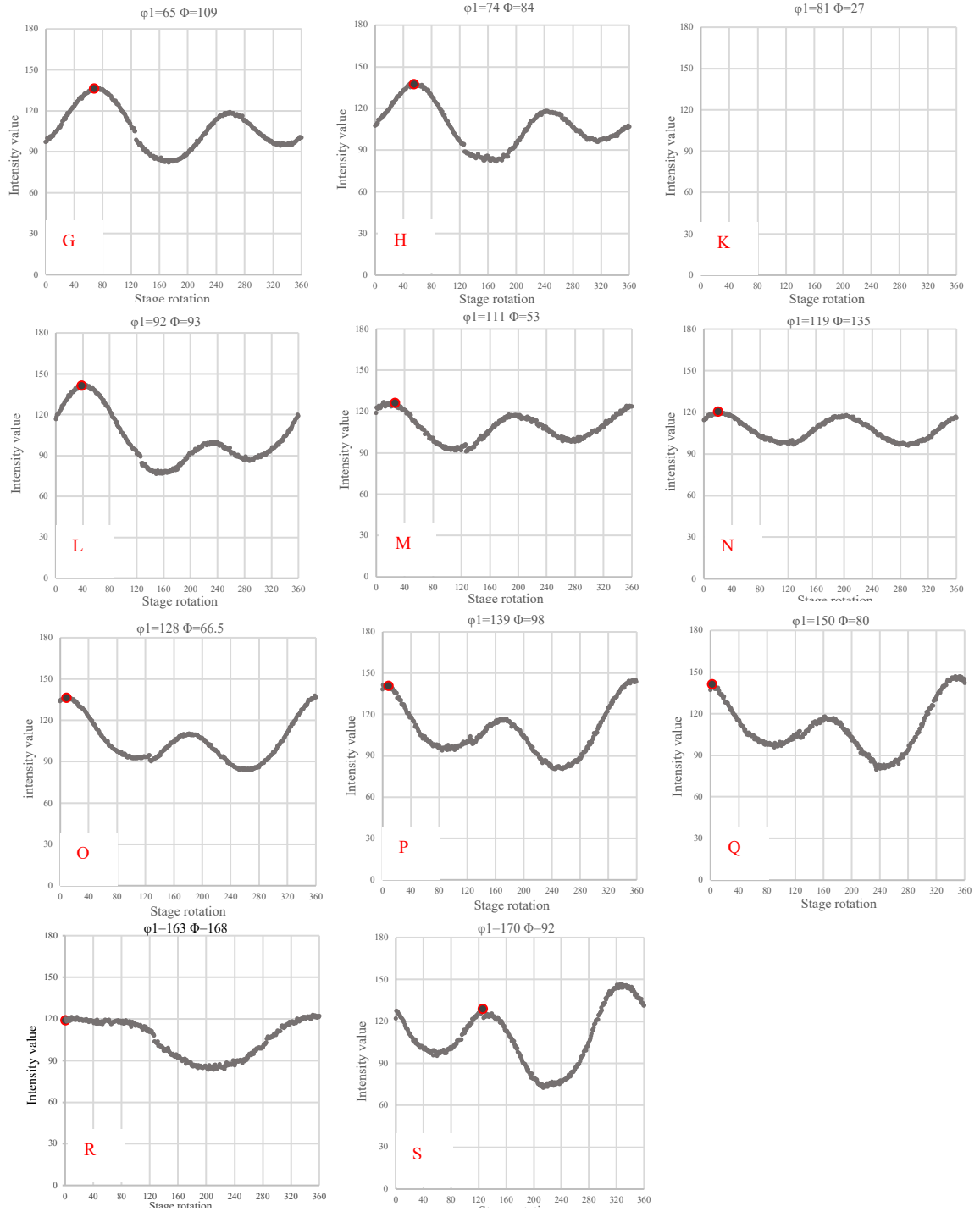


Figure 3.19 Intensity profile captured through 360° rotation of analyser for different grains with certain crystal orientations. The value for Euler1 increasing gradually to highlight the correlation between Euler1 and intensity plots. The red dots highlighted the position of maximum intensity.

Figure 3.19 is arranged so that there is roughly 10° of ϕ_1 shift between each plot. Over these plots the position of maximum intensity shifts proportionally to the ϕ_1 angle and as it increases the position of maximum intensity reaches closer to $0^\circ/360^\circ$.

As can be seen from the plots in Figure 3.19 some artefact can be seen such as changes in absolute intensity through the cycle and curve disjointed at a stage position around 120° . The reason to have these errors discussed in details in section 3.11.

To generate a plot of maximum intensity versus the orientation of ϕ_1 for the wider dataset. We must consider the 180° unit cell symmetry of the c axis with respect to ϕ_1 . As such the final plot shows maximum intensity recorded through 180° of stage rotation. This data agrees with the crystal symmetry of euler angles for hexagonal unit cell which previously reported by Nolze (133).

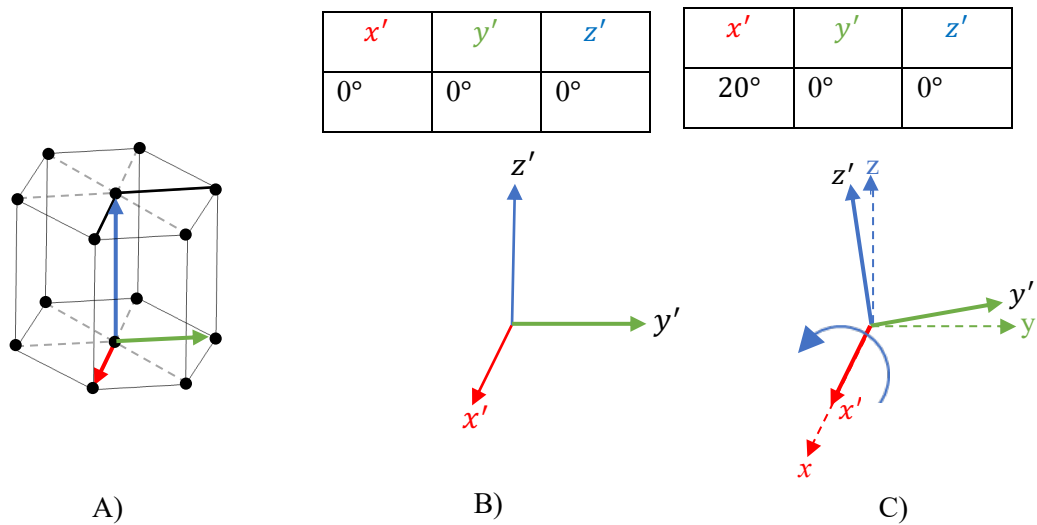


Figure 3.20 The Hexagonal Euler rotation representation for Euler 1 with fixed rotation for Euler2 and Euler3. A) Hexagonal unit cell with Euler angle reference vector. B) Euler angle set to 0° C) Roll Rotation representation with zero.

Figure 3.20 represents the rotation of Euler 1 with respect to the fixed frame for a given Euler angles. The output rotation matrix employed to demonstrate the orientation of a hexagonal unit cell in space equation 3.12.

$$R = \begin{pmatrix} \cos\phi_2 \cos\phi_1 - \sin\phi_2 \cos\Phi \sin\phi_1 & -\cos\phi_2 \sin\phi_1 - \sin\phi_2 \cos\Phi \cos\phi_1 & \sin\phi_2 \sin\Phi \\ \sin\phi_2 \cos\phi_1 + \cos\phi_2 \cos\Phi \sin\phi_1 & -\sin\phi_2 \sin\phi_1 + \cos\phi_2 \cos\Phi \cos\phi_1 & -\cos\phi_2 \sin\Phi \\ \sin\Phi \sin\phi_1 & \sin\Phi \cos\phi_1 & \cos\Phi \end{pmatrix}$$

Eq.3. 12

$$R = \begin{pmatrix} 1 & 0 & 0 \\ 0 & 0.94 & -0.342 \\ 0 & 0.342 & 0.94 \end{pmatrix}$$

In order to illustrate how ϕ_1 changes correspond to the change of the orientation of a hexagonal unit cell the position of the Φ and ϕ_2 are fixed to 0° . As previously stated the orientation of a unit cell can be expressed in space by representing with 3x3 rotation matrix. Lets consider the rotation of $\phi_1=90^\circ$, $\Phi=0^\circ$ and $\phi_2=0^\circ$ where we can simply calculate the final orientation of the unit cell by equation 3.13:

$$R = \begin{pmatrix} 0 & -1 & 0 \\ 0 & 0 & -1 \\ 1 & 0 & 0 \end{pmatrix}$$

Eq.3. 13

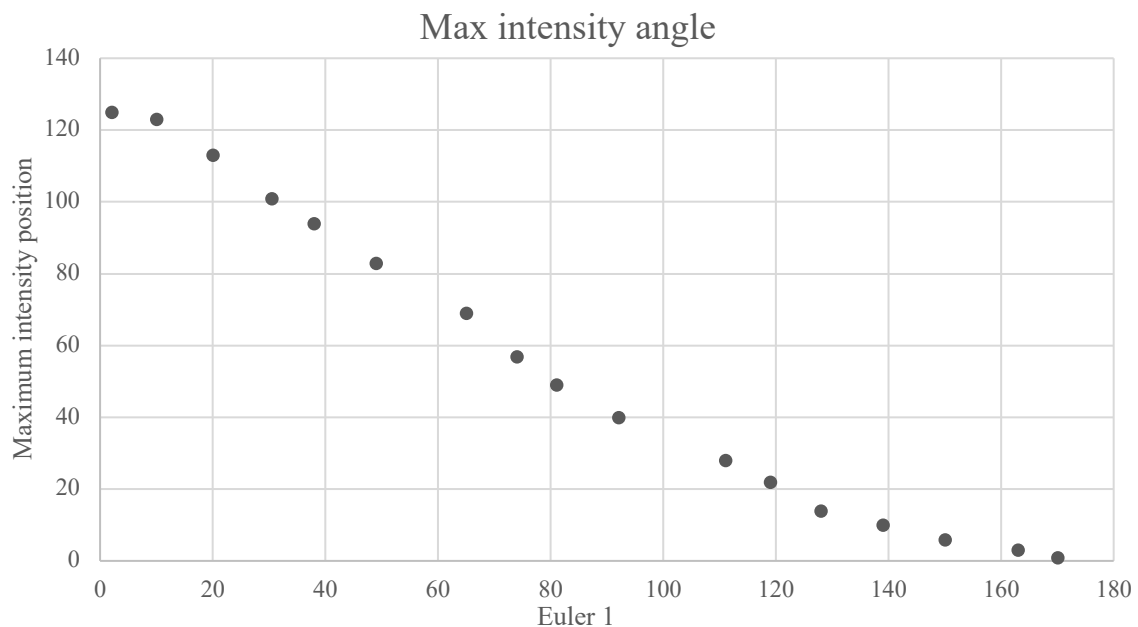
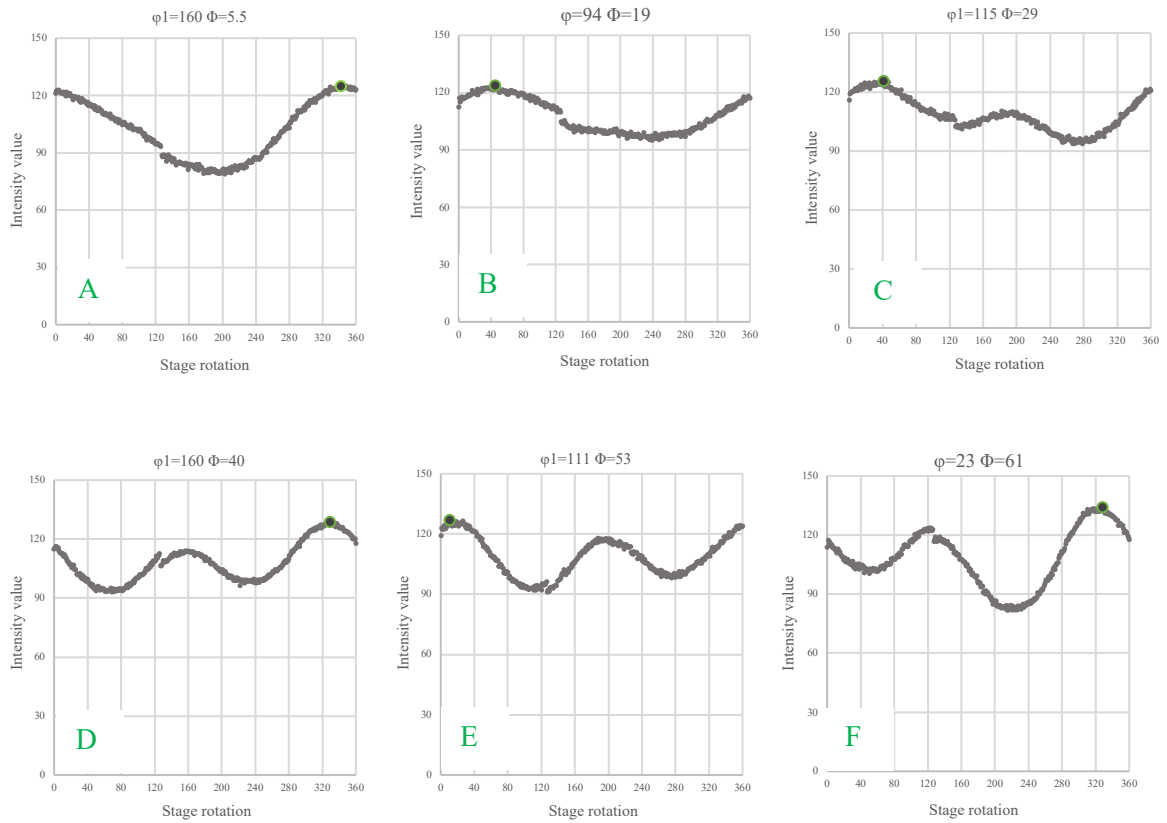


Figure 3.21 Euler 1 correlation between the position of maximum intensity through 180° of stage rotation.

Figure 3.21 shows how the rotation of Euler 1 under cross polarised condition would correspond to the position of maximum intensity. Figure 3.21 is a critical data set to produce the final crystal orientation map. This will be discussed in details later in this reaserch.

3.9.2. Euler 2 correlation

The same approach was taken to find the connection between Euler 2 (Φ) and the intensity profile. The intensity profile was collected from different grains with a well distributed range of orientation of Φ . The preliminary studies indicated that the maximum intensity (of that recorded across all the stage angles) is the key parameter to inform the correlation. As can be noticed from the dataset presented in figure 3.24 as the value for Φ approaches 90° higher intensity reflections are recorded from the grain. This observation is in agreement with the symmetry of hexagonal unit cell about Y axis which is at 90° .



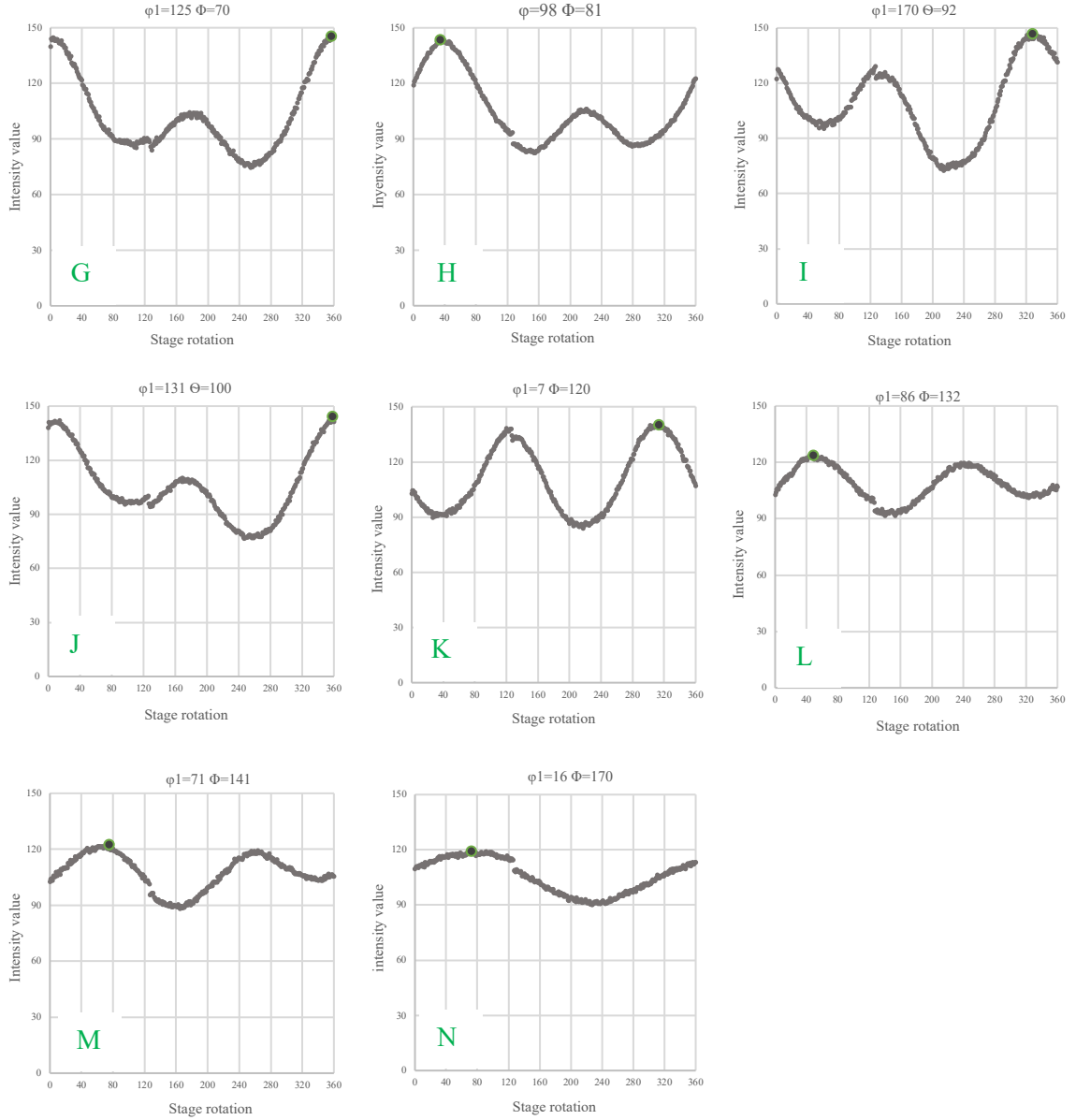


Figure 3.22 The impact of second Euler rotation to the intensity profile for each specific grain through 360° rotation of stage under cross polarised conditions.

The intensity plots in figure 3.22 show the intensity value for each specific crystal through the 360° rotation of the stage. Given that the value of Φ is critical to this correlation, grains with a wide range of Φ angles are selected here and presented in ascending order in intervals of $\sim 10^\circ$. It can be noticed from the plots that as the value of Φ becomes closer to 90° , and higher maximum intensities are recorded from the grain and the value for maximum intensity decreases as the Φ value increases from 90° to 180° . The correlation is summarised for all orientations in figure 3.24.

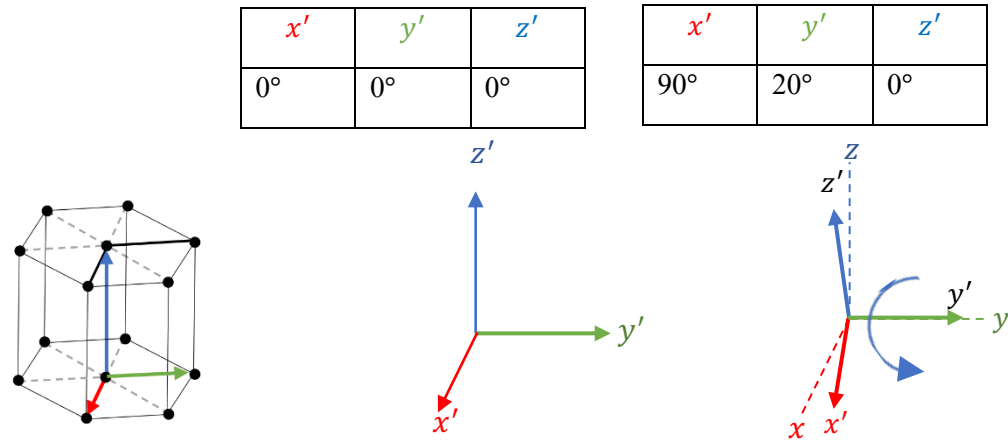


Figure 3.23 The Hexagonal Euler rotation representation for Euler 2 with fixed rotation for Euler1 and Euler3. A) Hexagonal unit cell with Euler angle reference vector. B) Euler angle set to 0° C) Pitch rotation representation with zero.

In order to illustrate the rotation of Φ and how this corresponds to the rotation of the hexagonal unit cell, Euler 1 is set to 90° , Euler 3 is set to 0° , and Euler 2 is set to the angle of interest (see figure 3.23). This simplifies the understanding of the rotation of hexagonal unit cells in space.

$$\text{Eq.2.37} \quad R_X(90^\circ)R_Y(20^\circ)R_Z(0^\circ) = \begin{pmatrix} 0.94 & 0 & 0.342 \\ 0.342 & 0 & -0.94 \\ 0 & 1 & 0 \end{pmatrix}$$

Figure 2.24 represents the rotation of Euler 2 with respect to the fixed frame for a given Euler angle. The output rotation matrix employed to demonstrate the orientation of a hexagonal unit cell in space is shown in equation 2.39.

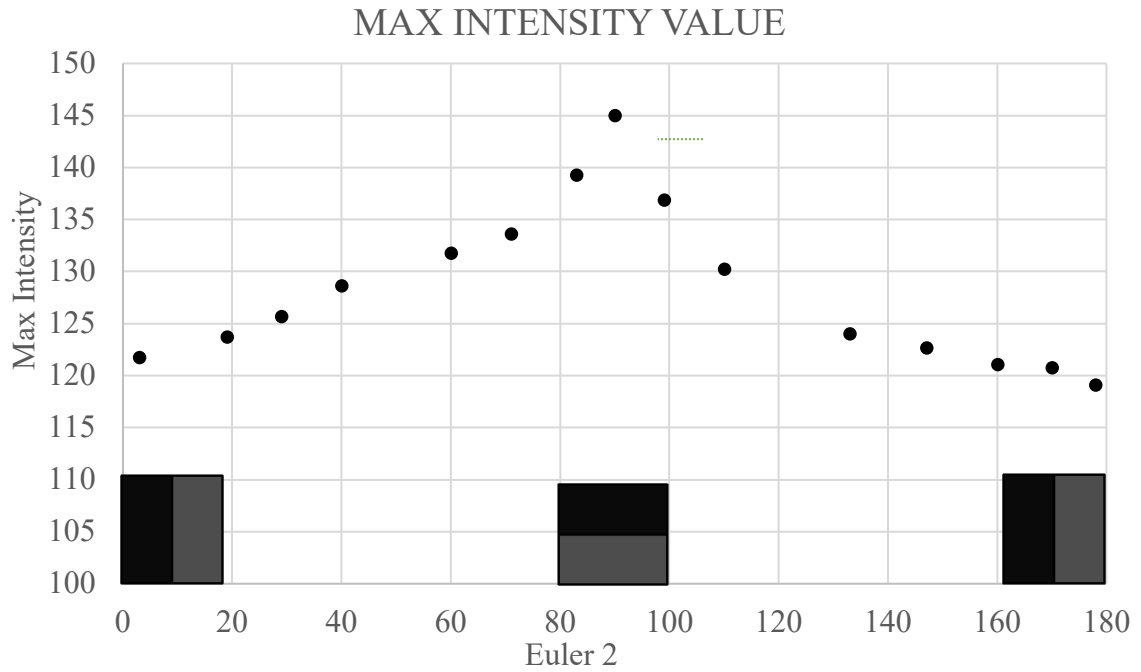


Figure 3.24 Euler 2 correlation between the maximum intensity value captured through 180° rotation of analyser and the rotation of Euler 2.

The final plot (3.24) clearly highlights the affiliation between Φ and the intensity plot. This plot agrees with the crystal symmetry of the hexagonal unit cell described in figure 3.23.

3.9.3. Euler 3 correlation

The preliminary study indicated that it was impossible to demonstrate the crystal's rotation around Euler 3 (ϕ_2) (cf the rotation about the c-axis for this system) from the raw data. This observation was confirmed when analysing the intensity plots in detail as no correlation was determined between the intensity captured and the orientation of ϕ_2 . Also, it was well discussed in many papers how the orientation of ϕ_2 has less effect on the main characters of the HCP crystal system.

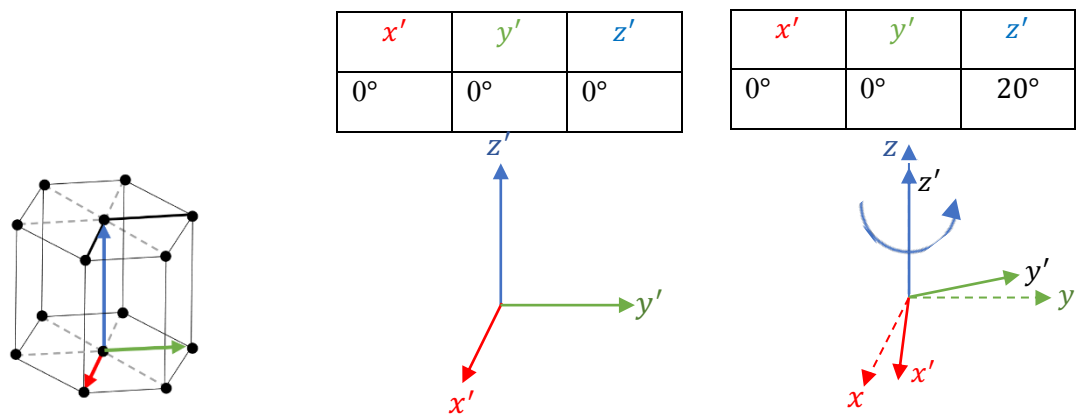


Figure 3.25 The hexagonal Euler rotation representation for Euler 3 with fixed rotation for Euler1 and Euler2.

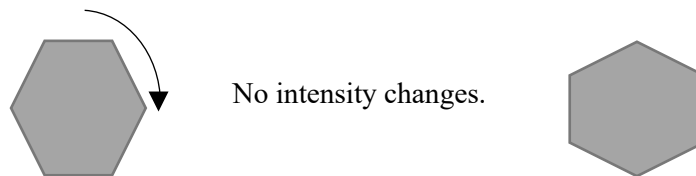


Figure 3.26 intensity change expected through the rotation around the c-axis.

By fixing the rotation of ϕ_1 and Φ to 0° and rotating the crystal around ϕ_2 , we clearly represent how ϕ_2 can change the rotation of a unit cell in space. As can be seen from the diagram by rotating the unit cell around the c-axis, no effect on the intensity plot can be

noticed. In this case, the rotation of ϕ_2 is irrelevant has no impact on the intensity plot. However, the value of Euler 3 can be estimated by an interlocking technique where there is no space for the crystal to move as crystals grew into one another. Having access to the value of Euler 1 and Euler 2 is essential to run the technique.

3.10. Forming the crystal orientation map

As such, by applying a single complete rotation of the specimen under cross-polarised conditions it should then be possible to resolve the c-axis orientation at each point on the image through a combination of maximum intensity angle and the maximum intensity value. These phenomenological and theoretical observations were applied practically through the use of digital image capture, in which three hundred sixty images were recorded at increments of 1° of sample rotation. A bespoke post processing software was developed which analysed each image individually to first normalise image rotation and subsequently record intensities at each site / pixel in the microstructure. The fluctuation in intensity could then be mapped for each pixel as demonstrated in figure 3.28. Each intensity profile was then analysed by identifying maxima angle and value through the employment of a simple secant method (figure 3.28) and maximum angle and position intensity values calculated.

These two critical parameters are the main reference points to create the c-axis map. According to the Euler map from EBSD, the red channel would correspond to the value of Euler 1, and the green channel represents the value of Euler 2. These two assumptions must have to be used to create the C axis map from PLM data. The orientation for ϕ_2 was ignored as no correlation could be drawn because it represents the rotation around the C axis.

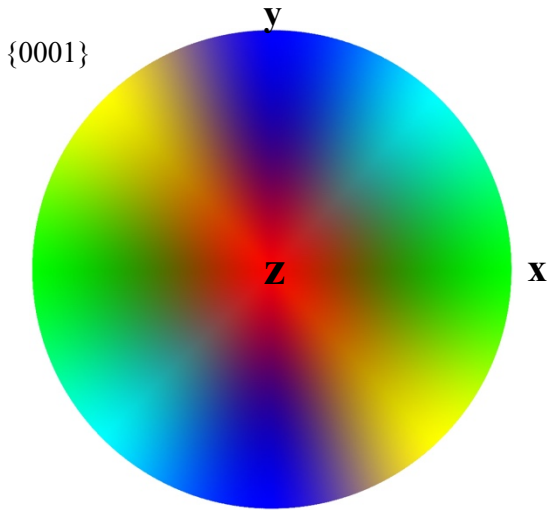


Figure 3.27 Colour correlation employed by PLM technique. Correlation between the intensity plots (figure 3.20 and 3.23) and crystal orientation map.

To obtain a comparative EBSD map based solely on c-axis orientations a ‘basal pole figure’ colouration was employed (see figure 3.27) in which orientations were plotted according to stereographic projections onto the colour wheel presented in figure 3.27. Orientation data collected from polarised light microscopy via the method described above was then presented in an identical manner. A comparison on these two methods of orientation data acquisition is presented in figure 3.28. The results demonstrate there is scope to develop into this variant of quantitative PLM as low cost alternative to EBSD.

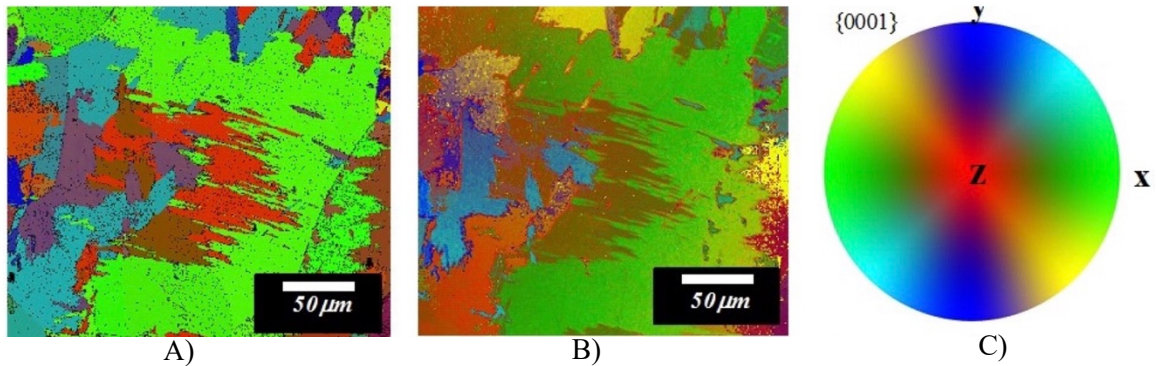


Figure. 3.28 The crystal orientations maps from the same sample area by using the PLM method and EBSD. A) illustrates Crystal Orientation Map by using the EBSD method. B) represents the crystal orientation map by using the PLM method and C) Maps are pole figure coloration (stereographic projection) denoted key.

The final analysis shows a very close correlation between the map generated by PLM and EBSD approach. The images were collected at every 2 degrees, and analysed each images pixels by pixels. The main reference data to analyse the images are figures 3.20 and 3.23. The position of maximum intensity and the value of maximum intensity are two fundamental data for the PLM approach to investigate the crystal orientation of the HCP crystal system. Some grains demonstrate the colour difference between PLM and EBSD. This happens due to the stage rotation approach, whereby rotating the stage manually, we introduce mechanical error to the approach. In this case, we introduce a novel approach by employing the circular polarised light microscope technique, which will be discussed in detail in chapter 4.

3.11. Shortcomings of the linear cross-polarised acquisition method

Some systematic errors noticed in employing linearly polarised light technique these errors noticed as artefact such as changes in absolute intensity through the cycle and curve

disjointed at a stage position around 120°.

3.11.1 Stage rotation errors

The PLM technique is compared directly to EBSD, which is a highly accurate technique. Rotating the stage and crystals physically introduces accuracies limitation to the final crystal orientation map, and this error is noticed during quantitative analysis. The error can be eliminated by finding an approach to analyse the light reflected from the sample and keep the sample in a stationary position.

3.11.2 Light source errors

Using a halogen light source means a higher intensity of light can be passed through the polariser filter. However, poor quality of light consistency is achieved through the whole microstructure surface. This can cause systematic errors in analysing grains individually and offset the final analysis. The error can be fixed by employing more consistent light such as LED or monochromatic light sources.

3.11.3 Cross polarised light condition errors

Differing intensities between peaks are a function of the illumination field across the image. The sample is swapped with a completely isotropic sample (mirror), and the same effect is noticed. Changing the state of light before reaching the sample surface can remove the mentioned problems.

3.12. Conclusions

Three separate analysis techniques (EBSD, unfiltered & polarised reflected light microscopy) have been applied to identical areas of microstructure in four distinct forms. It was noted that only etched microstructures suitably described the boundary structures

that defining the microstructural form (i.e. lath, equiaxed, acicular), but the character of these boundaries (low or high angle) could not be ascertained. Qualitative comparisons between single images acquired using EBSD and PLM revealed that PLM accurately described areas of common orientation without detecting low angle boundaries. Application of a simple variant of quantitative polarised light microscopy demonstrated the ability of PLM to resolve and map c-axis orientations, giving an indication of its feasibility as an alternative to EBSD in industrial applications. The technique can be improved by distinguishing an approach that can keep the sample in a stationary position, and instead of rotating the sample, managed to rotate the light under very precise conditions. In chapter 4 we introduce a novel approach to investigate the crystal orientation map of a cubic crystal which can be employed to investigate the crystal orientation on HCP crystal system as well.

The Circularly Polarised Light (CPL) can remove the systematic error introduced by the linear polariser filter to the data. The sample was analysed in a stationary position by employing the new technique, and a monochromatic light source was used to produce purely circularly polarised light. The problems mentioned in section 3.11 were solved by employing Circular Polarised Light Microscope (CPLM) technique, which is discussed in detail in chapter 4.

Publication on this chapter: *“An Assessment of Polarized Light Microscopy for the Quantification of Grain Size and Orientation in Titanium Alloys via Microanalytical Correlative Light to Electron Microscopy (CLEM)”* In journal of the Microscopy & Microanalysis 2018 (10.1017/s1431927618002490).

Chapter 4 Circular Polarised Light Microscopy (CPLM)

Following early successes by the authors and other investigators with optically birefringent metals, this investigation assesses the suitability of reflected circular polarised light microscopy (CPLM) as a rapid low-cost alternative to EBSD for cubic systems. Direct comparisons between EBSD crystal orientation maps (COMs) and a quantitative determination of the character of reflected polarised light images is presented to demonstrate that this technique can provide quantitative texture information for aluminium. Further, the inherently surface sensitive nature of the technique allowed further verification of orientation relationships between the substrate and surface oxide only previously made possible by high resolution transmission electron microscopy. In this approach, the research tried to tackle the problem mentioned in chapter 3.

4.1. Introduction

The influence of texture (grain orientation distribution) on the mechanical performance of aluminium is well documented (10,19,78). Assisted primarily by crystal orientation mapping (COM) and electron backscatter diffraction EBSD (70,112). Although now widely used, EBSD is still a specialized technique that is both expensive and potentially time consuming for assessing texture characteristics as routine design / quality control criteria in an industrial environment (78,113).

Previous investigations in other fields (specifically biosciences) demonstrated success in resolving differences in optical birefringence behaviour in transmitted light microscopy (27,99–101) (More recently, it has been applied in reflection for birefringent crystals order to investigate microtexture, first introduced by Hamed Safaie 2018 and subsequently by Luisa Böhme 2018 (98,114). In both cases determinations of the correlation between

birefringence and crystal orientation were made by linearly cross polarised condition. This has two practical disadvantages 1) careful simultaneous control of two independent polarisers is required for a stationary sample or else 2) the sample must be eccentrically rotated 360° and subsequent acquisition data transposed to determine the orientation. Whilst adequate to determine orientation relations for the technique, these steps significantly slow the acquisition rate and introduce additional measurement error.

The goal of the present study was to demonstrate two key novel steps in the development of this technique 1) that these practical and optically inherent limitations could be overcome 2) that this new method could be applied to inherently optically isotropic materials. A novel approach to optically determine the microtexture of optically isotropic and cubic material using Circular Polarised Light Microscopy (CPLM) is therefore investigated. This method negates the requirement for complex manipulation of either sample or microscope and is validated by EBSD data acquired through correlative light and electron microscopy (CLEM). The potential flexibility, reliability and speed of this new technique is compared to EBSD with a view to providing recommendations for its wider implementation (11,70,73,80).

The alloy studied is a commercially available 2XXX aluminium alloy. It has long been the case that this alloy group can be anodised to generate qualitative optical orientation contrast (26). Franklin and Stirland discovered in 1963 that this optical anisotropy is due to variations in pore inclination as the formed Alumina on the surface is in different crystals. This has been previously used to help determine phase proportions and microtextural morphology (115). However, to the authors knowledge this has never been used to quantitatively determine the orientation of the underlying crystal, which is attempted here. Nevertheless, previous research in the field of electrochemistry has examined the development of this oxide layer in the context of surface passivation (17). These studies determined an orientation relationship between the substrate and nanometre scale oxide through high resolution TEM. This found that the [0001] direction in the HCP oxide was

parallel to the [001] direction in the FCC substrate, albeit this was defined from a limited number of cases given the significant complexity in making these measurements. The inherently surface sensitive nature of the technique proposed coupled with the EBSD measurements permits more extensive insight into these observations and the potential for similar approaches with other cubic systems (11,73,110,112).

4.2. Experimental procedure

4.2.1. Material Preparation

Table 4.1 Composition of major elements in 2XXX

<i>Element</i>	<i>Al</i>	<i>Cu</i>
<i>Wt. %</i>	<i>98</i>	<i>2</i>

The Aluminum-2% Copper alloy characterised contains broadly used in industry due to low densities good mechanical properties such as high strength to weight ratio and excellent corrosion resistance (116,117). The sample was subjected to standard metallographic preparation routes, with a final polish using a Struers OP-S solution with 10% H₂O₂ by volume on a Struers MD-Chem medium for 10 minutes. The material was anodised using Barker's reagent(5ml HBF₄ (48%) + 200ml. H₂O) at J=0.2 A/cm² for 60s at room temperature) using a Kristall 680 fully automatic electrolytic polisher and etcher. These conditions were fixed to produce the required thickness of alumina on the surface in the same way as mentioned by (31,112,118,119)

4.2.2. EBSD

EBSD data was collected on a Carl Zeiss Crossbeam 550 with Oxford Instruments Nordilux 2 high speed EBSD Camera in Aztec. The data was acquired before anodising the sample

as the Alumina on the surface prevented generation of the signal for Kikuchi bands. An accelerating voltage of 20kv was employed carried out on the sample with step size of 5 with the sample tilted to 70° . at working distances of 17-20mm. The EBSD system was calibrated using a cleaved silicon specimen of known crystallographic orientation (within 0.5°). In the majority of cases EBSD data is presented in the form of Crystal Orientation Maps (COMs) employing modified Euler colour distribution which is explained in detail later (70,73).

4.2.3. Light path design for CPLM

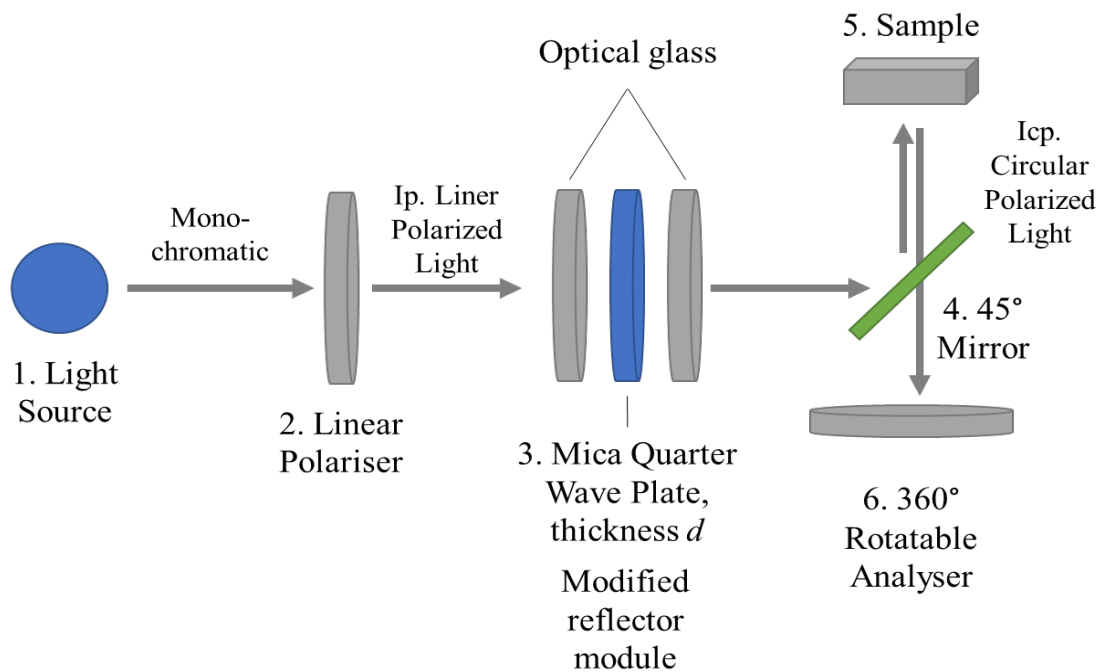


Figure 4.1 Optical path for CPLM where 1 is monochromatic light source, 2 is the linear polariser, 3 is quarter wave plate, 4 is a mirror with angle of 45° , 5 is the sample and 6 is 360° rotatable analyser.

Unlike the linear polarised light technique particular type of light source needs to be employed for circularly polarised light microscopy. The wavelength needs to be very specific as the light needs to be absolutely circularly polarised. Any wavelength changes will change the light to elliptically polarised light and completely offset the final data set. Also, monochromatic light must be employed to enable the technique to analyse the absolute intensity. In case of employing the LED or Halogen light, the light passing through the quarter wave plate will transform light into an elliptically polarised light. Also, having a broad wavelength band will cause the light reflected from each sample with a different colour. This would disable the technique of analysing the intensity profile through the rotation of the analyser.

The mica quarter wave plate thickness was determined using equation 4.1.

$$N\lambda = \pm(n_e - n_o)d \rightarrow d = \left| \frac{\lambda}{4(n_e - n_o)} \right|$$

Eq. 4.1

Where λ is the wavelength of the source light and d is the thickness of the quarter wave plate. N is the retardation which can be expressed as fraction of wavelength. Quarter wave plate retardation is $N = \frac{1}{4}$ (92,93). n_o represents the ordinary and n_e illustrates the extraordinary refractive indices (92).

The fidelity of circular polarisation was experimentally verified by capturing the intensity of a mirror reflection through a 360° rotation of the analyser with the Left Circular Polarised (LCP) light reflected from the mirror to produce a Right Circular Polarised (RCP) state. In this condition the intensity remained consistent independent of the rotation of the analyser (Figure. 4.2) demonstrating there is no elliptical character to the light, Figure 4.2

proves the $\frac{1}{4}$ wave plate thickness and wavelength are suitable. (85,92,120,122).

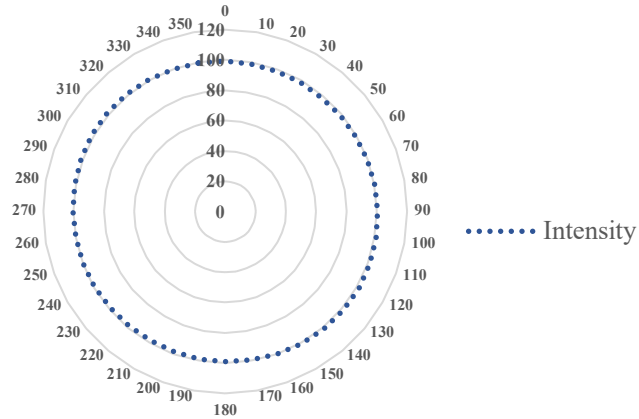


Figure 4.2. Intensity plot captured from the mirror reflection of modified circularly polarised light microscopy through 360 degrees of analyser rotations.

To ensure that the interaction between light and the sample are understood theoretically the following approach was adopted to describe the light path and beam polarisation state. The output light polarisation state before reaching the sample can be calculated by:

$$S' = (S) (Mp) (Mr) (Mm)$$

Eq. 4.2

Where S is the Stokes parameter of input unpolarised light, Mp is the Mueller matrix for linearly polariser filter, Mr is the Mueller matrix for a rotator and Mm symbolized the Muller matrix for the mirror.

Mueller matrices can be used to specify the state of polariser and the quarter wave plate whilst the character of the beam was described by four different observables Stokes parameters (S_0, S_1, S_2, S_3). The first Stokes parameter S_0 describes the total intensity of the light; the second parameter S_1 describes the amount of linear horizontal or vertical polarisation, the third parameter S_2 describes the amount of linear $+45^\circ$ or -45° and, finally, S_3 describes the preponderance of right circular polarised light over left circular

polarised light. which are represented by Equation 4.3.

$$S = \begin{pmatrix} S_0 \\ S_1 \\ S_2 \\ S_3 \end{pmatrix}$$

Eq. 4.1

The state of unpolarised light, i.e. the monochromatic light source is:

$$S = \begin{pmatrix} S_0 \\ S_1 \\ S_2 \\ S_3 \end{pmatrix} = \begin{pmatrix} 1 \\ 0 \\ 0 \\ 0 \end{pmatrix}$$

The Mueller matrix for a perfect linear polariser (M_p) with transmitted axis at an angle $\Theta = 45^\circ$ is:

$$M_p = \begin{pmatrix} 1 & \cos 2\Theta & \sin 2\Theta & 0 \\ \cos 2\Theta & \cos^2 \Theta & \sin 2\Theta \cos 2\Theta & 0 \\ \sin 2\Theta & \sin 2\Theta \cos 2\Theta & \sin^2 \Theta & 0 \\ 0 & 0 & 0 & 0 \end{pmatrix} = \begin{pmatrix} 1 & 0 & 1 & 0 \\ 0 & 0 & 0 & 0 \\ 1 & 0 & 1 & 0 \\ 0 & 0 & 0 & 0 \end{pmatrix}$$

Eq. 2.4

The Mueller matrix of the quarter plate (M_r) with the fast axis of 0° and the phase delay \emptyset of 90° can be expressed by Equation 4.5.

$$M_r = \begin{pmatrix} 1 & 0 & 0 & 0 \\ 0 & 1 & 0 & 0 \\ 0 & 0 & \cos \emptyset & -\sin \emptyset \\ 0 & 0 & \sin \emptyset & \cos \emptyset \end{pmatrix} = \begin{pmatrix} 1 & 0 & 0 & 0 \\ 0 & 1 & 0 & 0 \\ 0 & 0 & 0 & -1 \\ 0 & 0 & 1 & 0 \end{pmatrix}$$

Eq. 4.3

The mirror symmetry relation (M_m) represents the Mueller matrix in the following form.

$$Mm = \begin{pmatrix} a & b & 0 & 0 \\ b & a & 0 & 0 \\ 0 & 0 & a & b \\ 0 & 0 & -b & a \end{pmatrix} = \begin{pmatrix} 1 & 0 & 0 & 0 \\ 0 & 1 & 0 & 0 \\ 0 & 0 & -1 & 0 \\ 0 & 0 & 0 & -1 \end{pmatrix}$$

Eq. 4.4

The state of the output light for this case will then appear as a left circular polarised light (LCPL).

$$S' = \begin{pmatrix} 1 \\ 0 \\ 0 \\ -1 \end{pmatrix}$$

As such the experimental and theoretical approaches agree and demonstrate that the modified incident light path is suitable for the CPLM technique. Therefore any changes in polarisation state of light after interaction with the sample can be related to the orientation of the c-axis of optically anisotropic alumina crystals at the surface of an anodised sample that is reasonably free from surface defects (61,82,85,127). This incident condition was fixed for the apparatus and is henceforth referred to as “the incident light”.

4.2.4 Anodising process

The surface treatment of Aluminium by using anodisation method goes back to 1923, according to Feiyue Li and Lan Zhang. It generates a layer of Alumina divided into two types: nonporous barrier oxide and the porous oxide. These are of interest to corrosion scientists and so have been extensively studied in that context. The nonporous barrier oxide forms in a condition where the pH is close neutral (pH>5) or primary solutions such as freshwater, this causes a flat, nonporous, and featureless Alumina forms. Acidic solutions

such as Sulfuric(H_2SO_4) and fluoboric HBF_4 acids form porous structures with diameters of 5 to 100 nm and the maximum length of several microns. Under each pore consist of a barrier layer which is with the thickness of 10 to 100 nm, this porous specifies as “Anodic Cell”. The non-porous and continuous which is called a barrier layer first layer is as it makes the subsequent passage of current difficult. The operating condition and the composition of the electrolyte controls the thickness of the barrier layer. When the barrier layer has been formed, the continuous current flows and solvent etchant creates a series of attachment points on the outer part of the barrier layer. Each point corresponds to the pore of the anodic layer that is forming.

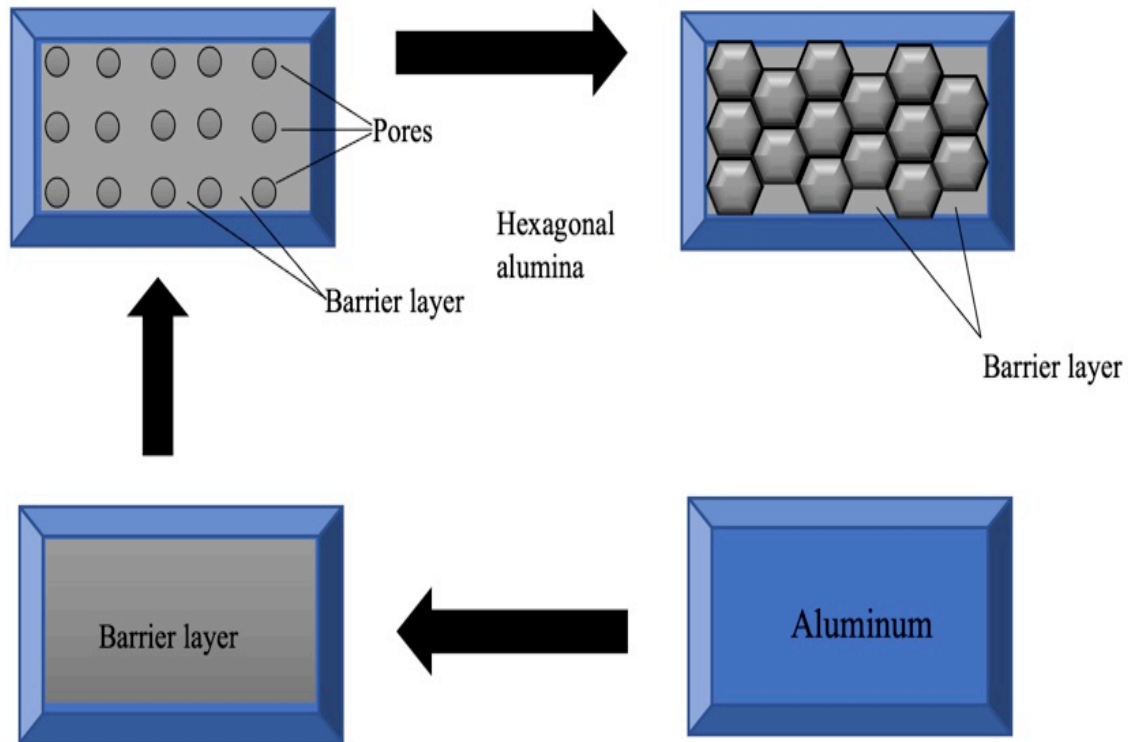


Figure 4.3. Anodised surface transformation from aluminium to hexagonal alumina.

As they form in the barrier layer before the oxide layer reaches the required thickness, it becomes evident that the passage of electro current was facilitated by the attachment points. The current is distributed in a radio manner with respect to the pore which has a semi-spherical shape. Therefore, the barrier and the oxide layer at first appeared to have a cylindrical form in the axes of the pore. Finally, due to equidistance between pores, these vertically formed cylinders transformed into a hexagonal crystal orientation with honeycomb structure (hexagonal prism shape). The same anodic film structure achieved independently to the type of the electrolyte sulphuric, chromic or fluoboric. The cell size has a linear relationship with voltage, as the voltage is increasing the cell size gets bigger too and the number of pores is decreasing, respectively. The layer of Al_2O_3 forms, and chemically bonds perfectly to the metal base also the thickness of the film is increasing as the treatment operates for a longer time (16,118,119,124–126).

4.3 Result and discussion

4.3.1 Qualitative analysis

After collecting the EBSD data, the same area was anodised and tested under circular polarised light microscopy. The intensity plot was captured by taking the intensity of each pixel position for images collected at all analyser rotations. Figure. 4.4 A - C represents how each grain appears for different illumination conditions. For pan-chromatic illumination, intensity data acquired under circular polarised light will be recorded by the detector in three different channels of colour (Red, Green and Blue). However, because a monochromatic blue ($\lambda=440$), light source was used in this study, the intensity is unaffected by chromatic shift (Figure. 4.4 C).

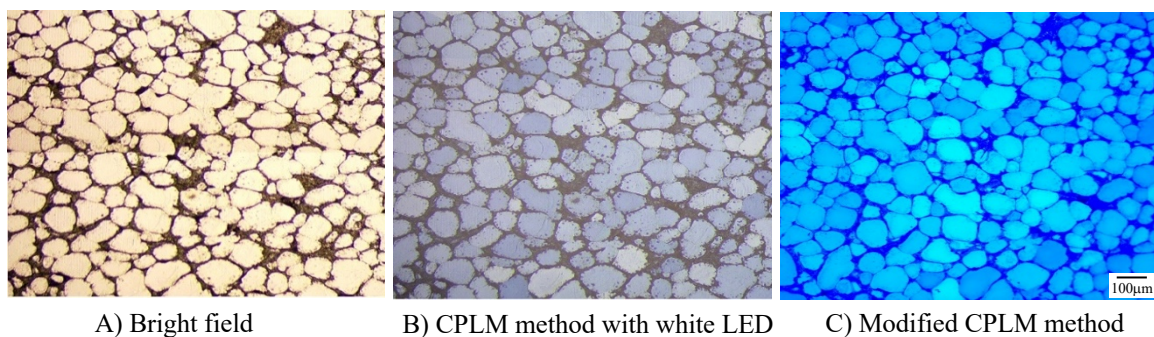


Figure. 4.4 The same area of interest under four different conditions A) Bright field with a LED light B) Circular polarised light microscopy with a LED light C) Circular polarised light microscopy with a monochromatic light.

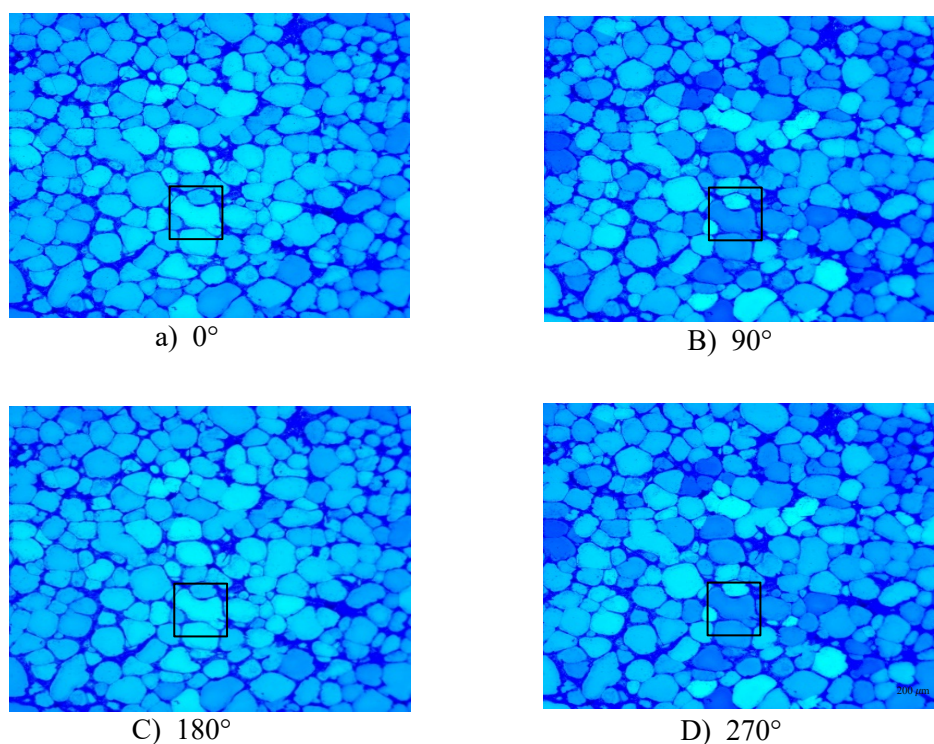


Figure. 4.5 Qualitative observations of symmetry in the contrast of images recorded under circular polarised light microscopy.

Circular Polarised light images were recorded using rotating analyser at various sample crystal orientations applied using the highlighted microstructure presented in Figure. 4.5 as an arbitrary example. Figure. 4.5 shows the symmetry observed in the appearance of images recorded at 0° , 90° , 180° and 270° of rotation respectively. Microstructural features appear similar at $0^\circ / 180^\circ$ and $90^\circ/270^\circ$ illustrating a 180° symmetry in the retardation behaviour. This observation correlates well with the crystallographic symmetry of both the $[0001]$ direction of the HCP surface oxide and the $[001]$ direction of the (FCC) substrate system (1,121) which can be linked according to the previously reported orientation relationship (16). Moreover, as the analyser was rotated, the intensity associated with individual units was found to vary sinusoidally against rotation with a phase of approximately 180° as demonstrated in Figure 4.6. This represents the intensity value for an individual grain from the dataset in Figure. 4.6 with a crystal orientation of $\phi_1 = 157^\circ$, $\Phi = 42^\circ$ and $\phi_2 = 22^\circ$. The effect of symmetry appears clearly in the plot as the FCC crystal orientation symmetry for $\phi_1=180^\circ$. The unit cell symmetry suggests that data captured from only 0° to 180° or 180° to 360° is needed to correlate the CPLM data to EBSD.

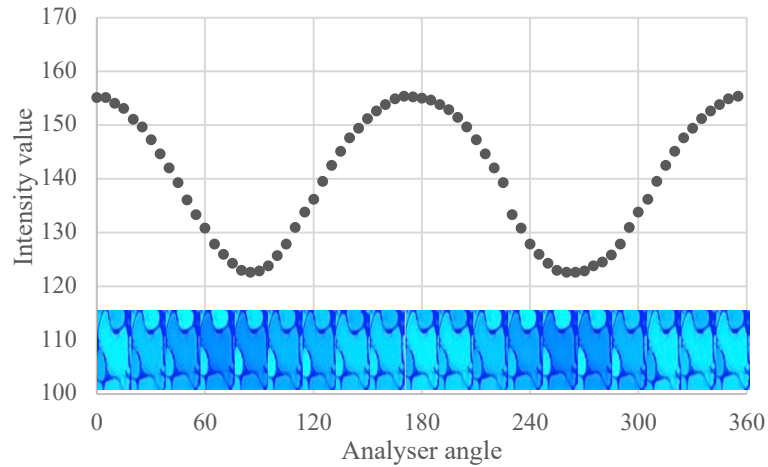
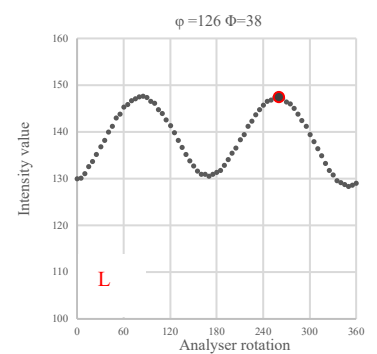
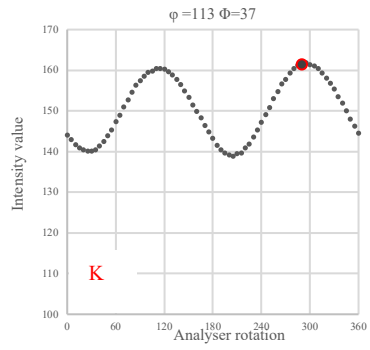
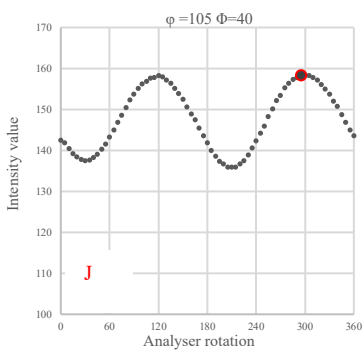
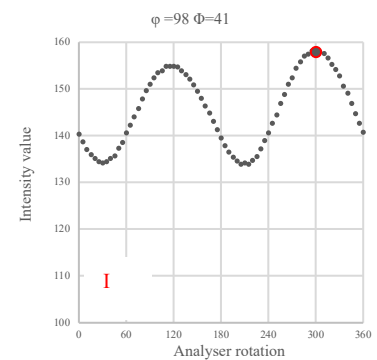
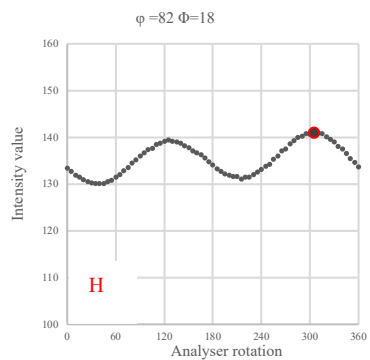
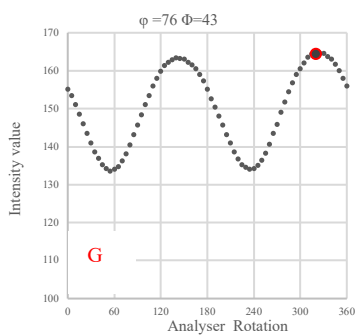
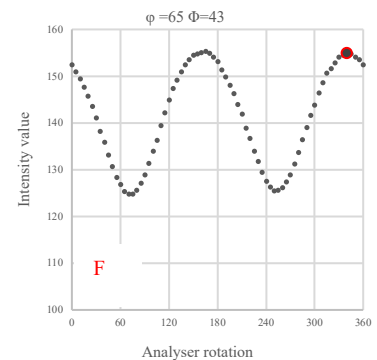
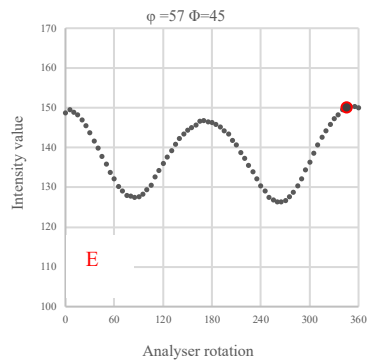
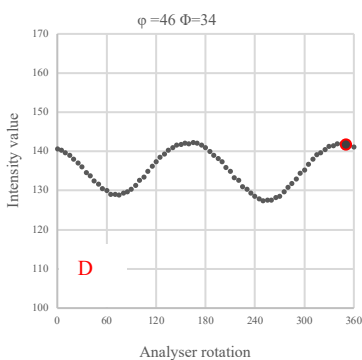
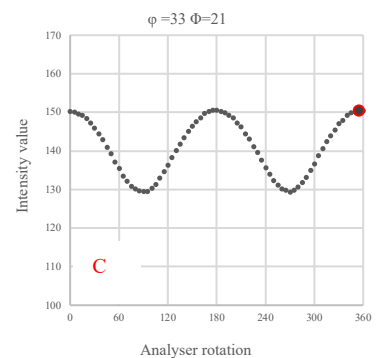
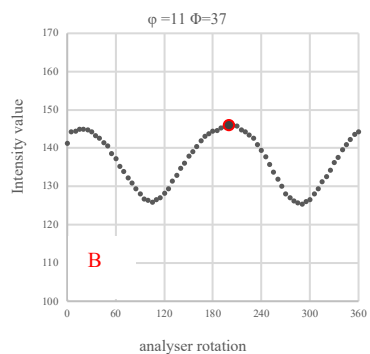
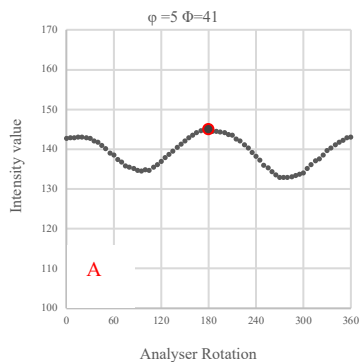


Figure. 4.6 An intensity profile and its derivative for an individual crystal orientation recorded over a complete analyser rotation.

4.3.2 Euler correlation

4.3.2.1 Euler 1 correlation

The value for S_1 and S_2 (linear parameter) can be determined by using a rotatable analyser to capture the maximum intensity value over 180° rotation of the analyser. This was achieved by correlating the measured crystal orientation by EBSD with the CPLM data for the anodised material (see Figure 4.7).



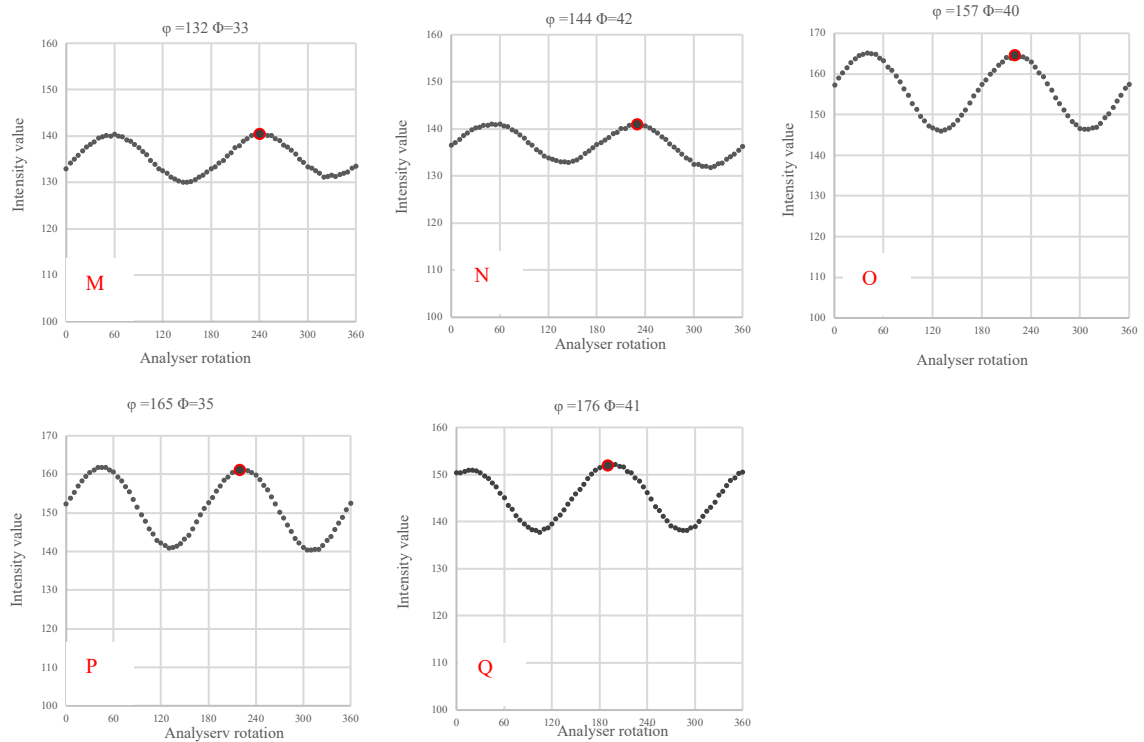


Figure 4.7 Intensity profile captured through 360° rotation of analyser for different grains with certain crystal orientations. The value for Euler1 increasing gradually to highlight the correlation between Euler1 and intensity plots.

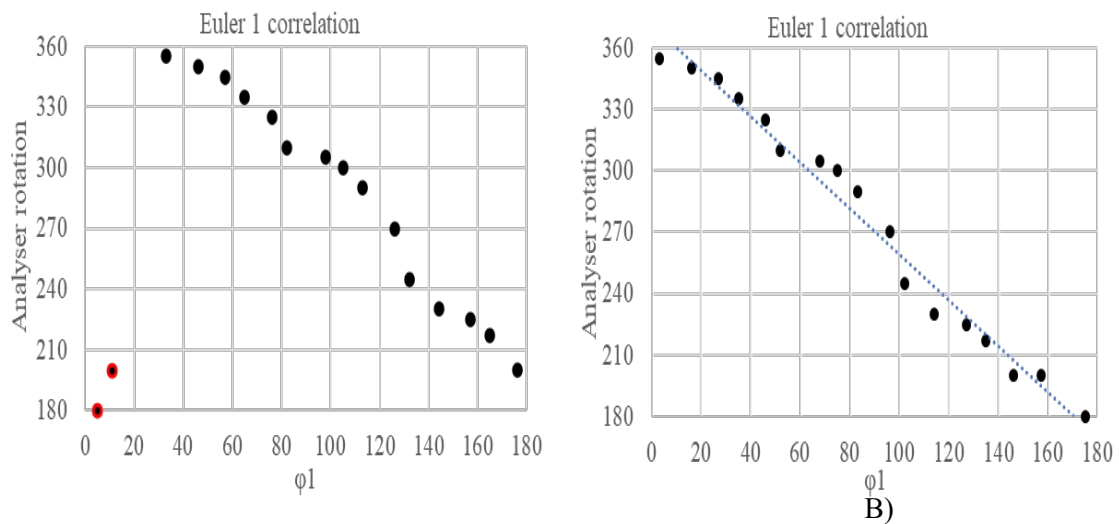
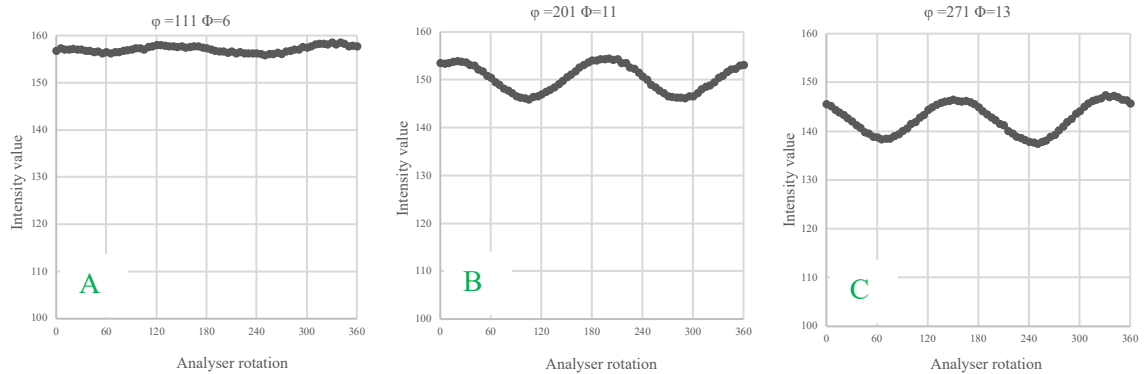


Figure. 4.8 The position of maximum intensity through 180 degrees of analyser rotation.

The first two points highlighted in figure 4.8A display a significant 15° shift in data because of an offset in the original position of the sample on the optical microscope stage compared to the position of the sample in the SEM. The data was corrected using the {001} planes and shows accurate correlation among the position of maximum intensity and Euler 1. Figure 4.8B represents the corrected position of maximum intensity over 180° rotation of Euler 1 (ϕ 1). This data proves the linear behaviour of the reflected light from the sample corresponding to the value of ϕ 1. The position of maximum intensity keeps shifting as the ϕ 1 is increasing.

4.3.2.2 Euler 2 correlation

The next step is to analyse the effect of Euler (Φ) on polarisation state (figure 4.9). The theoretical effect of crystal orientation on the state of polarisation of reflected light illustrates how the light state varies from circular to linear as the orientation of Φ reaches 45° (Figure 4.10). To mathematically validate the theory, the following approach is adopted (61,82,83,85,91).



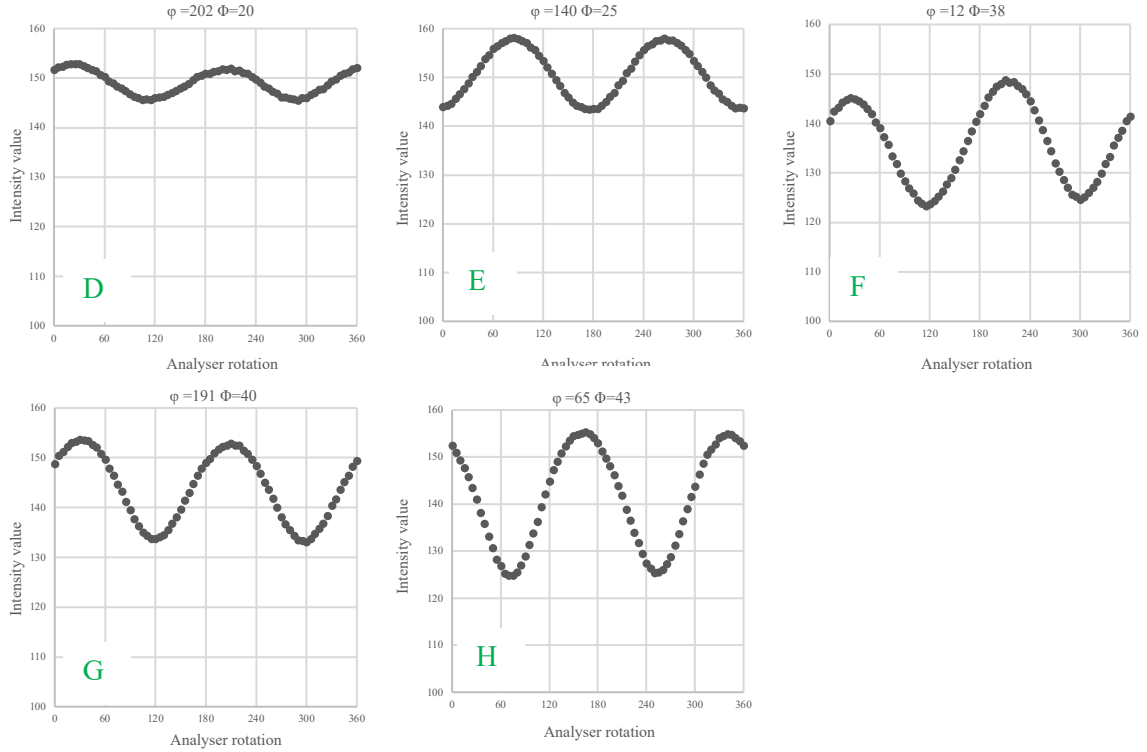


Figure 4.9 The impact of second Euler rotation to the intensity profile for each specific grain through 360° rotation of stage under cross polarised conditions.

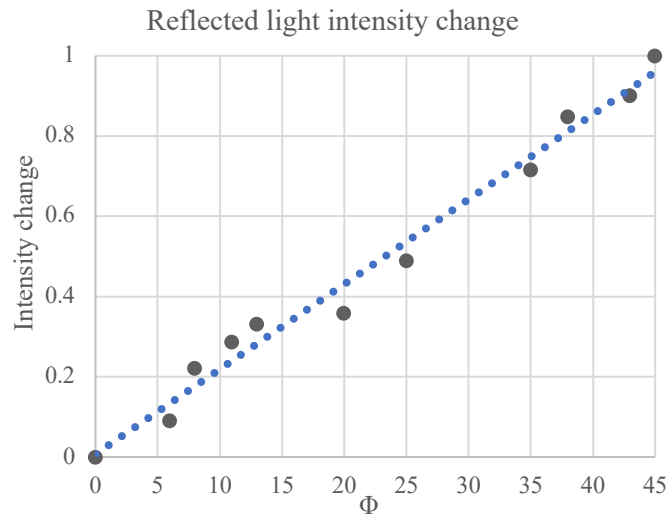


Figure 4.10 The difference between the maximum and minimum intensity over 45°

The differentiation between the maximum and minimum intensity become more dominant as the Φ value is increasing, and the state of the polarisation ends in a completely linear state when Φ reaches 45° . This means the Ellipticity parameter or S_3 value is dependent on the rotation of Φ .

Figure 4.11 plots the intensity profiles of two grains with similar crystal orientations. Both grains give intensity maxima and minima at similar analyser rotation angles, and both show comparable differences in maximum and minimum intensity, i.e. profiles are similar and the intensity difference (ΔI) remains constant, even though the absolute intensity values are different.

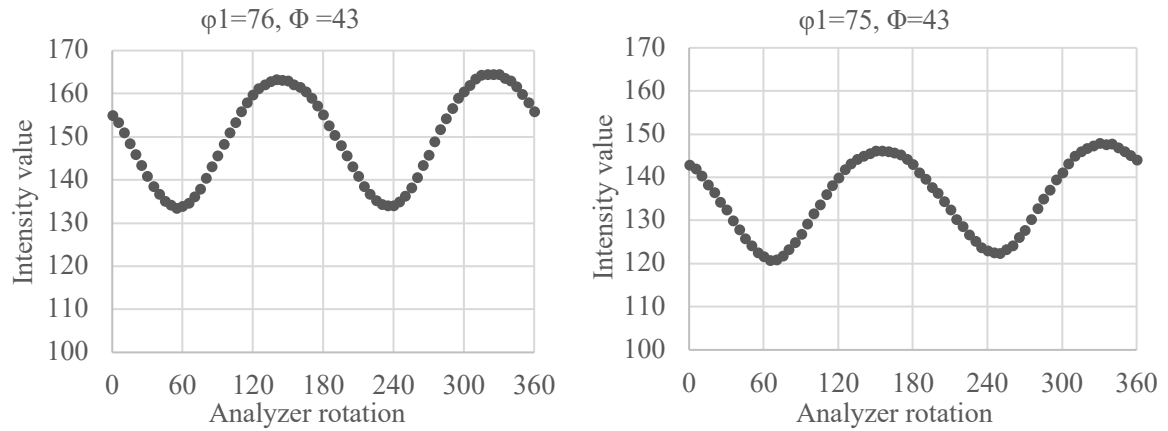


Figure 4.11 CPLM intensity data of Close C axis crystals orientations. Left intensity plot is $\phi_1=76$ and $\Phi=43$, Right intensity plot is $\phi_1=75$, $\Phi=43$

This proves that areas of common orientation can be measured by employing CPLM technique. To explore this for a wide range of orientations, the reference coordinate data for ϕ_1 collected from EBSD was compared directly with the CPLM intensity data. Figure. 4.12A presents the correlation between Euler 1 (ϕ_1) and the maximum intensity observed

through 180 degrees rotation of the analyser from 180° to 360°. This data represents the position of maximum intensity shifting from 360° to 180° as the Euler 1 (ϕ_1) is increased from 0° to 180°. Figure 4.12B presents the correlation between the difference in maximum and minimum intensity (ΔI) to Euler 2 (Φ). The symmetry of Φ is distinguished to be 45° for FCC according to Gert Nolze 2015 (133). The plot illustrates that by increasing Φ , ΔI for a specific grain would appear more noticeable. It follows that these two parameters are the main reference points required to create the c-axis map for the surface oxide and by inference the [001] FCC direction.

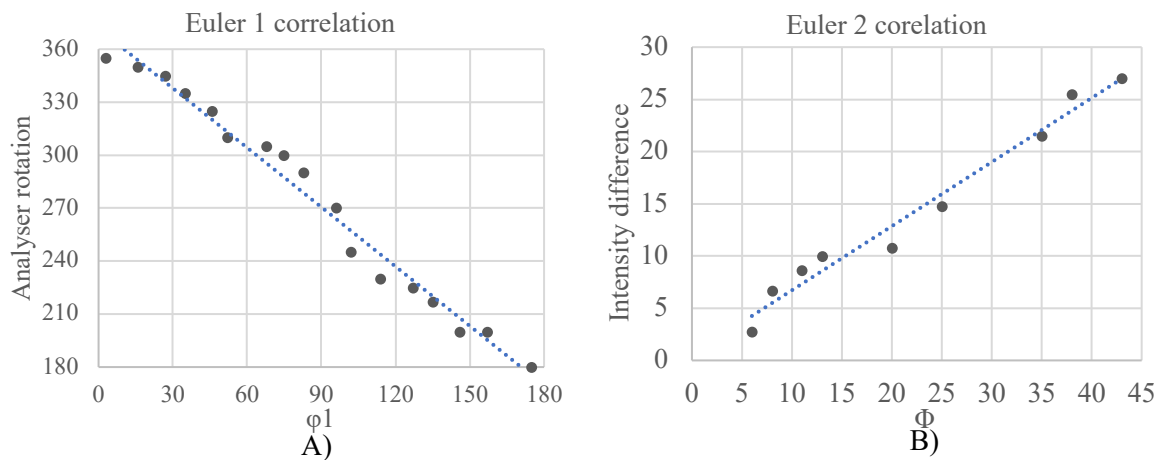


Figure 4.12 Correlation plots of CPLM data and EBSD data. A) Euler 1 correlation Plot represents the correlation between Euler 1 (ϕ_1) and analyser rotation. B) Euler 2 correlation illustrates the connection between the difference of maximum and minimum intensity to the Euler 2 (ϕ).

4.4 Theoretical validation of the observed incident beam rotation after reflection

We have shown that there is a correlation between ϕ_1 and the analyser position that yields the maximum intensity over 180° of rotation (Figure 4.12A). From a theoretical perspective

this is equivalent to Θ in Equation 4.4 and that equation can be used to calculate the linear parameter of polarised light reflected from the sample. This parameter is described by the S_1 and S_2 components of the Stokes vector. These values for equivalent analyser rotations to those in the experimental data (Figure 4.12A) are presented in table 4.2.

Table 4.2 The Stokes parameter value for S_1 and S_2 over the rotation of 180° of analyser rotation.

Analysers rotation	0°	15°	30°	45°	60°	75°	90°	105°	120°	135°	150°	165°	180°
S_1	1	0.866	0.5	0	-0.5	-0.866	-1	-0.866	-0.5	0	0.5	0.866	1
S_2	0	0.5	0.866	1	0.866	0.5	0	-0.5	-0.866	-1	-0.866	-0.5	0

We have also shown that ΔI reaches a maximum as Φ reaches 45° (Figure 4.12B). This intensity change during the reflection of circularly polarised light has been previously shown to be related to the ellipticity parameter of the Stokes vector and describes the change from circular to linear polarisation (Figure 4.13) (61,82,83,85,91). To mathematically validate our observations against this theory, the following approach is adopted:

The transverse components of light are represented by Equation 4.7.

$$E_x(z, t) = E_{0x} \cos(\tau + \delta_x)$$

Eq. 4.5a

$$E_y(z, t) = E_{0y} \cos(\tau + \delta_y)$$

Eq. 4.7b

Where t represents the time, E_{0x} and E_{0y} are the maximum amplitudes of the optical field and τ is the propagator which is constant. The subscripts x and y refer to the component direction in x and y . The propagation of E_x and E_y give rise to a vector describing a locus of points in space that generates a curve whose form can be derived using the equations 4.7a and 4.7b.

$$\frac{E_x}{E_{0x}} = \cos \tau \cos \delta_x - \sin \tau \sin \delta_x$$

Eq. 4.6a

$$\frac{E_y}{E_{0y}} = \cos \tau \cos \delta_y - \sin \tau \sin \delta_y$$

Eq. 8b.

Rearranging the terms of equation 8 and subtracting using the double angle formula gives

$$\frac{E_x}{E_{0x}} \sin \delta_y - \frac{E_y}{E_{0y}} \sin \delta_x = \cos \tau \sin(\delta_y - \delta_x)$$

Eq. 4.7a

$$\frac{E_x}{E_{0x}} \cos \delta_y - \frac{E_y}{E_{0y}} \cos \delta_x = \sin \tau \sin(\delta_y - \delta_x)$$

Eq. 4.9b

Squaring equation 4.9 and adding them together gives the equation for parameters of the polarisation ellipse:

$$\frac{E_x^2}{E_{0x}^2} + \frac{E_y^2}{E_{0y}^2} - \frac{2E_xE_y \cos \delta}{E_{0x}E_{0y}} = \sin^2 \delta$$

Eq. 4.8

Where $\delta = \delta_x - \delta_y$ (the phase difference).

This signifies that if the incident light is reflected back from a crystal with $\Phi = 0^\circ$ it will be reflected in the RCP state.

In this condition ($\delta = \pi/2$ and $E_{0x} = E_{0y} = E_0$)

$$\frac{E_x^2}{E_{0x}^2} + \frac{E_y^2}{E_{0y}^2} - \frac{2E_xE_y \cos \delta}{E_{0x}E_{0y}} = \sin^2 \delta \text{ leads to } \frac{E_x^2}{E_{0x}^2} + \frac{E_y^2}{E_{0y}^2} = 1$$

According to cubic crystal symmetry the maximum value for Φ without describing an indistinguishable reflection is 45° . In this condition ($\delta=0$ and $E_{0x} = E_{0y}$) giving:

$$\frac{E_x^2}{E_{0x}^2} + \frac{E_y^2}{E_{0y}^2} - \frac{2E_xE_y \cos \delta}{E_{0x}E_{0y}} = \sin^2 \delta \text{ leads to } \left(\frac{E_x}{E_{0x}} + \frac{E_y}{E_{0y}} \right)^2 = 0$$

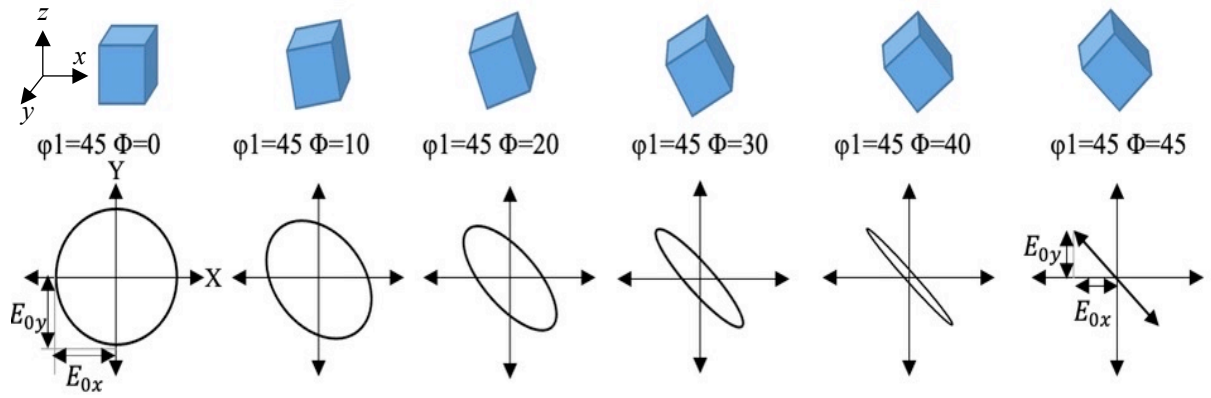


Figure. 4.13 The effect of Φ rotation on the ellipse amplitude.

When this theoretical calculation of the Ellipticity parameter (Figure 4.14A) under perfect conditions was compared with the experimentally observed intensity data, (Figure 4.14B) it followed and inverse relationship. This confirms that the Ellipticity parameter (or the value of S_3) which can be determined by ΔI is dependent on the Φ component of the crystal orientation.

By combining the observations presented in Figure 4.12A and 4.12B with the theoretical descriptions presented above it is possible to unambiguously determine the polarisation state. This can be represented on the Poincare sphere (Figure 4.16), which is a common way to illustrate the state of the light reflected from the sample (128) but is less useful for quantitative observations. Instead, here we have for the first time unified theoretical and experimental descriptions of the polarisation state with the crystal orientation. The relationship between the intensity profile and the polarisation state is illustrated in Figure. 4.15, where Ψ is the analyser position of maximum intensity and X is ΔI . With reference

to the theoretical description outlined above, the Stokes parameters can then be expressed in terms of Ψ and X . The approach taken to calculate the Stokes parameters and relate them to experimentally determined crystal orientation is shown in equations 4.11-4.13 below (83,87,91,128–132). For convenience, various examples comparing the measured and calculated outcomes are presented in table 4.3.

$$S_1 = \cos(2X)\cos(2\Psi)$$

Eq. 4.9

$$S_2 = \cos(2X)\sin(2\Psi)$$

Eq. 4.12

$$S_3 = \sin(2X)$$

Eq. 4.13

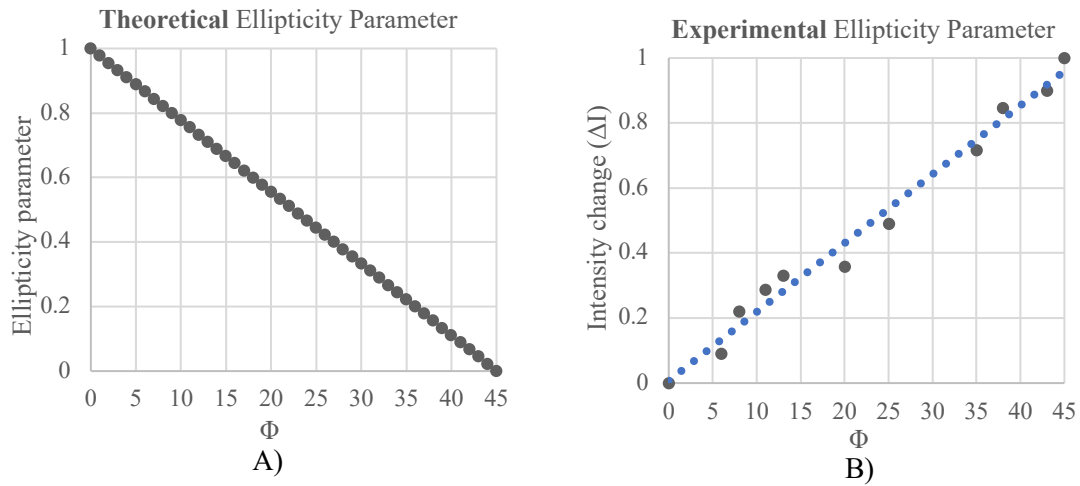


Figure 4.14 Correlation between ellipticity parameter and the difference between max and min intensity (ΔI value) for a) theoretically calculated ellipticity parameter and b) experimentally measured ellipticity parameter.

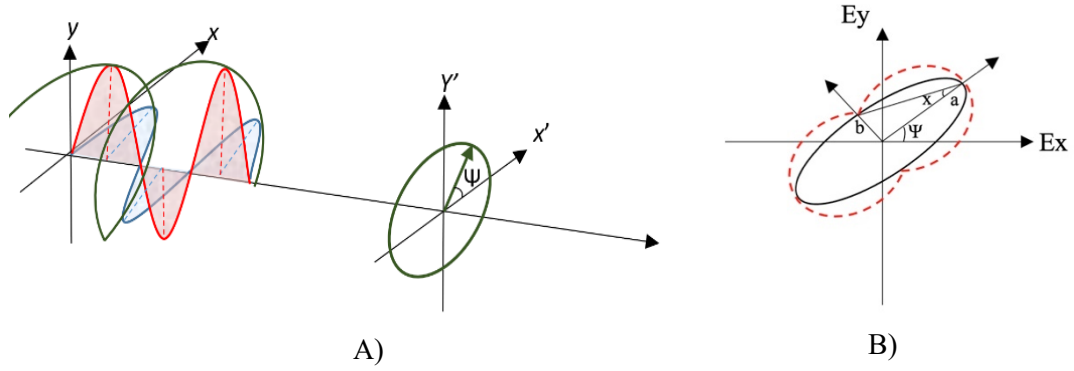


Figure 4.15. A) Formation of an elliptical ellipse by electrical field at the coordination of Ψ . B) Elliptical polarised ellipse corresponding to the intensity profile. Ψ is the orientation angle of the ellipse and X the measure of the ellipticity. a is the major axis and b is the minor axis.

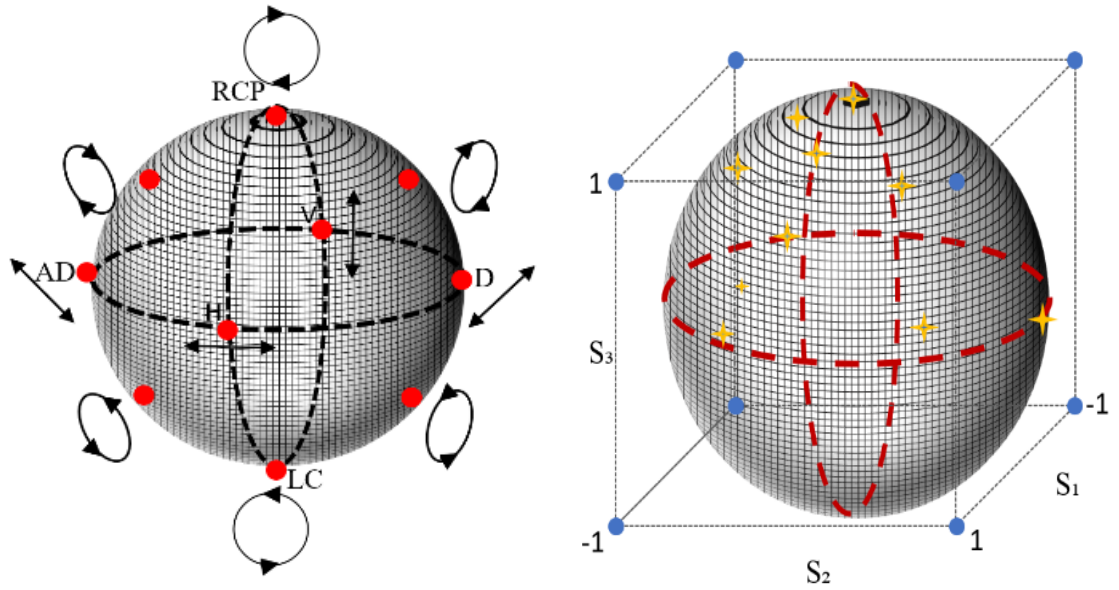
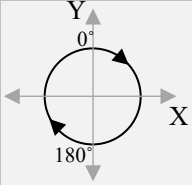
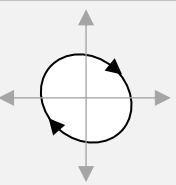
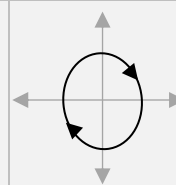
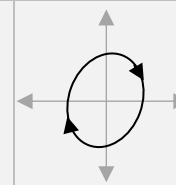
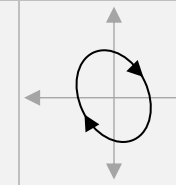
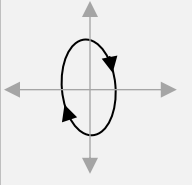
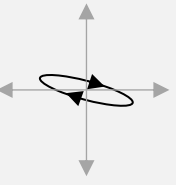
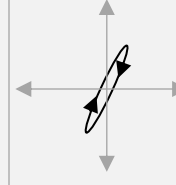
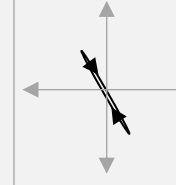
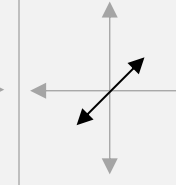


Figure 4.16. Representation of polarization state of table 4.3 on a Poincare sphere. A) General format of Poincare sphere representing systematic range of polarization state. B) Representation of polarized ellipse in table 4.3 on Poincare sphere.

Table 4.3. Ellipse structure and stoke parameters for different range of crystal orientation.

C axis Euler angle (EBSD)	$\phi 1=14^\circ$ $\Phi=0^\circ$	$\phi 1=111^\circ$ $\Phi=6^\circ$	$\phi 1=33^\circ$ $\Phi=8^\circ$	$\phi 1=201^\circ$ $\Phi=11^\circ$	$\phi 1=271^\circ$ $\Phi=13^\circ$
Shape of the ellipse (CPLM)					
Maximum intensity angle(CPLM)	NA	130°	175°	20°	155°
Stokes parameters	$S_{out} = \begin{pmatrix} 1 \\ 0 \\ 0 \\ 1 \end{pmatrix}$	$S_{out} = \begin{pmatrix} 1 \\ -0.035 \\ -0.203 \\ 0.978 \end{pmatrix}$	$S_{out} = \begin{pmatrix} 1 \\ 0.27 \\ -0.04 \\ 0.96 \end{pmatrix}$	$S_{out} = \begin{pmatrix} 1 \\ 0.28 \\ 0.23 \\ 0.92 \end{pmatrix}$	$S_{out} = \begin{pmatrix} 1 \\ 0.27 \\ -0.33 \\ 0.89 \end{pmatrix}$
C axis Euler angle (EBSD)	$\phi 1=33^\circ$ $\Phi=20^\circ$	$\phi 1=305^\circ$ $\Phi=36^\circ$	$\phi 1=191^\circ$ $\Phi=40^\circ$	$\phi 1=75^\circ$ $\Phi=43^\circ$	$\phi 1=157^\circ$ $\Phi=45^\circ$
Shape of the ellipse (CPLM)					
Maximum intensity angle(CPLM)	175°	105°	25°	150°	45°
Stokes parameters	$S_{out} = \begin{pmatrix} 1 \\ 0.63 \\ -0.11 \\ 0.76 \end{pmatrix}$	$S_{out} = \begin{pmatrix} 1 \\ -0.82 \\ -0.475 \\ 0.31 \end{pmatrix}$	$S_{out} = \begin{pmatrix} 1 \\ 0.63 \\ 0.75 \\ 0.17 \end{pmatrix}$	$S_{out} = \begin{pmatrix} 1 \\ 0.5 \\ -0.86 \\ 0.069 \end{pmatrix}$	$S_{out} = \begin{pmatrix} 1 \\ 0 \\ 1 \\ 0 \end{pmatrix}$

4.5 Final Microstructure map

The final stage is to compare the crystal orientation maps directly between the CPLM method and the EBSD method (Figure 4.17). A MATLAB code analysed images recorded at all analyser positions pixel by pixel. Each pixel position for the dataset therefore contains information on the whole intensity profile. The position of maximum intensity and ΔI were determined and used via the approach presented above to calculate ϕ_1 and Φ for every pixel position. To obtain a comparative EBSD map based solely on [001] directions, a ‘basal pole figure’ colouration was employed in which orientations are plotted according to stereographic projections onto the colour wheel. According to the Euler map from EBSD (Figure 4.17A), the red channel corresponds to the value of ϕ_1 , and the green channel represents the value of Φ . This colour convention was used to create an equivalent map from CPLM data. In this case the value of ϕ_2 is irrelevant because it represents the rotation around the HCP c-axis (FCC [001] direction) which cannot be resolved by the CPLM technique. Those pixels are considered grain boundaries when the intensity profile falls 70%, and the absolute intensity stays consistent.

The CPLM method simplifies data collection and removes the necessity for step size determination, i.e. data is collected at a consistent resolution determined by the wavelength of the monochromatic light source (440nm). The orientations of each crystal are clearly distinguished by CPLM method and validated by EBSD, however there are some differences. The highlighted CPLM grains appear as different colours compared to the EBSD map, but this is not due to any errors in the CPLM approach. The CPLM method utilizes the symmetry of the cubic unit cell. However, post-processing EBSD packages such as Tango, Crystal Aztech and TSL report crystallographic data with respect to the Euler twist (72,108,109,133). The absence of a standard symmetry for the unit cell causes

the above programs to represent the grains with different Euler colours although they may have the very similar orientations. This particular error is described in detail by (1,133) and is highlighted by this CPLM technique. The difference becomes more noticeable when $\phi_1 > 300^\circ$, e.g. the highlighted crystals in Figure 4.17A all have their $\phi_1 > 330^\circ$, according to crystal symmetry they should be treated the same as crystals with $\phi_1 > 150^\circ$.

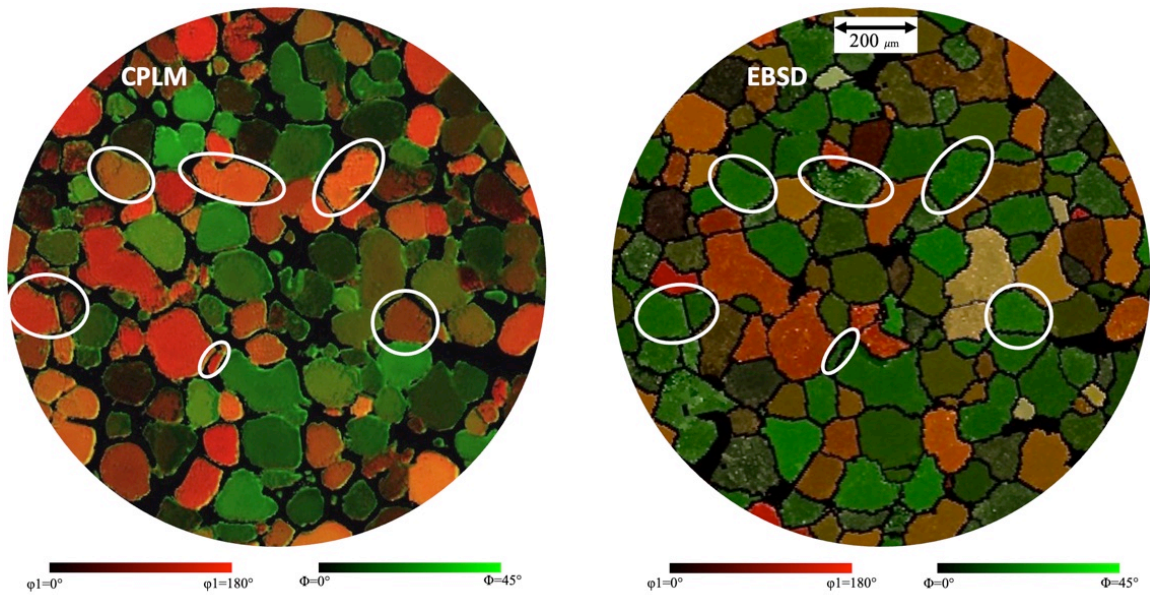


Figure 4.17. The c-axis crystal orientations maps from the same sample area by using the CPLM method and EBSD. A) represents the crystal orientation map by using the CPLM method and B) illustrates Crystal Orientation Map by using the EBSD method.

4.6. Anodised data

Anodised aluminium alloys become optically anisotropic under polarised light microscopy due to the light interaction between the oxidised film on the grain surface. The light reflection from the anodised surface and the interface between the anodic layer and Al substrate intertwined with scattering and absorption within the anodic layer generates a specific optical appearance as has been previously described (16,26,124).

The authors wanted to ensure that the anodisation process itself did not have an effect on the measured orientations (i.e. that the previously reported oxide/substrate orientation relationships were preserved). For that reason the entire experiment was repeated after re-polishing (to acquire EBSD data) and re-anodising (to acquire CPLM data) the sample surface (whilst preserving the original section of the microstructure).

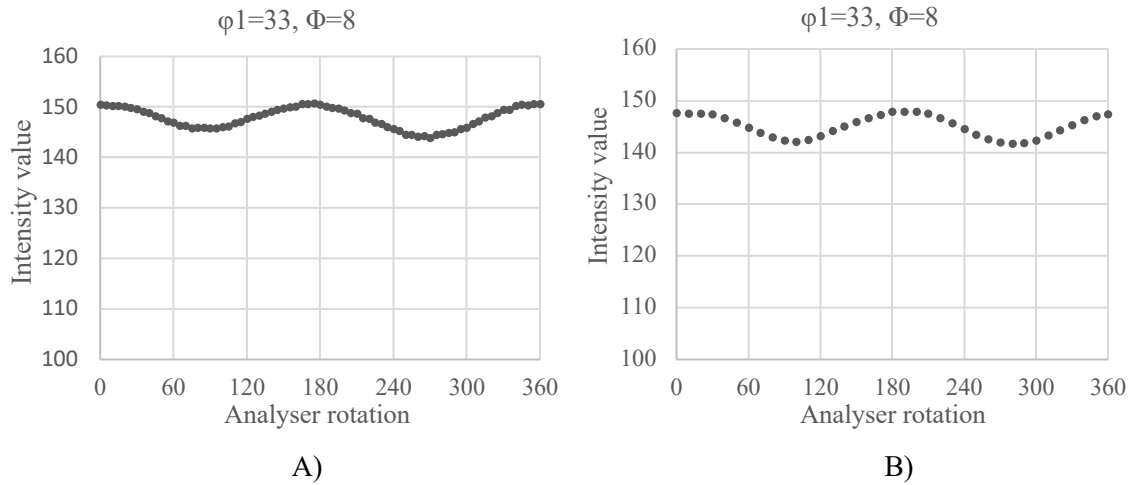


Figure 4.18. The intensity plots from the same grain. A) First time anodisation data collected on every 5° of analyser rotation. B) Intensity plot of re-anodised grain, data collected on every 10° of analyser rotation.

Figure 4.18 characterizes no change in intensity between the first and re-anodisation of the same grain. Data was collected for a variety of crystal orientations to confirm the independency of the anodised layer to the substrate crystallographic orientation. Each specific grain illustrated identical position of maximum intensity with respect to the analyser rotations. Also, the data showed each specific grain to maintain identical value for the difference between maximum and minimum intensity unconventionally to the anodised layer(16,124–126).

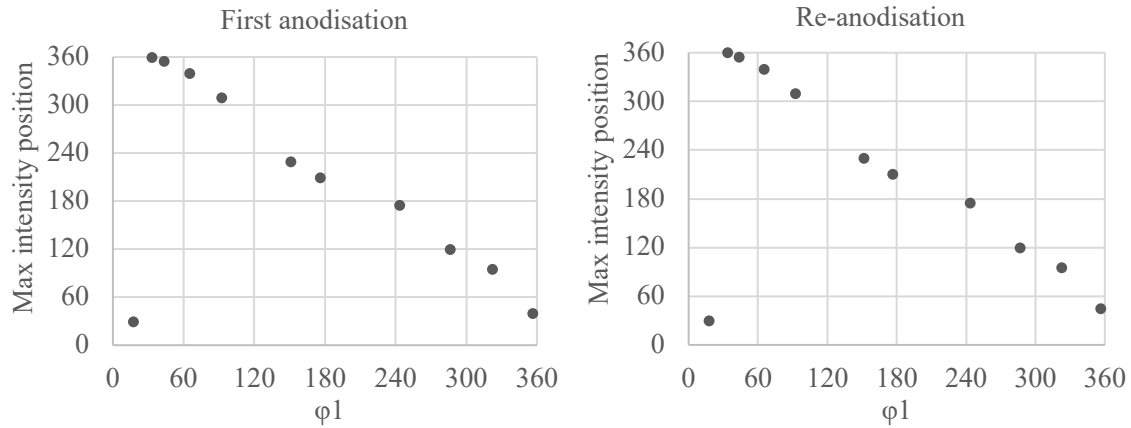


Figure 4.19 Compared data of maximum intensity position from the first anodisation and re-anodised sample.

4.7. Conclusions

Four separate analysis techniques (EBSD, bright field optical microscopy, pan-chromatic circular polarised light microscopy and monochromatic circular polarised light microscopy) have been applied to identical areas of microstructure of an FCC Al-Cu alloy in two distinct forms. The CPLM was shown (we believe for the first time) to have the potential to be employed as an accessible, cheap and accurate approach to produce crystal orientation maps of some FCC crystal systems.

- Qualitative comparisons between single images acquired using EBSD and monochromatic CPLM revealed that monochromatic CPLM accurately described areas of common [001] directions for FCC crystal structures (via its orientation relationship with the [0001] direction of the HCP surface oxide generated through anodisation). The new method correctly determined the value for Euler 1 (ϕ_1) and Euler 2 (Φ) and the colour system employed plotted green & red colours in close correlation to corresponding EBSD orientation maps. The crystal symmetry of cubic structures helped to optimize the CPLM post processing procedure making this new simplified method more suited for potential

quality assurance applications.

- There was some discrepancy in the colour schemes between the two methods which highlights the fundamental limitation of symmetry representation in EBSD Euler maps. However, these differences were not found to translate to differences in the underlying orientation data and can therefore be considered as an advantage of the CPLM technique.
- This new method was successfully tested on anodised aluminium, which historically provides challenges for good EBSD orientation data. It was found that the re-anodising of aluminium had little effect on the subsequent crystal orientation provided the anodising parameters remained consistent.
- The oxide-substrate orientation relationship on which the current study builds was previously determined for a limited number of orientation combinations due to the complexity of extracting orientation data from surface layers of nanoscale thickness by HRTEM. The current study replicated the prior finding with a comparatively trivial technique, indicating its significant potential to study other such interfaces in the future.

The consistency of the data observed from the CPLM technique is the most notable advantage compared to the PLM approach. Also, having the sample in a stationary position significantly helped remove the mechanical errors initiated by rotating the sample. It was controlling the light instead of rotating the sample, which highly automated the CPLM approach and reduced the operation time and post-processing time. It also provides the opportunity to apply the technique in other applications, which is one of the crucial points for this research to make the technique more applicable to other materials with isotropic and anisotropic crystal systems (146).

Publication on this chapter: “*Using circular polarised light microscopy to investigate the crystal orientation of Aluminium*”; Journal of the Material Characterization 2022 - <https://doi.org/10.1016/j.matchar.2022.111749>

Future work

This research used a reflective polarised light microscope to introduce a cheaper, faster and more straightforward approach to extract the quantitative information about the anisotropic crystals like HCP (Ti) (80,114). The success becomes more evident since we have invented a novel polarised light microscopy technique to investigate the crystal orientation of isotropic crystals such as FCC crystal system, like aluminium. The new design used monochromatic light to create a highly accurate circular polarised light, plotting the crystal orientation map of anisotropic and isotropic crystals (Hamed Safaie 2022) (This success was a fundamental reason to invest this research on new samples like calcite, which is the most common form of natural calcium carbonate (CaCO_3), a widely distributed mineral. Also, Dolomite $\text{CaMg}(\text{CO}_3)_2$, is a double carbonate of calcium and magnesium and is the principal component of the sedimentary rock(134). The crystallographic orientation of crystallites is an essential piece of information for structural geologists studying the formation of rocks and their subsequent evolution (135–140). Many attempts have tried to introduce a simple approach to investigate the crystal orientation of CaCO_3 by using Computer Integrated Polarisation (CIP) since 1924 by Berek and later in 1994 by Panozzo-Heilbronner and Pauli and the recent effort in 2018 by Jellison, G. E. However, this method is only applicable to fragile samples, and the accuracy is not comparable to the EBSD method. The CPLM technique has the capability to provide highly accurate data and can also be applied to thick samples as it used the light reflected from the sample to plot the crystal orientation map (146).

- Zinc is used to galvanise other metals, such as iron, to prevent rusting. Galvanised steel is used for car bodies, street lamp posts, safety barriers, and suspension bridges. Large quantities of Zinc are used to produce die-castings, which are crucial in the automobile, electrical and hardware industries. Zinc is also used in alloys such as brass, nickel silver and aluminium solder. Zn-Al-based alloy is an excellent

example to develop the CPLM method on alloy-based material. Where we have witnessed the capability of the technique to provide COM of FCC crystal system (Al) and HCP crystal system (Ti) individually (141), this would be a novel analysis as there has not been any attempt of using a polarised light microscope to plot the COM of alloys. Also, there have been no attempts to extract quantitative information from Zinc based alloys using an optical microscope (11,142). The importance of having access into COM of Zn and its alloys is well stated in many different researchers by (112,143).

- Magnesium improves the mechanical, fabrication and welding characteristics of aluminium when used as an alloying agent. These alloys are useful in aircraft and car construction. Magnesium is optically anisotropic, and this would provide the capability to develop the CPLM method to solve the crystal orientation map of magnesium and its alloys like tungsten (12,144,145).

Appendix

MATLAB code for crystal orientation map

```
clear all;
```

```

clc;

close all;

%%%%%%%%%%%%%%%%%%%%%%%%%%%%%%%%%%%%%%%%%%%%%%%%%%%%%%%%%%%%%%%%%%%%%%%%%%%%%%
%%%%%%%%%

num_image = 230;

black_boundary = 1;

filter3 = 85;

%%%%%%%%%%%%%%%%%%%%%%%%%%%%%%%%%%%%%%%%%%%%%%%%%%%%%%%%%%%%%%%%%%%%%%%%%%%%%%
%%%%%%%%%

k1 = 1;

for ii = 0:5:num_image

    %p1= sprintf('(Hamed safaie)_10_M13_20x_001_%.d.jpg',ii);

    p1= [num2str(ii),'.jpg'];

    vid=[];

    vid = imread(p1);

    %      p1

    %vid_gray = [];

    vid_gray(:, :, k1) = rgb2gray(vid);

    k1 = k1+1;

```

```

        if ii ==0

            vid_gray2=rgb2gray(vid);

        end

    end

    si1 = size(vid)

    % si1(2)=1000;

    si1(1)=1040;

    % imtool(vid);

    % ss=si1(1);

    % si1(1) = si1(2)

    % si1(2) = ss

    for hh1 = 1:si1(2)

        for vv1 = 1:si1(1)

            if vid_gray2(vv1,hh1)<=filter3

                vid_gray(vv1,hh1,:) = 0;

            end

        end

    end

    end

    for hh1 = 1:si1(2)

        for vv1 = 1:si1(1)

```

```

k1 = 1;

for ii = 0:5:num_image

    intensity1(k1) = vid_gray(vv1,hh1,k1);

%       xval(k1)=ii;

    k1 = k1+1;

end

[M1,I1]=max(intensity1);

[M2,I2]=min(intensity1);

angle_max = (I1-1)*5;

if angle_max > 90 && angle_max <= 180

    angle_max = 180 - angle_max;

elseif angle_max > 180

    angle_max = angle_max - 180;

end

color_image(vv1,hh1,1) = floor(angle_max*256/90);

color_image(vv1,hh1,2) = floor(M1-M2);

color_image(vv1,hh1,3) = 0;

end

end

% M3 = max(color_image(:,2))

```

```

% size(M3)

M3 = 0;

for hh1 = 1:si1(2)

    for vv1 = 1:si1(1)

        if color_image(vv1,hh1,2) > M3

            M3 = color_image(vv1,hh1,2);

        end

    end

end

for hh1 = 1:si1(2)

    for vv1 = 1:si1(1)

        color_image(vv1,hh1,2) = floor(color_image(vv1,hh1,2).*256./M3);

    end

end

imwrite(color_image./256,'test11.png')

% %p1=sprintf('Hamed safaie_B4_f92163_10x_001_%.jpg',1)

%

imtool(color_image./256);

% vid_gray= rgb2gray(vid);

% %imtool(vid_gray);

```

```
% % (640,534)
```

```
% % (675,587)
```

```
% eval(sprintf('ind=Hamed safaie_B4_f92163_10x_001_%.jpg',ii+2));
```

```
% eval(sprintf('ind_main=ind%.d;',ii+2));
```

```
% eval(sprintf('ind_main=ind%.d;',ii+2));
```


References

1. Clegg W, Blake AJ, Cole JM, Evans JSO, Main P, Parsons S, et al. Crystal Structure Analysis: Principles and Practice. Crystal Structure Analysis: Principles and Practice. 2009;9780199219:1–408.
2. Rose JH, Smith JR, Ferrante J. Universal features of bonding in metals. Physical Review B. 1983;28(4):1835–45.
3. Cruickshank DWJ, Juretschke HJ, Kato N, Snyder RL, Fiala J, Bunge HJ. The Basics of Crystallography and Diffraction: Fourth Edition. 2015;2:1–519.
4. Y K Li, Y W Chen XWC et al. Physics of Mott insulators. (x).
5. Thompson B. Engineering Materials 1: An introduction to their properties & applications Michael F. Ashby & David R.H.Jones, Butterworth-Heinemann, 1996 (second edition), ISBN: 0-7506-30-81-7, 306 pp, 234 x 163 x 20 mm, £17.99 (softback). Materials & Design. 1996;17(5–6):303–4.
6. Hirasawa Y. Springer Japan KK. 2015. 2015.
7. Luneau D, Jeanneau E, Jal J-F, San Miguel A, Gueguen-Chaignon V, Haser R, et al. Auguste Bravais: a major human contribution. Acta Crystallographica Section A Foundations and Advances. 2014;70(a1):C1307–C1307.
8. Ladd MFC (Marcus FC, Palmer RA (Rex A. Structure determination by X-ray crystallography. 2003. 819.
9. Tables I. 5.2. Crystal-density measurements. 2006;117–23.
10. Nakashima PNH. The Crystallography of Aluminium and its Alloys. arXiv. 2020. 1–93.
11. Nafisi S, Roccisano A, Ghomashchi R, Voort G vander. A comparison between anodizing and EBSD techniques for primary particle size measurement. Metals. 2019 May 1;9(5).
12. Mironov S, Onuma T, Sato YS, Kokawa H. Microstructure evolution during friction-stir welding of AZ31 magnesium alloy. Acta Materialia [Internet]. 2015;100:301–12. Available from: <http://dx.doi.org/10.1016/j.actamat.2015.08.066>
13. Ashby J. The Aluminium Legacy : the History of the Metal and its Role in Architecture. The Construction History Society. 2014;15(1999):79–90.
14. Cobden R, Banbury A. Aluminium: Physical Properties, Characteristics and Alloys. Talat [Internet]. 1994;60. Available from: <http://www.alueurope.eu/talat/lectures/1501.pdf>

15. Masters BR. History of the Optical Microscope in Cell Biology and Medicine. Encyclopedia of Life Sciences. 2008;(September).
16. G.E. Thompson, R.C. Furneaux, G.C. Wood, J.A. Richardson, J.S. Goode, Nucleation and growth of porous anodic films on aluminium, *Nature* 272 (1978) 433–435.
17. Donatus U, Thompson GE, Elabar D, Hashimoto T, Morsch S. Features in aluminium alloy grains and their effects on anodizing and corrosion. *Surface and Coatings Technology*. 2015 Sep 15;277:91–8.
18. Reverdy M, Potocnik V. History of Inventions and Innovations for Aluminum Production. *Minerals, Metals and Materials Series*. 2020;(February):1895–910.
19. Kuroda M. Effects of Texture on Mechanical Properties of Aluminum Alloy Sheets and Texture Optimization Strategy. 2005.
20. Zhong C, Liu J, Zhao T, Schopphoven T, Fu J, Gasser A, et al. Laser metal deposition of Ti6Al4V-A brief review. *Applied Sciences (Switzerland)*. 2020;10(3):1–12.
21. Oosthuizen SJ. Titanium: the innovators' metal - Historical case studies tracing titanium process and product innovation. *Journal of the Southern African Institute of Mining and Metallurgy*. 2011;111(11):781–6.
22. Tarui N, Nagano Y, Sakane T, Matsumoto K, Kawada M, Uchikawa O, et al. Kinetic resolution of an indan derivative using *Bacillus* sp. SUI-12: Synthesis of a key intermediate of the melatonin receptor agonist TAK-375. *Journal of Bioscience and Bioengineering*. 2002;93(1):44–7.
23. W. Nicholson J. Titanium Alloys for Dental Implants: A Review. *Prosthesis*. 2020;2(2):100–16.
24. Warlimont H. Titanium and titanium alloys. *Springer Handbooks*. 2018. 195–206.
25. Ma B, Rao QH, He YH. Effect of crystal orientation on tensile mechanical properties of single-crystal tungsten nanowire. *Transactions of Nonferrous Metals Society of China (English Edition)*. 2014 Sep 1;24(9):2904–10.
26. Newton CJ, Vacher HC. Correlation of Polarized Light Phenomena With the Orientation of Some Metal Crystals. Vol. 53, *Journal of Research of the National Bureau of Standards*. 1954.
27. Curtis RK, Tyson DONR. Birefringence : Polarization Microscopy as a Quantitative Technique of Human Hair Analysis. *Journal of the Society of Cosmetic Chemists*. 1976;27(9):411–31.

28. Huang LF, Grabowski B, Mceniry E, Trinkle DR, Neugebauer J. Importance of coordination number and bond length in titanium revealed by electronic structure investigations. *Physica Status Solidi (B) Basic Research*. 2015;252(9):1907–24.
29. Placidi L, Hutter K. An anisotropic flow law for incompressible polycrystalline materials. *Zeitschrift fur Angewandte Mathematik und Physik*. 2005;57(1):160–81.
30. Extensive THE. The crystallography and deformation modes of hexagonal close-packed metals. :169–94.
31. Ambroziak A, Solarczyk MT. Application and mechanical properties of aluminium alloys. *Shell Structures: Theory and Applications Volume 4 - Proceedings of the 11th International Conference on Shell Structures: Theory and Applications, SSTA 2017*. 2018;(May 2020):525–8.
32. Obasi GC. Variant Selection and its Effect on Texture in Ti-6Al-4V. 2011;1–301.
33. S.H.Whang. (2011). *Nanostructured Metals and Alloys*. New York University, USA: Woodhead Publishing Series in Metals and Surface Engineering.
34. Paul Worsfold, Alan Townshend, Colin Poole. (2005). *Encyclopedia of Analytical Science*. 2nd ed. UK: Elsevier.
35. Atul Chauhan, Amba D.BhattProf. (2022). Effect of unit cell features on mechanical properties of lattice structures at constant porosity levels: A general mixtu. *Materialstudy proceedings*. 56(1), pp.1-8. [Online]. Available at: <https://doi.org/10.1016/j.matpr.2021.11.323> [Accessed 3 July 2022].
36. Ma B, Rao QH, He YH. Effect of crystal orientation on tensile mechanical properties of single-crystal tungsten nanowire. *Transactions of Nonferrous Metals Society of China (English Edition)*. 2014;24(9):2904–10.
37. T.Kogure. (2013). *Developments in Clay Science*. Department of Earth and Planetary Science, Graduate School of Science, The Unive: Elsevier. pp.275-317.
38. Jian Zhaoab, Xia Liua. (2022). Electron microscopic methods (TEM, SEM and energy dispersal spectroscopy) Author links open overlay panel. *Reference Module in Earth Systems and Environmental Sciences*. 1(1). [Online]. Available at: <https://doi.org/10.1016/B978-0-12-822974-3.00013-6> [Accessed 15 July 2022].
39. Birch JM, Wilshire B. The effect of crystal orientation on the creep behaviour of magnesium oxide. *Philosophical Magazine*. 1975;31(6):1421–4.

40. Albrecht R, Rak J, Bogdanowicz W, Gancarczyk K, Sieniawski J, Kubiak K, et al. Effect of creep on crystallographic orientation in single crystal superalloy. *Acta Physica Polonica A*. 2016;130(4):1094–6.
41. Martin Hÿtch, Peter W. Hawkes. (2021). *Advances in Imaging and Electron Physics*. UK: Academic Press.
42. Robert A. Meyers. (2001). *Encyclopedia of Physical Science and Technology*. 3rd ed. USA: Academic Press.
43. ChaoyiZhu, MarcDe Graef. (2020). EBSD pattern simulations for an interaction volume containing lattice defects. *Ultramicroscopy*. 218(1), pp.1-12. [Online]. Available at: <https://doi.org/10.1016/j.ultramic.2020.113088> [Accessed 7 August 2022].
44. Ro YJ, Agnew SR, Gangloff RP. Crystallography of fatigue crack propagation in precipitation-hardened Al-Cu-Mg/Li. In: *Metallurgical and Materials Transactions A: Physical Metallurgy and Materials Science*. 2007. p. 3042–62.
45. Dahmen U. Orientation relationships in precipitation systems. *Acta Metallurgica*. 1982;30(1):63–73.
46. Tromans D. Elastic Anisotropy of HCP Metal Crystals and Polycrystals. *Ijrras*. 2011;6(March):462–83.
47. Somekawa H, Schuh CA. Effect of Crystal Orientation on Nanoindentation Behavior in Magnesium. *Metallurgical and Materials Transactions A: Physical Metallurgy and Materials Science*. 2016;47(6):3227–34.
48. Britton TB, Liang H, Dunne FPE, Wilkinson AJ. The effect of crystal orientation on the indentation response of commercially pure titanium: Experiments and simulations. *Proceedings of the Royal Society A: Mathematical, Physical and Engineering Sciences*. 2010;466(2115):695–719.
49. Bache MR, Evans WJ. Impact of texture on mechanical properties in an advanced titanium alloy. 2001;321:409–14.
50. Bridier F, Villechaise P, Mendez J. Analysis of the different slip systems activated by tension in a / b titanium alloy in relation with local crystallographic orientation. 2005;53:555–67.
51. Whittaker M, Jones P, Pleydell-pearce C, Rugg D, Williams S. The effect of prestrain on low and high temperature creep in Ti834. *Materials Science & Engineering A [Internet]*. 2010;527(24–25):6683–9. Available from: <http://dx.doi.org/10.1016/j.msea.2010.07.008>

52. Germain L, Gey N, Humbert M, Hazotte A, Bocher P, Jahazi M. An automated method to analyze separately the microtextures of primary α grains and the secondary α s inherited colonies in bimodal titanium alloys. 2005;54:216–22.
53. Rugg D, Dixon M, Dunne FPE, Plc R. Effective structural unit size in titanium alloys. 2007;42:269–79.
54. Paul Verkade, Thomas Muller-Reichert. (2012). Correlative light and electron microscopy fundamentals. UK: Elsevier Science.
55. Spence H. Handbook Microscopy. Springer. 2019. 1–1561.
56. Lawlor D. Introduction to Light Microscopy. Introduction to Light Microscopy. 2019.
57. Goldstein JI, Newbury DE, Michael JR, Ritchie NWM, Scott JHJ, Joy DC. Microscopy and X-Ray Microanalysis. 2018. 554.
58. Danz R, Gretscher P. C-DIC: A new microscopy method for rational study of phase structures in incident light arrangement. Thin Solid Films. 2004;462–463(SPEC. ISS.):257–62.
59. Suoninen EJ. Optical microscopy. Surface Characterization: A User's Sourcebook. 2007;(April):54–6.
60. Kuo TC, Ding TJ, Lin JH, Ma SH. Optical design of an LED lighting source for fluorescence microscopes. Applied Sciences (Switzerland). 2019;9(21):1–14.
61. Abramowitz M. Microscopy: Basics and Beyond. Molecular Expressions Microscopy Primer. 2003;1:1–50.
62. Wallace H. A Different Kind of Chemistry: A History of Tungsten Halogen Lamps. IEEE Industry Applications Magazine. 2001;7(6):10–7.
63. Cho J, Park JH, Kim JK, Schubert EF. White light-emitting diodes: History, progress, and future. Laser and Photonics Reviews. 2017;11(2).
64. Karman SB, Diah SZM, Gebeshuber IC. Bio-inspired polarized skylight-based navigation sensors: A review. Sensors (Switzerland). 2012;12(11):14232–61.
65. Kumar P, Foundation T, Academy P. Chapter · January 2018. 2018;(January).
66. Weiss AD. Scanning Electron Microscopes. Semiconductor International. 1983;6(10):90–4.
67. Han W, Jiao H, Fox D. Scanning electron microscopy. Vol. 272, Springer Tracts in Modern Physics. Elsevier Inc.; 2018. 35–68.

68. Scheu C, Kaplan WD. Introduction to Scanning Electron Microscopy. In-Situ Electron Microscopy: Applications in Physics, Chemistry and Materials Science. 2012;1–37.
69. Alink R, Gerteisen D. Scanning electron microscopy. PEM Fuel Cell Diagnostic Tools. 2011;315–32.
70. Britton TB, Jiang J, Guo Y, Vilalta-Clemente A, Wallis D, Hansen LN, et al. Tutorial: Crystal orientations and EBSD - Or which way is up? Materials Characterization [Internet]. 2016;117(April):113–26. Available from: <http://dx.doi.org/10.1016/j.matchar.2016.04.008>
71. By Seishi KIKUCHI. Institute of Physical and Chemical Research, Tokyo. (Rec. June 9, 1928. Comm. by T. TERADA, M. I .A., June 12, 1928.). 1928;117(6).
72. Schwarzer RA. Backscatter and transmission Kikuchi diffraction for materials science. Available from: <http://www.ebsd.info/pdf/overview.pdf>
73. Maitland T, Sitzman S. (EBSD) Technique and Materials Characterization Examples. :41–76.
74. Chen Z, Yang Y, Jiao H. Some Applications of Electron Back Scattering Diffraction (EBSD) in Materials Research. Scanning Electron Microscopy. 2012;
75. Mariani E. Electron backscatter diffraction (EBSD) in the SEM: applications to microstructures in minerals and rocks and recent technological advancements. Instrumental Techniques Applied to Mineralogy and Geochemistry, Zaragoza. 2008;120(3):7–20.
76. Sémoroz A, Strezov L, Rappaz M. Orientation domains and texture in hot-dipped galvanized coatings. Metallurgical and Materials Transactions A: Physical Metallurgy and Materials Science. 2002;33(8):2695–701.
77. Elvins J, Spittle JA, Worsley DA. Relationship between microstructure and corrosion resistance in Zn-Al alloy coated galvanised steels. Corrosion Engineering Science and Technology. 2003;38(3):197–204.
78. Zhang L, Wang Y, Yang X, Li K, Ni S, Du Y, et al. Texture, microstructure and mechanical properties of 6111 aluminum alloy subject to rolling deformation. Materials Research. 2017 Oct 1;20(5):1360–8.
79. Abdolvand H, Wright J, Wilkinson AJ. Strong grain neighbour effects in polycrystals. Nature Communications. 2018;9(1):1–11.

80. Safaie H, Mitchell RL, Johnston R, Russell J, Pleydell-Pearce C. An Assessment of Polarized Light Microscopy for the Quantification of Grain Size and Orientation in Titanium Alloys via Microanalytical Correlative Light to Electron Microscopy (CLEM). *Microscopy and Microanalysis*. 2018;24(S1):400–1.
81. Gou J, Shen TH, Bao P, Ramos Angulo JL, Evans SD. A stokes polarimetric light microscopy view of liquid crystal droplets. *Sci Rep*. 2021 Aug 11;11(1):16329. doi: 10.1038/s41598-021-95674-4. PMID: 34381082; PMCID: PMC8358033.
82. Agarwal N. Basics of Polarization. 2013;1–28.
83. Collett E. Field Guide to Polarization. Field Guide to Polarization. 2009.
84. David Kliger, James Lewis. (1990). Polarized Light in Optics and Spectroscopy. USA: University of California, Santa Cruz.
85. Schaefer B, Collett E, Smyth R, Barrett D, Fraher B. Measuring the Stokes polarization parameters. *American Journal of Physics*. 2007 Feb;75(2):163–8.
86. Cardano F, Karimi E, Slussarenko S, Marrucci L, Lisio C De, Santamato E. Polarization pattern of vector vortex beams generated by q-plates with different topological charges. *Applied Optics*. 2012;51(10):1–6.
87. Magnusson R. Mueller matrix ellipsometry studies of nanostructured materials. 57.
88. Jellison GE. Data Analysis for Spectroscopic Ellipsometry. *Handbook of Ellipsometry*. William Andrew, Inc.; 2005. 237–296.
89. Spandana KU, Mahato KK, Mazumder N. Polarization-resolved Stokes-Mueller imaging: a review of technology and applications. *Lasers in Medical Science*. 2019;34(7):1283–93.
90. Krijger JM, Snel R, Van Harten G, Rietjens JHH, Aben I. Mirror contamination in space I: Mirror modelling. *Atmospheric Measurement Techniques*. 2014;7(10):3387–98.
91. Cox AJ. Quantitative analysis of elliptically polarized light. *American Journal of Physics*. 1978;46(3):302–3.
92. Hu Y, Yi Z, Yang H, Xiao J. A simple method to measure the thickness and order number of a wave plate. *European Journal of Physics*. 2013 Sep;34(5):1167–73.
93. Modern Optics Simplified - Robert D. Guenther - Google Books.
94. Banerjee D, Williams JC. Microstructure and Slip Character in Titanium Alloys. *Defence Science Journal*. 1986;36(2):191–206.

95. Le Biavant K, Pommier S, Prioul C. Local texture and fatigue crack initiation in a Ti-6Al-4V titanium alloy. *Fatigue and Fracture of Engineering Materials and Structures*. 2002;25(6):527–45.
96. Bache MR. A review of dwell sensitive fatigue in titanium alloys : the role of microstructure , texture and operating conditions. 2003;25:1079–87.
97. Astrophysical A. Revision of a Pair of Classics : Born and Wolf ' s , and Allen ' s Principles of Optics : 2000;
99. Ross S, Newton R, Zhou YM, Haffeggee J, Ho MW, Bolton JP, et al. Quantitative image analysis of birefringent biological material. *Journal of Microscopy*. 1997;187(1):62–7.
100. Shribak M, Oldenbourg R. Techniques for fast and sensitive measurements of two-dimensional birefringence distributions. *Applied Optics*. 2003;42(16):3009.
101. Whittaker P, Przyklenk K. Fibrin architecture in clots: A quantitative polarized light microscopy analysis. *Blood Cells, Molecules, and Diseases*. 2009;42(1):51–6.
102. Science E, Road P, Ox O. Quantitative polarized light microscopy. 2003;209(October 2002):13–22.
103. Mikheenko P, Mart E, Bevan A, Abell JS. Grain boundaries and pinning in bulk MgB₂ J L MacManus-Driscoll. 264.
104. Tompkins HG, Irene EA, Hill C, Carolina N. Handbook of Ellipsometry. *Handbook of Ellipsometry*. 2006.
105. EDWIN HERBERT LAND. (1994). EDWIN HERBERT LAND. UK: The Royal Society and the author. pp.197-219.
106. Shapira Y. The Linear Elasticity Equations. Solving PDEs in C++. 2011;403–12.
107. Wu S, Naghavi SS, Fecher GH, Felser C. A Critical Study of the Elastic Properties and Stability of Heusler Compounds: Phase Change and Tetragonal; X₂YZ Compounds. *Journal of Modern Physics*. 2018;09(04):775–805.
108. Randle V. Application of EBSD to the analysis of interface planes: Evolution over the last two decades. *Journal of Microscopy*. 2008;230(3):406–13.
109. Mingard KP, Roebuck B, Bennett EG, Thomas M, Wynne BP, Palmiere EJ. Grain size measurement by EBSD in complex hot deformed metal alloy microstructures. *Journal of Microscopy*. 2007;227(3):298–308.

110. Nolze G. Image distortions in SEM and their influences on EBSD measurements. *Ultramicroscopy*. 2007;107(2–3):172–83.
111. Nolze G. Euler angles and crystal symmetry. *Crystal Research and Technology*. 2015 Feb 1;50(2):188–201.
112. Boehm-Courjault E, Gonzales F, Jacot A, Kohler F, Mariaux A, Niederberger C, et al. EBSD: A powerful microstructure analysis technique in the field of solidification. *Journal of Microscopy*. 2009;233(1):160–9.
113. Callahan PG, Echlin M, Pollock TM, Singh S, De Graef M. Three-dimensional texture visualization approaches: Theoretical analysis and examples. *Journal of Applied Crystallography*. 2017;50:430–40.
114. Böhme L, Morales-Rivas L, Diederichs S, Kerscher E. Crystal c-axis mapping of hcp metals by conventional reflected polarized light microscopy: Application to untextured and textured cp-Titanium. *Materials Characterization* [Internet]. 2018;145(July):573–81. Available from: <https://doi.org/10.1016/j.matchar.2018.09.024>
115. Nafisi S, Roccisano A, Ghomashchi R, Voort G Vander. A comparison between anodizing and EBSD techniques for primary particle size measurement. *Metals*. 2019 May 1;9(5).
116. Seshagiri PC, Nair BS, Reddy GM, Rao KS, Bhattacharya SS, Rao KP. Improvement of mechanical properties of aluminium-copper alloy (AA2219) GTA welds by Sc addition. *Science and Technology of Welding and Joining*. 2008 Mar;13(2):146–58.
117. Koll L, Tsipouridis P, Werner EA. Preparation of metallic samples for electron backscatter diffraction and its influence on measured misorientation. *Journal of Microscopy*. 2011;243(2):206–19.
118. Wielage B, Alisch G, Lampke T, Nickel D. Anodizing - A key for surface treatment of aluminium. *Key Engineering Materials*. 2008;384:263–81.
119. X. Zhou, E. Thompson, Skeldon AGC, P. Wood, K. Shimizu, H. Habazaki, Anodic Oxidation of an Al₉₀Cu₁₀ Alloy Effect of Grain Orientation, 2021.
120. Higgins MD. Imaging birefringent minerals without extinction using circularly polarized light. *Canadian Mineralogist*. 2010;48(1):231–5.
121. Theofanous NG. Error analysis of circular polariser–analyzer systems for phase retardation measurements. *Journal of the Optical Society of America A*. 2008;4(12):2191.
122. Chen W, Li H, Zhang S, Long X. Measurement of phase retardation of waveplate online based on laser feedback. *Review of Scientific Instruments*. 2012;83(1):2012–5.

123. Richartz M, Hsü H-Y. Analysis of Elliptical Polarization. *Journal of the Optical Society of America*. 1949;39(2):136.
124. Sacco L, Florea I, Châtelet M, Cojocaru CS. Investigation of porous anodic alumina templates formed by anodisation of single-crystal aluminum substrates. *Thin Solid Films*. 2018 Aug 30;660:213–20.
125. Li F, Zhang L, Metzger RM. On the Growth of Highly Ordered Pores in Anodized Aluminum Oxide. 1998.
126. Jensen F, Gudla VC, Kongstad I, Ambat R. High frequency pulse anodising of aluminium: Anodising kinetics and optical appearance. *Surface and Coatings Technology*. 2019;360:222–31.
127. Scott S, Ko J. Polarization Changes by flat, ideal mirrors. 2008;1–27.
128. Ferro-Famil L, Pottier E. SAR Imaging using Coherent Modes of Diversity: SAR Polarimetry, Interferometry and Tomography. *Microwave Remote Sensing of Land Surfaces: Techniques and Methods*. 2016;67–147.
129. Li P, Lv D, He H, Ma H. Separating azimuthal orientation dependence in polarization measurements of anisotropic media. *Optics Express*. 2018 Feb 19;26(4):3791.
130. Milione G, D’Addario AJ, Jones JA, Galvez EJ, Rojec BL. The Poincaré-sphere approach to polarization: Formalism and new labs with Poincaré beams. *American Journal of Physics*. 2016;84(11):822–35.
131. Pizurica A. Pattern Encoding on the Poincare Sphere. 2014;1–26.
132. Suzuki M, Yamane K, Oka K, Toda Y, Morita R. Full Quantitative Analysis of Arbitrary Cylindrically Polarized Pulses by Using Extended Stokes Parameters. *Scientific Reports*. 2015;5(September):1–9.
133. Nolze G. Euler angles and crystal symmetry. *Crystal Research and Technology*. 2015;50(2):188–201.
134. Al- Awadi M, Clark WJ, Herron M, Hurley N, Kho D, Montaron B, et al. Dolomite : Perspectives on a Dolomite is a metastable carbonate . It forms in a variety of distinctly different settings. *oilfield Review*. 2009;3(September):32–45.
135. Kamb WB. Theory of Preferred Crystal Orientation. Kamb, W. B. (1958). Theory of Preferred Crystal Orientation Developed. *Journal of Geology*, 67(2), 153–170. on Developed. *Journal of Geology*. 1958;67(2):153–70.

136. Rutter EH, Casey M, Burlini L. Preferred crystallographic orientation development during the plastic and superplastic flow of calcite rocks. *Journal of Structural Geology*. 1994;16(10):1431–46.
137. Pennacchioni G, Menegon L, Leiss B, Nestola F, Bromiley G. Development of crystallographic preferred orientation and microstructure during plastic deformation of natural coarse-grained quartz veins. *Journal of Geophysical Research: Solid Earth*. 2010;115(12).
138. Gilbert PUPA, Young A, Coppersmith SN. Measurement of c-axis angular orientation in calcite (CaCO₃) nanocrystals using X-ray absorption spectroscopy. *Proceedings of the National Academy of Sciences of the United States of America*. 2011;108(28):11350–5.
139. Michels ZD, Tikoff B, Kruckenberg SC, Davis JR. Determining vorticity axes from grain-scale dispersion of crystallographic orientations. *Geology*. 2015;43(9):803–6.
140. Gregg JM, Bish DL, Kaczmarek SE, Machel HG. Mineralogy, nucleation and growth of dolomite in the laboratory and sedimentary environment: A review. *Sedimentology*. 2015;62(6):1749–69.
141. Zhu YH, Lee WB, Yeung CF, Yue TM. EBSD of Zn-rich phases in Zn-Al-based alloys. *Materials Characterization*. 2001;46(1):19–23.
142. Garcia CB, Ariza E, Tavares CJ, Villechaise P. Electron backscatter diffraction analysis of ZnO:Al thin films. *Applied Surface Science* [Internet]. 2012;259:590–5. Available from: <http://dx.doi.org/10.1016/j.apsusc.2012.07.081>
143. Etienne A, Cadel E, Lina A, Cretinon L, Pareige P. Crystallographic characterization of an electroplated zinc coating prone to whiskers. *IEEE Transactions on Components, Packaging and Manufacturing Technology*. 2012;2(11):1928–32.
144. Tripathi A, Zaefferer S. On the spatial resolution of EBSD in magnesium. *arXiv*. 2019;
145. Jiang S, Jia Y, Wang X, Jiang J. Precise measurement of strain accommodation in a Mg-Gd-Y-Zn alloy using cross-correlation-based high resolution EBSD. *Materials Characterization* [Internet]. 2020;165(May):110384. Available from: <https://doi.org/10.1016/j.matchar.2020.110384>
146. Safaie, H., Coleman, M., Johnston, R., Das, A., Russell, J., & Pleydell-Pearce, C. (2022). Circular polarized light microscopy to investigate the crystal orientation of aluminium. *Materials Characterization*, 185, p. 111749. doi:10.1016/j.matchar.2022.111749

